On the Storm-Time Character of Earth's Mid-Latitude Ionospheric Irregularities

by

Thomas Ronald Parsons Heine

A dissertation submitted in partial fulfillment
of the requirements for the degree of
Doctor of Philosophy
(Atmospheric, Oceanic, and Space Sciences)
in The University of Michigan
2016

Doctoral Committee:

Professor Mark B. Moldwin, Co-Chair
Associate Professor Shasha Zou, Co-Chair
Assistant Professor Branko Kerkez
Professor Aaron Ridley

The Lord said to Gideon, "You have too many men. I cannot deliver Midian into their hands, or Israel would boast against me, 'My own strength has saved me.'..."(Judges 7:2, New International Version)

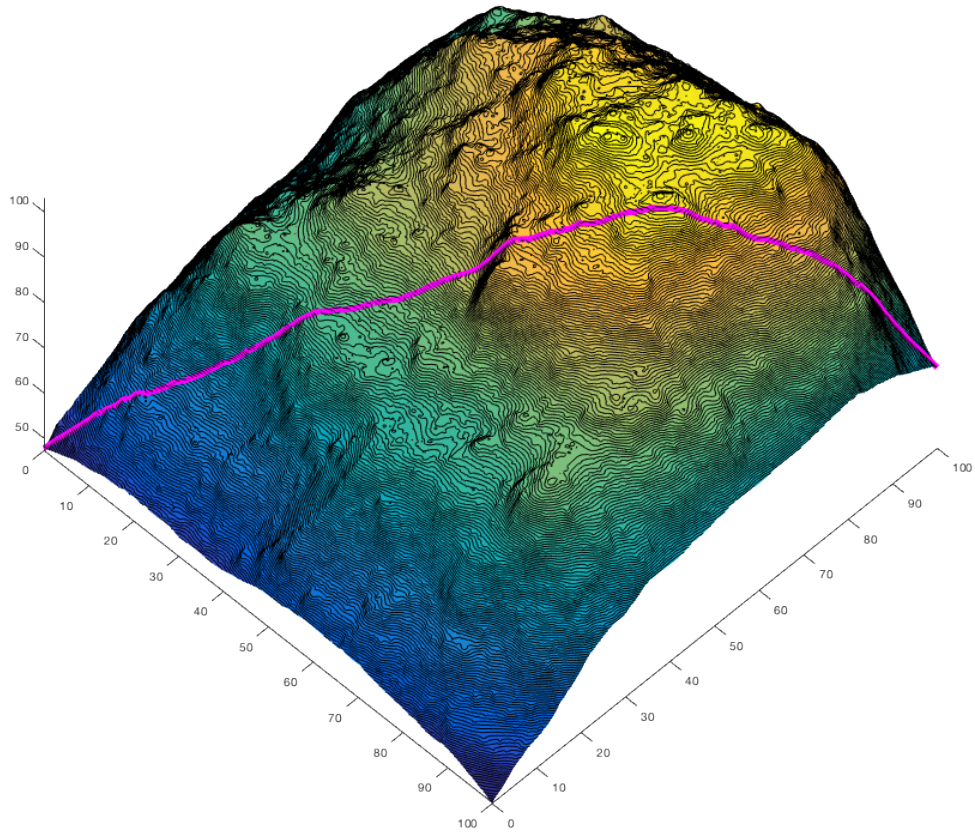

GPS Ionospheric Pierce Point track through synthetic multi-scale TEC structure.

For my wife, Molliebeth, for whom I love and am forever grateful.

For my parents, Ronald and Norma, who chose me and whose support has been a constant in my life.

ACKNOWLEDGEMENTS

Thank you Professor Mark Moldwin for an uncountable collection of generosities, beginning with your interest and investment in me as an MEng student, your encouragement and opportunity to become your PhD student, and many opportunities along the way, including the chance to attend a conference in Ethiopia and to participate in an interplanetary CubeSat proposal to Mars. Above all, thank you Mark for your constant mentorship and friendship in matters big and small.

Thank you Professor Shasha Zou for your insight, direction, and guidance in research and welcoming me into the founding membership of your research group. Your arrival as my co-advisor and dissertation co-chair could not have been a better addition to my research and development as a PhD Candidate.

Thank you Professor Aaron Ridley for introducing me to real flight systems hardware, first in AOSS 584, the design-build-fly high altitude balloon class, and my very first class at the University of Michigan. Thank you for the opportunity to work on CADRE for two summers and the academic years around them. Thank you also for frequent and sage words of wisdom and strong doses of reality amidst some truly brilliant wise cracks.

Thank you Professor Branko Kerkez for serving as the cognate member to my dissertation committee and for teaching my last class at the University of Michigan. The broad material you somehow covered that term will carry with me through the rest of my career I am sure. Thank you also for numerous office visits helping me to

better understand and improve the methods of my dissertation research.

My deep appreciation to Professor James (Jamie) Cutler for introducing me to the world of CubeSats and taking a chance on me and bringing me into your spacecraft laboratory for two summers.

Thank you to Dr. Jeremy Bassis for your patient and excellent instruction in the impromptu Mathematical Methods for Geoscience course that got me up and running on graduate mathematics.

Thank you, Theresa Caranza-Fulmer for being a wonderful colleague, classmate, officemate, project partner, and friend.

Thank you Xianyung Zhang for being a wonderful research group "sibling" and extraordinarily supportive friend in the run up to qualifying exams.

Thank you Doga Ozturk for your leadership, contagious enthusiasm in group meetings, and your overall kindness. You have one of the most extraordinary attitudes and outlooks of anyone I've ever met! Thank you also for pulling together last minute velocity data and wrestling with DaViTPy for me as I worked on the last stages of my dissertation.

Thank you Nick Perlongo for being my friend despite my persistent inability to commit to hanging out outside of school. Your renowned humor and sharp style are overshadowed by your genuineness and willingness to be a great friend. I am certain that, had I had your advice the first time around, the outcome of my first oral qualifying exam could have been much different. Thank you most recently for all of your help and advice prepping my dissertation defense.

Thank you Charles Bussy-Virat, first of course, for all of the work you did on SCION — starting with the 583 project, and much later the SmallSat talk. Thank

your for weathering my dissertation defense practice and the amazing advice and support from you and Nick. I'm glad that we got to know each other and I only regret we didn't start sooner.

Thank you Stacey Kawecki for "weathering" Fluid Dynamics, all-night Radiative Transfer homework sessions, and being an awesome sounding board for the past four years. You are my O.G. PhD friend and you have proven once again that the best people come from Hillsborough, NJ.

Thank you Harvey Elliot for being a great friend, a great engineer turned PhD space scientist, and trailblazer of Airbnb lodging at AGU. I'm glad we got to know each other and I'm sure we will have many more opportunities to continue.

Thank your Lois Sarno-Smith for your irrepressible spirit, great perspectives, and superb blogs. I was glad to have you in journal club and to talk with you during our mutual final weeks of PhD candidacy.

Thank you Faye Ogasawara, Darren Britten-Bozzone, Brian White, Melissa Terwilliger, and Kevin McLaughlin for keeping the wheels on and engines running at countless turns during my time in AOSS/CLaSP. Thank you for putting up with an embarrassment of support tickets and my weird Matlab dilemmas. Your collective quality and professionalism is beyond compare.

I am indebted for the substantial efforts of Ms. Edilia Thomas, Ms. Marie McKnight, and Ms. Laura Hopkins for their support and mountains of effort put into students and faculty to make possible the resources, purchase requests, computers, and travel reports that keep a student's life moving. Additionally, I am forever delighted to have found a fellow Whovian in Ms. Thomas and will be sure to keep up with her Dr. Who inspired knit creations on Facebook.

I cannot express my appreciation to Ms. Margaret Reid and Dr. Darren McKague for being my first contacts with the University of Michigan and opening the door into the Master of Engineering in Space Systems program. In addition to being an outstanding Masters advisor, Dr. McKague is an outstanding teacher and mentor whose perspective on the aerospace industry, systems engineering, and life in general uniquely shines through a lens of sincerity and humility.

Thank you Ms. Sandra Pytlinski for so many things ranging from making sure I remembered to close my door during fire drills to reminding me of the necessary hurdles in my progress toward graduation. Thank you for your time, considerable effort, open door, willingness to help, and endless patience.

My deepest thanks to the AOSS 583 teams that worked on developing the SCION engineering design, but especially my co-authors on the resulting Journal of Small Satellites paper: Jessica Arlas, Ambarish Desai, Brandon Heidt, Steve McCarthy, Adelina Nastasoiu, and Vritika Singh.

Thank you Ms. Marti Moon for showing me what "service where you are" actually looks like, putting every other person first, and perpetually reminding me where to look no matter whatever else might be going on. You are an example, mentor, servant, and light in this world.

Thank you Dr. Steve Bougher for numerous coffee, hallway, and office discussions full of life, faith, purpose, fellowship, and friendship.

Thank you Damen Provost for being simultaneously a mentor, colleague, fellow Airman, and friend.

Thank you Professor Harlan Spence of Boston University and later the University of New Hampshire. Thank you for your continued support through many letters of

recommendation at each step along the way of my MEng and PhD journey and occasional visits to my AGU posters.

Thank you Lt Col (Ret) Jon Schoenberg for exemplifying what it looks like to be a scientist, engineer, and Air Force Officer.

I could not complete this journey without the immeasurable, spiritual, emotional, and tangible support of Liz and Bob Soloman, Megan and Kevin Packard, James and Christina Heine, Joe Heine, and Chad Parsons.

Benjamin Parsons, I can't tell you how great it has been knowing you from your early teens to becoming a brother and friend. Thank you for many late night geek-out sessions and letting me wax on about space, science, politics and whatever other ramblings I am prone to. I am both thankful for your friendship and exceedingly proud of you.

Thank you my daughter, Florence (Flossie) Soleil Heine, for being joy and light in my life and in our family. You could not have come into our lives at a better time and if you read this some day, thank you for surprising us with an overabundance of love and joy in our lives during this period.

Lastly, yet with gratitude that cannot ever be adequately expressed, thank you my wife, Molliebeth Parsons Heine, for continued support, encouragement, exertion, patience, sacrifice, and understanding over these five years of our marriage during the entirety of which I also existed as a full time graduate student. Of everyone that has touched my life during these years, it is you that I will continue to walk with joyfully every day into a great and future adventure.

So many people positively influenced my time at the University of Michigan, and the rest of life during this time period. I am regrettably and certainly amiss having

not specifically included them all here. I hope that they will forgive my inadvertent omission and accept my deepest appreciation nonetheless.

TABLE OF CONTENTS

LIST OF FIGURES

Figure

LIST OF TABLES

Table

LIST OF ABBREVIATIONS

TEC Total Electron Content

VTEC Vertical Total Electron Content

STEC Slant Total Electron Content

SED Storm Enhanced Density

GPS Global Positioning System

GNSS Global Navigation Satellite Systems

EUVAC EUV model for Aeronomic Calculations

PRN Pseudorandom Number

EUV Extreme Ultraviolet

Dst Disturbance Storm Time

$\mathbf{K_p}$ Planetary K Index

SAPS Sub-auroral Polarization Stream

WAAS Wide-area Augmentation System

FAA Federal Aviation Administration

VNAV Vertical Navigation System

ROT Rate of TEC

ROTI Rate of TEC (ROT) Index

HF High Frequency

VHF Very High Frequency

UHF Ultra High Frequency

OTH Over the Horizon

IPP Ionospheric Pierce Point

NOAA National Oceanic and Atmospheric Administration

DMSP Defense Meteorological Satellite Program

FFT Fast Fourier Transform

TECU TEC Unit, TECU = 10^{16} [e^{-} m^{-2}]

FAC Field-Aligned-Current

ISR Incoherent Scatter Radar

RINEX Receiver Independent Exchange Format

IMF Interplanetary Magnetic Field

SSC Sudden Storm Commencement

SNR Signal-to-Noise Ratio

SCION SCintillation and Ionospheric Occultation NanoSat

NASA National Aeronautics and Space Administration

JPL Jet Propulsion Laboratory

UT Universal Time

LT Local Time

SPRL Space Physics Research Laboratory

SRB Space Research Building

ABSTRACT

On the Storm-Time Character of Earth's Mid-Latitude Ionospheric Irregularities

by

Thomas Ronald Parsons Heine

Co-Chairs Mark B. Moldwin and Shasha Zou

During strong geomagnetic storms, the usual, horizontally uniform mid-latitude ionosphere can undergo a dramatic reconfiguration and become highly structured with the formation of Storm Enhanced Density (SED) plumes that were first observed in the North American sector, but have since been observed in all sectors at magnetic mid-latitudes. Along the steep gradients of these high density plumes and the low density plasmapause boundary, or trough, plasma instabilities can produce small-scale density variations, or irregularities. These small-scale density irregularities have the potential to interfere with the transmission of the radio waves used in space-based communication and navigation systems in a phenomenon known as scintillation. The societal impact from degradation in Global Navigation Satellite Systems (GNSS) (e.g., the Global Positioning System (GPS)) alone extends beyond the usual navigation application and into the systems' use as a precise global time keeper — used to synchronize human activities ranging from high speed financial transactions, the power transmission grid, to the internet itself.

Using spatial, temporal, and frequency analyses of ground-based GPS Total Electron Content (TEC), in combination with radar ion velocity measurements, the

kilometer-scale irregularities responsible for High Frequency (HF) scintillation are detected and used to characterize the regions of the SED plume system in which they occur. The full scope of these observations, especially the determination of their vertical extent, will be greatly enhanced by the SCintillation and Ionospheric Occultation NanoSat (SCION) mission to perform space-based top-side, cross-track, and limb GPS radio occultations from two closely spaced (<5 km) spacecraft. Finally, a survey of twelve strong geomagnetic storms between 2012-2016 reveals correlations between the different regions of the SED plume system and the formation of small-scale irregularities at mid-latitudes.

This study demonstrates the utility of a combined coherent scatter radar and TEC Fast Fourier Transform (FFT) method for detecting, locating, and measuring the intensity and length scale of small-scale irregularities against background large-scale density structures such as SED plumes. This method is first applied to the great storm of March 17, 2015 (Dst = -223) and indicates 2-10 km irregularities on the poleward gradient of the SED plume, near gradients within the mid-latitude trough, and in the aurora — which were observed as low as 42° geodetic latitude — and is extended for application to broad comparisons between storms using three spectral parameters: Maximum Amplitude, Frequency of Maximum Amplitude, and Maximum Frequency of the TEC FFT spectra, and reveals a dependency of TEC variability on the storm phase during observation of the SED plume system. Lastly, this dissertation includes a detailed mission design and architecture of a two, 1U CubeSat formation mission to investigate small-scale irregularities during geomagnetic storms with broader coverage than ground measurements, and measurement geometries that are only possible from orbit and will be used to produce vertical density profiles, multipoint TEC observations of the top-side ionosphere, and constant-altitude cross-track multipoint observations of small-scale irregularities.

CHAPTER I

Introduction

1.1 A Broad Overview of the Ionosphere

Earth's ionosphere is a region of the atmosphere populated with <1 eV plasma, which is relatively cold in comparison with other magnetospheric plasmas that can reach energies in the keV and MeV. It extends in altitude from 60 km to ∼1000 km and co-exists with the ∼1200 K rarified neutral atmosphere known as the thermosphere. Ionospheric plasma is considered quasi-neutral — having approximately an equal number of free electrons and positively charged ions — and is primarily produced through the photoionization of neutral atmospheric species, such as O, O_2, N_2, H, He, and NO, by Extreme Ultraviolet (EUV) and soft X-ray solar radiation (λ =∼10-100 nm), but also by the precipitation of energetic particles — mostly keV electrons — above 50° magnetic latitude (notably in the aurora) [*Schunk and Nagy*, 2009].

The ionosphere is important to magnetospheric physics and even to life on Earth, and it is intrinsically connected to the larger space environment: it is the source region for the plasmasphere, makes a significant contribution to the overall content of magnetospheric plasma, and acts as a sink for energetic particles trapped in the Earth's magnetic field when they are deposited into the upper atmosphere and become a source of ionization and the aurora. The ionosphere is also capable of

supporting electric fields and consequently large current systems that produce magnetic disturbances that have been shown to adversely affect large-scale infrastructure such as power distribution lines and substations, gas and oil pipelines, and even animal migratory patterns [e.g., *Belova and Acosta-Avalos*, 2015]. The ionosphere was partly discovered through its effects on radio waves, especially the reflection of certain frequencies and allowing the first trans-atlantic radio communication by Marconi in 1901 [*Schunk and Nagy*, 2009]. During the Cold War, and to some extent continuing to this day, the ionosphere has been used to communicate long distances with submerged submarines via **ELF!** (**ELF!**) radio waves that are ducted by the "ionospheric wave guide" between the ground and bottom of the ionosphere, Over the Horizon (OTH) High Frequency (HF) radar has allowed for the detection of aircraft and ships over much greater distances than is possible with the more commonly used Very High Frequency (VHF) and Ultra High Frequency (UHF) systems thanks to the reflection of HF waves by the ionosphere illustrated in Figure 1.1. With the advent of the space age, it has been found that the ionosphere also affects radio signals transmitted to and from space.

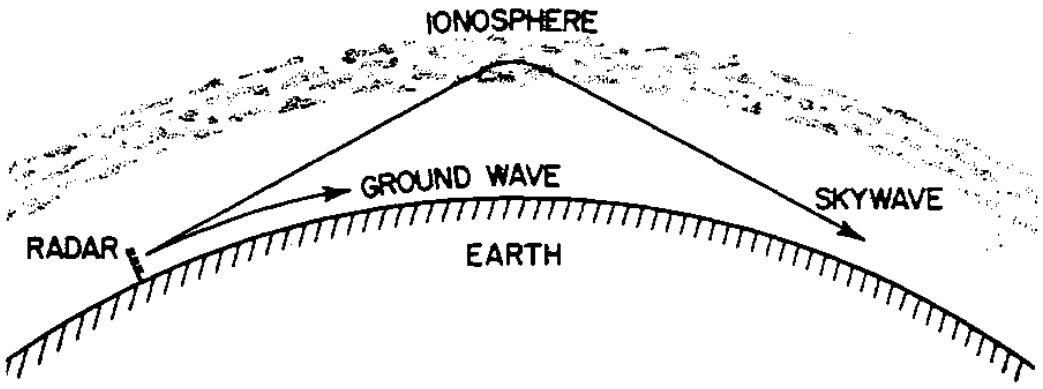

Figure 1.1: Illustration of the ionospheric wave guide "skywave" transmission. From *Headrick and Skolnik* [1974]

1.2 Composition of Earth's Upper Atmosphere

1.2.1 The Neutral Thermosphere

The ionosphere is formed out of the neutral atmosphere which, above ∼100 km, exists at a nearly constant temperature (though changing with solar activity) of ∼1200 K. The mass fraction of the atmosphere is constant up ∼120 km, called the "homopause", mixing rates between neutral species are high enough to maintain an atmosphere that has constant relative composition with height, or sometimes called the "turbopause", because below this altitude the atmospheric composition is dominated by turbulent mixing. Near 120 km the atmospheric density becomes low

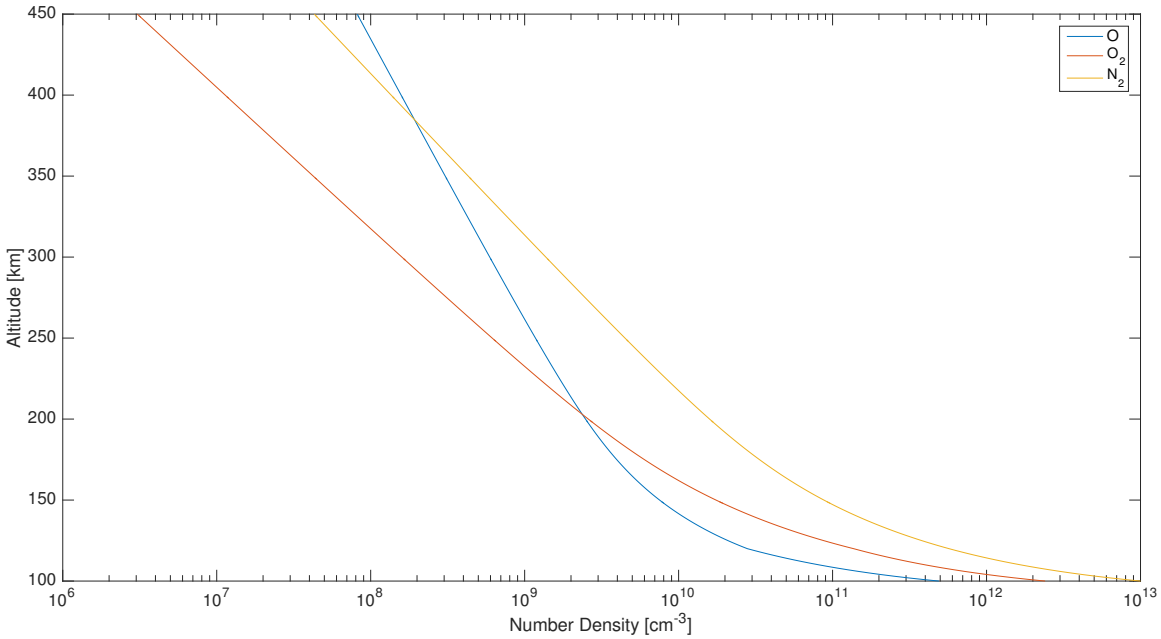

Figure 1.2: Primary neutral consituants (species) of the upper atmosphere at altitudes above the homopause.

enough that the collision rate can no longer keep up with buoyancy and the constituents begin to separate by mass (Figure 1.2). One important point that can be seen in Figure 1.3 is that, at altitudes between 400 and 600 km, atomic oxygen (O) — which is highly reactive, and also corrosive to spacecraft, is the most abundant species.

1.2.2 Earth's Ionosphere

The composition of the ionosphere consists primarily of O^+ ions above ∼150 km and up until ∼1000 km altitude where H^+ becomes more abundant. This transition is what demarcates the ionosphere from the plasmasphere (previously and aptly called the "protonosphere") [*Schunk and Nagy*, 2009]. The remaining major ion species in the ionosphere are O_2^+, NO^+, $N_2{}^+$, and N^+, with He^+ contributing as a minor species above 400 km and H^+ becoming the dominant species in the plasmasphere. Figure 1.3 gives a typical vertical profile of the atmospheric composition for both neutral and ion species above 100 km.

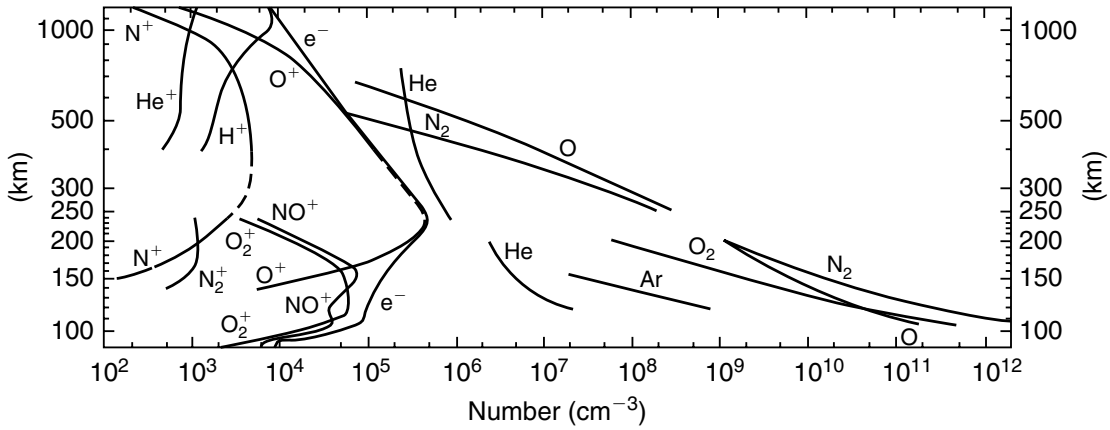

Figure 1.3: Daytime composition measurements of neutral and ion constituents of the upper atmosphere over White Sands, NM during the International Solar Quiet Years (1964-1965). From *Kelley* [2009].

1.3 Organization of the Ionosphere

1.3.1 Vertical Structure

The vertical structure of the ionosphere tends to separate into distinct bands of altitude as illustrated by Figure 1.4. The D, E, F regions of the ionosphere are distinguished by local peaks in ion density corresponding to a specific altitude. The density and composition of the D and E regions are regulated primarily by chemical

interactions while the F region is a balance primarily between chemistry and advection.

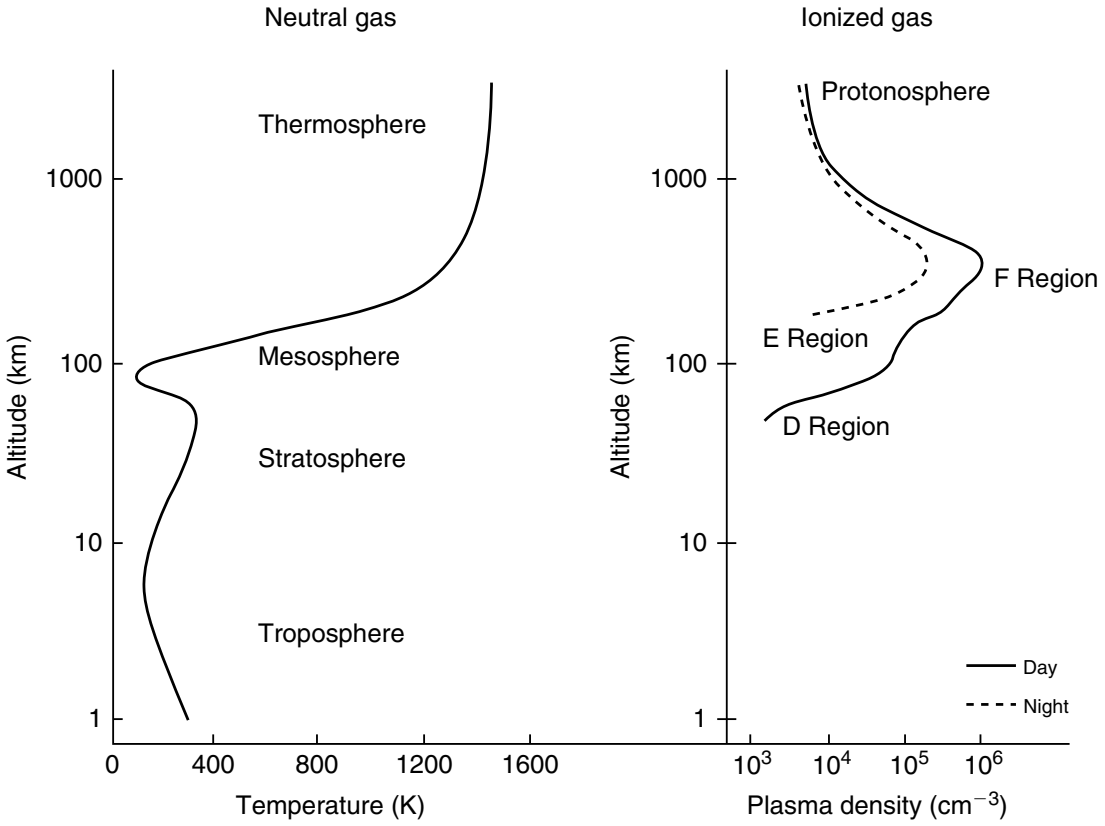

Figure 1.4: Geomagnetically quiet altitude profiles of the neutral and ionized atmosphere in the mid-latitudes. The ionosphere loses its D and E regions during the night to chemical recombination. The secondary "F_1 peak" also disappears during the night, while the F-region persists through the night. From *Kelley* [2009].

D Region The D region is the very lowest altitude regime of the ionosphere and exists below ∼100 km. Because of it's low altitude, the D region exhibits very little ionization and features several bands of rapidly increasing density [*Kelley*, 2009]. It consists primarily of NO^+ ionized by a high flux of low-energy Lyman-α ultraviolet radiation (122 nm) that are only able to ionize the NO due to its low ionization potential (9.264 eV) [*Schunk and Nagy*, 2009]. The D region is the least explored region of the ionosphere owing to its height above the altitude where research balloons can fly and below where spacecraft can maintain a stable orbit and provide

persistent in-situ observations. In fact, most exploration of the D region has been from ground-based ionosondes measuring electron density from the ground and sounding rockets that make fleeting measurements of density, composition, and temperature. One of the more interesting properties of the D region is its absorption of microwave radio waves. During the day, radio waves $\sim$1 MHz (including AM radio) are completely absorbed. However, the D region completely disappears during the night, due to the absence of solar illumination and rapid chemical recombination with the dense neutral atmosphere, and AM radio is able to propagate to higher and denser regions of the ionosphere where it is reflected. This phenomena is often used by amateur radio operators to communicate over distances beyond the horizon and is also observed by early morning AM radio listeners who may occasionally tune in stations from surprisingly great distances.

E Region The E region is defined as the region from 100-150 km. Since the ion densities are $\sim 10^5$ cm^{-3} while the neutral densities are $\sim 10^{12}$ cm^{-3}, the E region is considered to be weakly ionized and the vast majority of ion collisions are between ion and neutral species rather than ion-ion collisions. As can be seen from Figure 1.3, the dominant ions in the E Region are NO^+, O_2^+, and N_2^+. The E region is also where most aurora are observed. Energetic electrons from the solar wind become trapped along closed magnetic field lines near Earth's polar regions and precipitate down the field lines into the neutral atmosphere where they produce the optical emissions known as aurora. In addition to optical emissions, precipitating electrons in the aurora are also a major source of ionization in the E region, having ionization production rates ten times higher than the noon time production in the E region closer to the equator [*Kelley*, 2009].

F Region The F region extends above 150 km and features a density peak near 200 km, known as the F_1 peak, and another, more pronounced F_2 peak at 300 km,

which is the densest altitude layer of the ionosphere and holds the bulk of plasma in the ionospheric density column. Similar to the D and E regions, the F_1 peak undergoes chemical recombination during the night and decreases in density. However, the F_2 peak, though diminished, remains throughout the night due to a variety of factors described in Section 1.4.2.

1.3.2 Meridional Organization

The ionosphere is typically broken into polar, equatorial, and mid-latitudes regions based on magnetic latitude and the distinct phenomena and processes observed in each region.

Polar The polar regions of the ionosphere are defined by their coupling with the magnetopause and the nightside magnetotail plasma sheet and magnetotail. At the highest latitudes, known as the polar cap, the magnetic field lines are open and connected to the solar wind. Through reconnection on the nightside, energetic electrons can be deposited in ionosphere's E region where they produce aurora and form a significant source of ionization. At lower latitudes, the magnetic field lines are closed and more dipolar. The boundary between these regions of open and closed field lines is appropriately called the open/closed field line boundary. The auroral zone is an intermediate region threaded by the open/closed field line boundary. Field lines at poleward edge of the auroral zone close far down the stretched magnetotail while field lines near the equatorward boundary are become more dipolar.

Equatorial The equatorial and low-latitudes are defined by the nearly horizontal geomagnetic field, resulting current systems, and vertical $\mathbf{E} \times \mathbf{B}$ transport, most notably in the equatorial fountain and subsequent equatorial anomaly. During the day, ions are carried vertically by tidal expansion of the thermosphere at the

sub-solar point. These thermospheric winds across magnetic field lines and the resulting eastward dynamo electric field maps to the F region where it drives plasma first up in altitude and then along the horizontal magnetic field lines to form two density peaks on either side of the magnetic equator that are known as the equatorial anomaly.

Mid-latitudes The ionosphere's mid-latitude regions, between 30° and 60°, tend to exhibit a relatively uniform density structure during geomagnetically quiet times that increases and decreases with day and night. The poleward boundary of the mid-latitude ionosphere is the mid-latitude trough (sometimes called the "main trough") that, during geomagnetically quiet times, is a region of low velocity plasma that becomes depleted because of its stagnation long dwell times allowing more plasma to be lost. The trough is also magnetically connected to the plasmapause, and during geomagnetically active times, the enhanced sunward convection erode the plasmapause boundary extending the trough in latitude and convecting the low density plasma sunward.

1.4 Formation

The formation of the ionosphere results from the balance between production rates P (due to photoionization, particle precipitation, and Joule heating) and the loss rate L due to processes that vary within the different altitude regimes of the ionosphere. Neglecting the transport term, $(\nabla \cdot \boldsymbol{v})\, n_e$, the continuity equation for each species can be simplified to Equation 1.1.

$$\frac{\partial n_s}{\partial t} = P_s - L_s \qquad \text{Continuity equation (neglecting transport)} \qquad (1.1)$$

1.4.1 Production

The primary ionization source of the ionosphere is photoionization by EUV and soft X-ray radiation (124 nm to 10 nm). Ion production depends on the intensity of the EUV spectrum, which varies in intensity by wavelength, according to the species' respective absorption cross-section for that wavelength. To a first order, the solar intensity at each wavelength is attenuated by the atmosphere by Equation (1.2) from *Schunk and Nagy* [2009].

$$I(z,\chi)_\lambda = I_{\infty\lambda}\, e^{-H\, n(z)\, \sigma^a_\lambda\, \sec\chi} \tag{1.2}$$

where $I(\infty)_\lambda$ and $I(z,\chi)_\lambda$ are the intensity of a photon of a specific wavelength ("monochromatic") either at the top of the atmosphere ("infinity") or at a given height z above the surface; H is the scale height (e-folding distance) $H = k_b T/m\, g$ according to the mass, m of the atmospheric species, χ is the solar zenith angle of an incident photon, σ^a is the atmospheric species' electromagnetic absorption cross-section at the wavelength, λ, of that photon, and $n(z)$ is the number density of an atmospheric species as an exponential function of altitude: $n(z) = e^{-z/H}$.

The solar flux is computed by integrating the intensity through all solid angles from 0 to 2π steradians and the incident EUV solar spectrum at the top of the atmosphere from the EUV model for Aeronomic Calculations (EUVAC) is shown in Figure 1.5. Table 1.1 lists the energy required to ionize the most abundant neutral species of the upper atmosphere along with the wavelength of the equivalent energy photon.

The term $H\, n(z)\, \sigma^a_\lambda\, \sec\chi$ in Equation (1.2) is often referred to as the optical depth τ and photons deposit the majority of their energy in the atmosphere at the height where $\tau = 1$. Figure 1.6 shows the unity optical depth for EOV wavelengths in Earth's upper atmosphere.

Table 1.1: Ionization Potentials of Most Abundant Thermospheric Species [*Schunk and Nagy*, 2009]

Species	**Energy [eV]**	**Wavelength [nm]**
O	13.62	91.03
O_2	12.06	102.8
N_2	15.58	79.58
He	24.59	50.42
NO	9.264	133.8

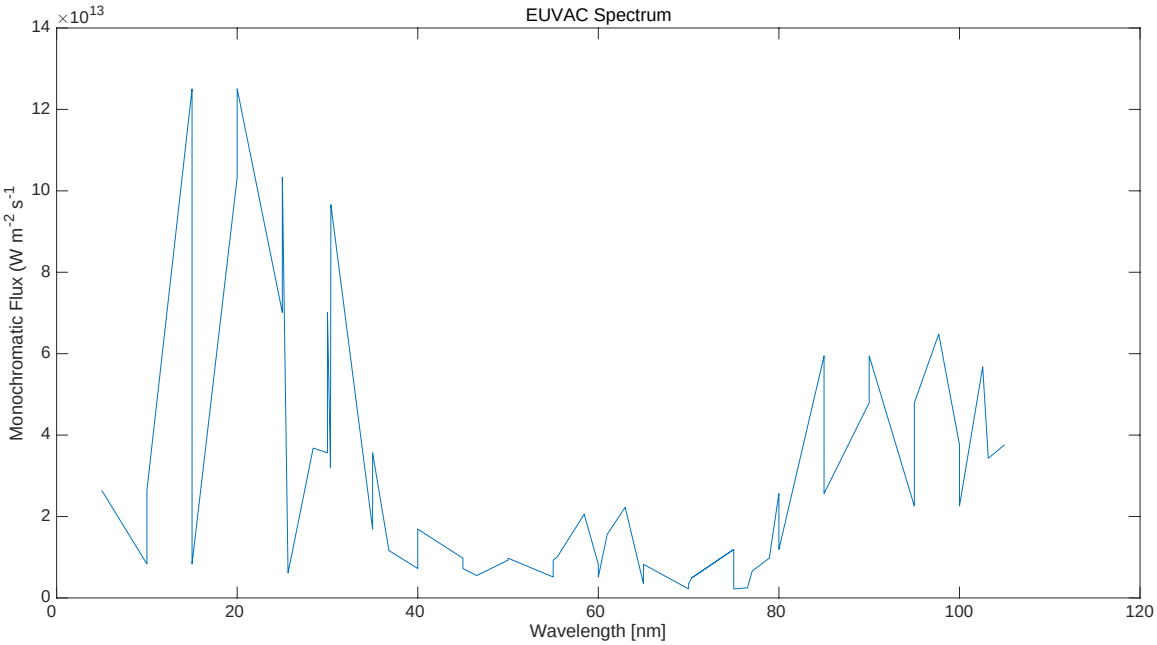

Figure 1.5: The monochromatic intensity (flux per each photon wavelength) of the EUV spectrum of the sun.

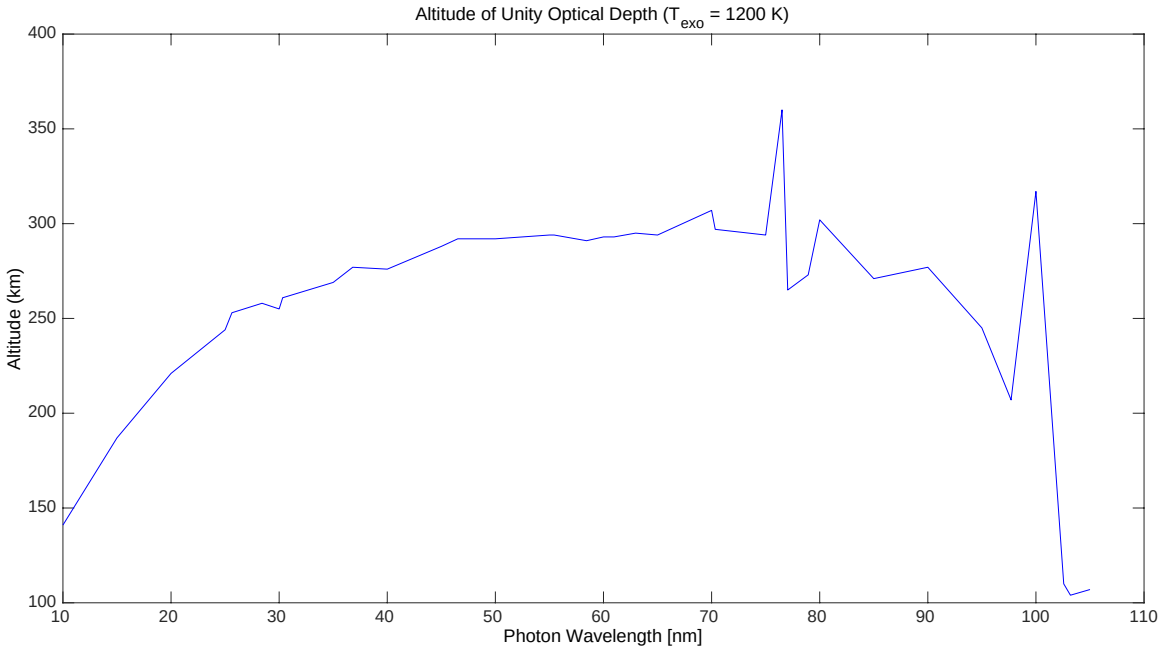

Figure 1.6: Altitude of unity optical depth ($\tau = 1$) for the solar EUV spectrum incident at the top of the atmosphere.

1.4.2 Loss Processes

Generally speaking, plasma is lost from the ionosphere through the chemical processes of dissociative recombination and radiative recombination, with charge exchange playing a roll in enabling some of these chemical reactions. Plasma at low altitudes experiences continuous losses due to chemical reactions with the neutral atmosphere and ion densities decrease dramatically during the night when production through photoionization stops. At higher altitudes, recombination reaction rates are slowed due to the reduced abundance of N_2, which plays a key roll as an intermediate step that enables the high rate dissociative recombination reaction with NO^+. Instead, ion loss at higher altitudes occurs through charge exchange interactions, which are much slower than the dissociative recombination reactions at lower altitudes, and the plasma is able to persist through the night. Table 1.3 gives a variety of chemical processes that play a role in plasma loss from the ionosphere.

Table 1.2: Important Loss Reactions in the Ionosphere

Reaction	**Rate Const. [cm^3s^{-1}]**	**Rx Type**
$NO^+ + e^- \longrightarrow N + O$	$4.0 \times 10^{-7} (300/T_e)^{0.5}$	Dis. Recomb.
$O_2{}^+ + e^- \longrightarrow O + O$	$2.4 \times 10^{-7} (300/T_e)^{0.7}$	Dis. Recomb.
$O^+ + e^- \longrightarrow O + \nu$	$3.7 \times 10^{-12} (250/T_e)^{0.7}$	Rad. Recomb.
$O^+ + O_2 \longrightarrow O + O_2{}^+$	2.1×10^{-11}	Charge Ex.
$O^+ + N_2 \longrightarrow NO^+ + N$	1.2×10^{-12}	Intermediate Process
$O^+ + NO \longrightarrow NO^+ + O$	8.0×10^{-13}	Charge Ex.

In the E region, O^+ is lost in the two-step process of a charge exchange with either O_2 or NO and then one of the dissociative reactions (breaking up and neutralizing the resulting $O_2{}^+$ and NO^+ respectively).

In the F region, O^+ undergoes radiative recombination during which a photon is released in the reaction $O^+ + e^-$. Which, as shown in Table 1.3, is five orders of magnitude slower than dissociative recombination reactions and the reduced N_2 concentration (see Figure 1.2) means even these reactions proceed much more slowly. The lack of molecular species in the F_2 peak and downwelling from the plasmasphere are the primary reasons that it persists through the night.

1.5 Instrumentation for Ionospheric Research

There are a large number and wide variety of instruments that routinely measure properties of the ionosphere from the ground, sub-orbital rockets, and orbital spacecraft. The research described in the subsequent chapters uses three types of instrumentation: Global Positioning System (GPS) Total Electron Content (TEC), radar, and in-situ plasma measurements.

GPS TEC In the past two decades, GPS and more generally Global Navigation Satellite Systems (GNSS) have been used to measure the ionosphere's TEC. TEC is the integrated electron number density, n_e, along a given raypath between points s_1 and s_2 given by Equation 1.3. TEC can be thought of as the total sum of electrons

along a one square meter column through the ionosphere. In the case of GPS and GNSS TEC, this column extends from the transmitting satellite to the receiver. This measurement takes advantage of the dispersive nature of the ionosphere, meaning that electromagnetic waves of different frequencies travel through it at different speeds. The phase velocity of a signal traveling through a plasma (such as the ionosphere), depends on the plasma's electron density as given by Equation 1.4 for an electromagnetic wave of frequency f in a plasma [*Chen*, 1984], where v_ϕ is the wave phase velocity, ω_p is the plasma frequency (given by Equation 1.5), m_e and e are the mass and charge of an electron respectively, and c is the speed of light. From Equations 1.4 and 1.5 — the dependency of propagation time on frequency and density is readily seen.

$$\text{TEC} = \int_{s_1}^{s_2} n_e \, ds \tag{1.3}$$

$$v_\phi^2 = c^2 + \omega_p^2 \frac{f^2}{c^2} \tag{1.4}$$

$$\omega_p^2 = \frac{n_e e^2}{\epsilon_0 m_e} \tag{1.5}$$

The slight difference in transit time between the GPS L1 and GPS L2 frequencies, 1575.42 MHz and 1227.60 MHz respectively, can be used to infer TEC between the transmitting GPS satellite and the receiver, provided the receiver is capable of measuring both channels. *Mannucci et al.* [1993] gives Equation 1.6 as the relationship between the GPS L1 and L2 pseudorange delay and TEC,

$$\text{TEC} = (P_1 - P_2) \cdot 2.852 \times 10^{16} \quad [\text{e}^- \, m^{-2}] \tag{1.6}$$

where P_1 and P_2 represent the pseudorange transit time in nanoseconds measured from the GPS L1 and L2 signals, respectively.

Radar Radar is an important tool in ionospheric research and there are essentially two types of radar used in ionospheric research: coherent and incoherent scatter radars. Coherent scatter radar, such as the type employed in the SuperDARN radar network, is relatively low power (kilowatts) and makes measurements of velocity and range using reflected signals from the ground and decameter size density irregularities in the ionosphere. It requires the presence of the irregularities to return a signal, otherwise nothing is returned. Incoherent scatter radar makes measurements of electron density, velocity and temperature of electrons in the ionosphere by measuring the reflected intensity, Doppler shift, and Doppler broadening of a high power (megawatts) pulse at a range determined by the signal's round-trip time-of-flight.

Defense Meteorological Satellite Program (DMSP) In addition to terrestrial weather, DMSP satellites measure several parameters relevant to ionospheric research including ion and electron flux, energy, electric fields, and electric current flux. Four DMSP satellites are at 830 km altitude in sun-synchronous orbit (98.8° inclination) giving them an orbital period of 101 minutes [*NOAA/NGDC - Earth Observation Group - Defense Meteorological Satellite Progam*]. DMSP measurements are used in the research described in Chapters III and IV to identify the equatorward edge of the auroral zone.

1.6 Geomagnetic Storms

1.6.1 Origin of Geomagnetic Storms

The origin of geomagnetic storms lies ultimately in the sun. As plasma streams out radially from the solar corona, in what is known as the solar wind, it carries with it the heliospheric magnetic field, also known as the Interplanetary Magnetic Field (IMF). The orientation of the IMF at Earth, is described in components: x

toward the sun from Earth, z north out of the ecliptic plane, and y completing the right hand rule — pointing opposite the Earth's trajectory around the sun. The speed, orientation, density, and magnetism of the solar wind is extremely complex in detail, owing to the twisted and dynamic configuration of the sun's magnetic fields, but the magnetic structure can be described with the simplified spiral first developed by *Parker* [1958]. As the solar wind moves radially away from the rotating sun, it traces out a spiral pattern much like that of a lawn sprinkler. In three dimensions, the IMF current sheet, formed between oppositely directed IMF field lines ($\nabla \times \boldsymbol{B} = \mu_0 \boldsymbol{J}$), takes on a shape that has been likened to a ballerina skirt as illustrated in Figure 1.7. The tilting of this sheet gives rise to instances of southward IMF which can produce storms. Additionally, the ever changing dynamics of the sun over the eleven-year solar cycle, gives rise to a high degree of variability including high speed solar wind streams, coronal mass ejections, and shock waves. The interaction with these disturbances in the solar wind varies with density, pressure, temperature, and orientation of the IMF. It has been shown that a southward oriented IMF z component, $B_z < 0$, is especially effective in producing geomagnetic storms [e.g., *Zhang and Moldwin*, 2014]. The mechanism for the geoeffectiveness of the IMF was first described by *Dungey* [1961] through a process now known as magnetic reconnection (Figure 1.8). Reconnection occurs when a southward IMF first encounters the Earth's magnetic field at the equatorial subsolar point of the magnetopause (the magnetic pressure balance point between the IMF and the terrestrial magnetic field), which here is oppositely oriented northward. Because of this discrepancy in magnetic orientation the magnetic field diffuse into one another and merge, opening the magnetosphere to the solar wind. The reconnected terrestrial magnetic field lines are now convected with the solar wind over the Earth dragging ionospheric plasma with them across the polar cap. Downstream on the Earth's night side, stretched open field lines from the north and

south poles become nearly parallel and are driven closer together by a magnetic tension force until they reconnect and return toward the Earth and a more dipolar configuration. The ionospheric footprints of this process, in the simplest case, trace out the two-cell plasma convection pattern in the polar cap shown in Figure 1.9. Meanwhile, the motion of the magnetized solar wind produces an electric field ($\mathbf{E} = -\mathbf{v} \times \mathbf{B}$) across the magnetopause from dawn to dusk. When the reconnection point penetrates deeper into the magnetosphere, due to a disturbance in the solar wind, such as a CME or shock, the open/closed field line boundary and auroral oval move to lower latitudes, and convection across the polar cap is enhanced, while the convection electric field is enhanced. As the plasma moves toward Earth, it experiences a longitudinal drift due to the radial gradient in the magnetic field and its curvature. The resulting gradient-curvature drift is charge dependent and so positive ions and electrons drift in opposite directions around the Earth. This charge separation gives rise to what is known as the ring current.

1.6.2 Storm Disturbance Indices (Dst and $\mathbf{K_p}$)

Disturbance Storm Time (Dst) The Dst index is one of the most used measures of disturbances to Earth's magnetic field. It represents the ground disturbance to the Earth's magnetic field at the geomagnetic equator (driven by changes in the ring current, as described in Section 1.6.1 and is computed from hourly measurements of the horizontal component H of the geomagnetic field at four observatories distributed longitudinally around the globe on both sides of the geomagnetic equator. Figure 1.10 shows the locations of stations at Hermanus South Africa, Kakioka Japan, Honolulu Hawaii, and San Juan Puerto Rico [*Sugiura et al.*, 1991]. The background solar quiet (S_q) daily variation is subtracted from magnetic H measurements at each station (Equation (1.7)), which are normalized by the cosine of their magnetic latitude ϕ. Dst is then computed (Equation (1.8)) as

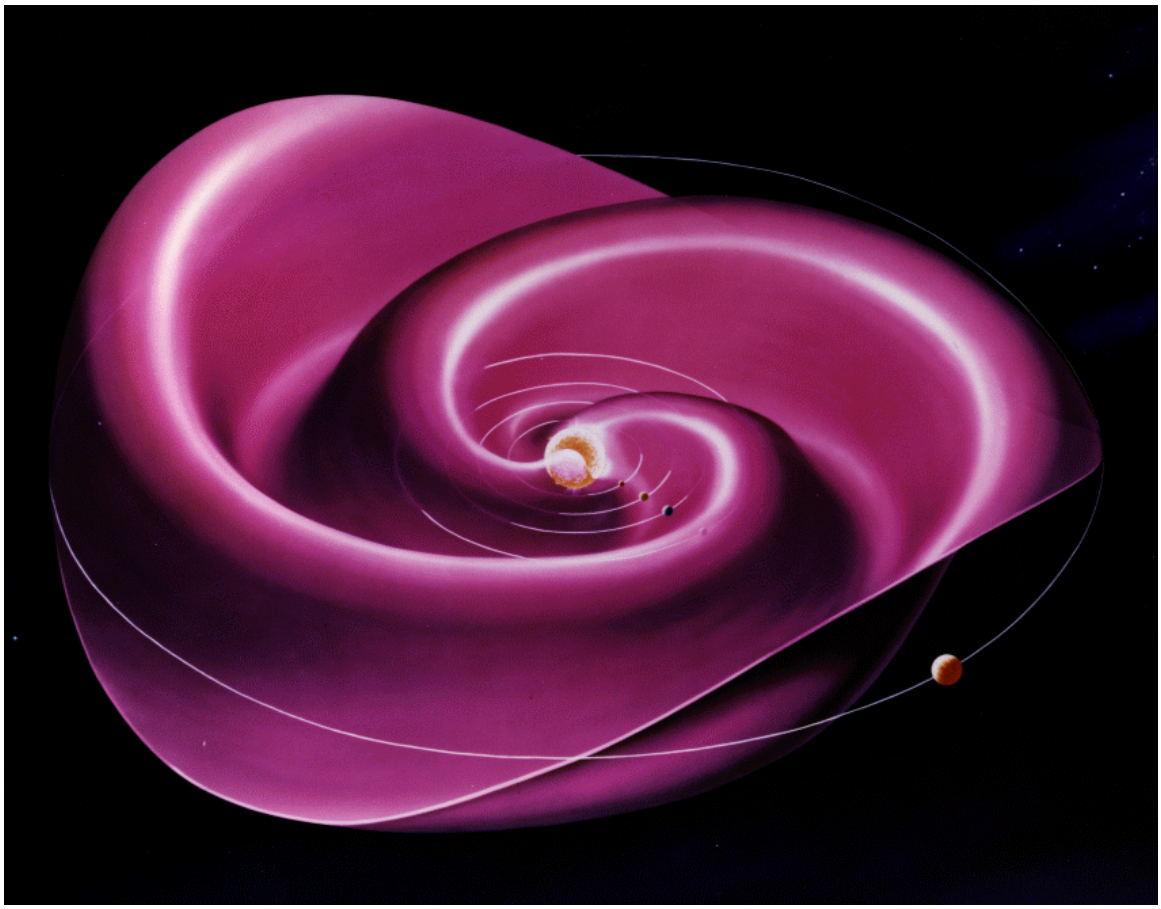

Figure 1.7: The three-dimensional Parker Spiral and resulting current sheet. The IMF is directed radially away from the sun above the current sheet and toward the sun below. Meanwhile it is drawn into a spiral shape by the rotation of the sun.

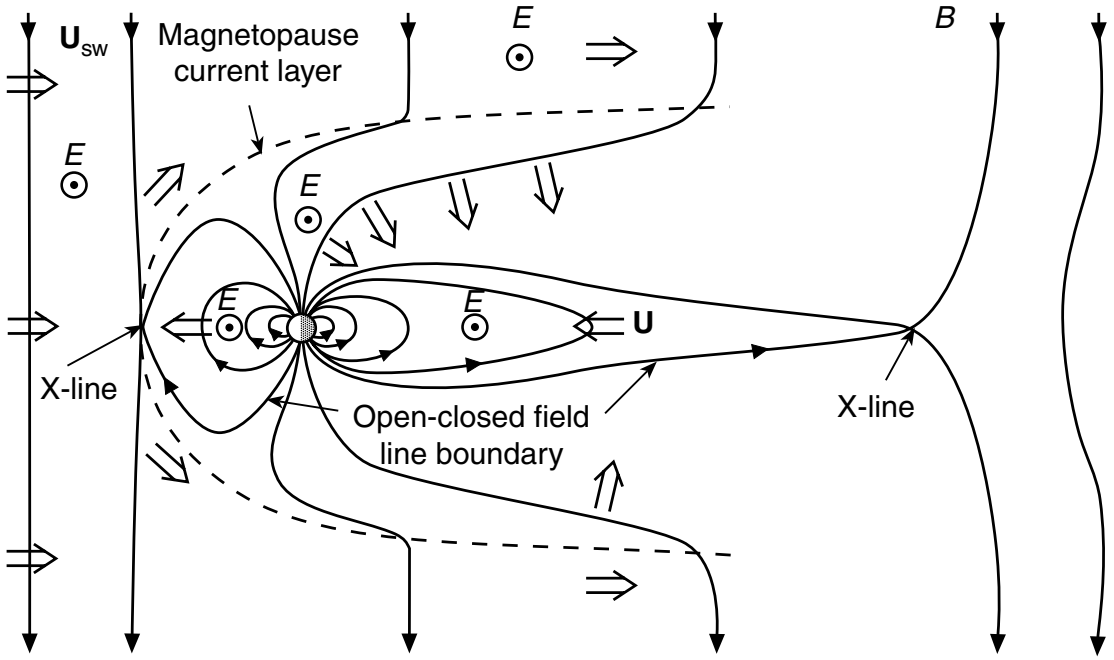

Figure 1.8: Schematic of the open magnetosphere and magnetic reconnection proposed by Dungey, taken from *Schunk and Nagy* [2009]

the average of the normalized disturbance variations $D(t)$.

$$D(t) = \Delta H(t) - S_q(t) \tag{1.7}$$

$$\mathrm{Dst}(t) = \frac{D(t)}{\cos\phi} \tag{1.8}$$

Planetary K Index ($\mathbf{K_p}$) The K_p describes geomagnetic disturbances on a three hour cadence. One of the ways that is used to describe the geomagnetic field at a point on Earth's surface is in x, y, and z components where the x (north) and y (east) components are tangent to the surface, and z is radially inward completing the right hand rule. The K-index is derived locally from observations of

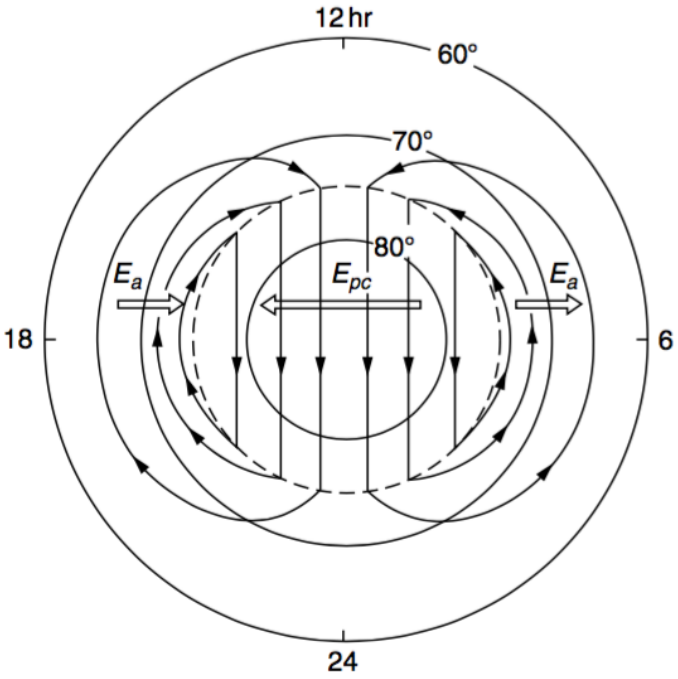

Figure 1.9: Simplified two-cell convection pattern in the polar cap. Plasma is convected from noon to midnight by reconnected magnetic field lines and returned along field lines connected to the ring current after they have undergone reconnection in Earth's nightside magnetotail.

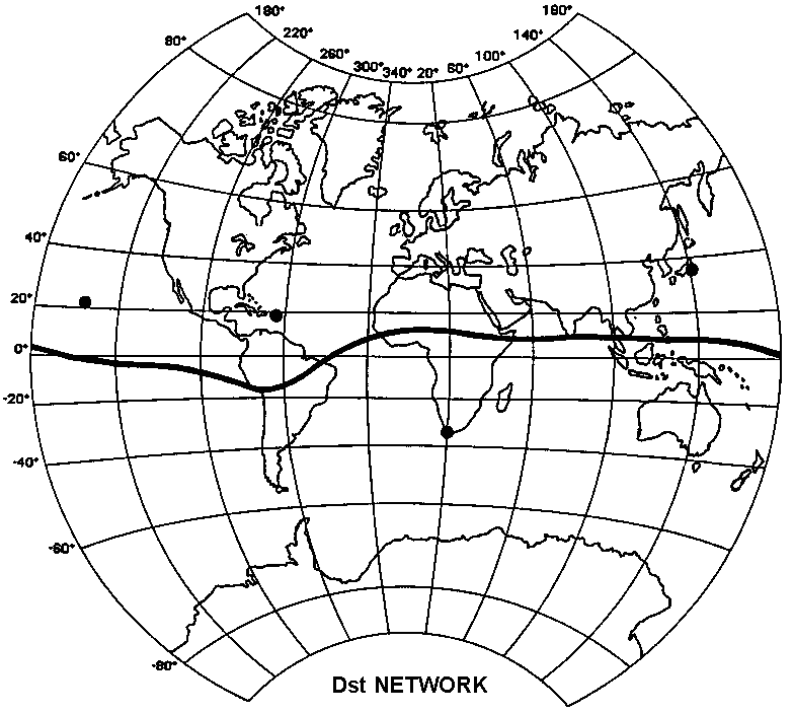

Figure 1.10: Dst Stations from left to right: Honolulu Hawaii, San Juan Puerto Rico, Hermanus South Africa, and Kakioka Japan. Image from *Sugiura et al.* [1991].

disturbances to the horizontal components at thirteen mid-latitude stations (44° to -60° geomagnetic latitude) around the world and which are then averaged to produce a the planetary K_p index.

The official K_p index proposed by Julius Bartels in 1938 is a semi-logarithmic scale assigning values in a one third integer sequence as: 0, 0+, -1,1o,1+... with subscripts -,o, and + to indicate thirds rather than decimals. National Oceanic and Atmospheric Administration (NOAA) publishes a integer logarithmic K_p index (analogous to the Richter scale) from 0-9 as an indicator that alerts potentially affected users to the level of geomagnetic activity. In general K_p = 0-3 is considered to be "geomagnetically quiet", K_p = 4 is considered "active", and K_p= 5-9 is considered "geomagnetic storm conditions".

1.6.3 Geomagetic Effects on the Mid-latitude Ionosphere

Geomagnetic storms have been shown to drive structural changes in the Earth's ionosphere that deviate dramatically from the typical quiet-time conditions [e.g., *Foster and Rideout*, 2005]. Observations of TEC have revealed that some of the most dramatic changes are the Storm Enhanced Density (SED) plumes that occur in the mid-latitude ionosphere [e.g., *Foster*, 1993; *Kelley et al.*, 2004; *Zou et al.*, 2013, 2014], where steep density gradients along the plumes' edges can produce a cascade of small-scale density irregularities and subsequently, a potentially worsening scintillation environment for GNSS such as GPS , and space-based communication users. Small-scale ($\sim$1 km) variations (or irregularities) in ionospheric electron density correspond to the Fresnel radius of radio frequencies between 100 MHz - 3 GHz for a receiver on the ground. Consequently, these irregularities can have dramatic impacts on space-based systems operating in this frequency range such as signal degradation, GNSS loss-of-lock, dropped data packets, or total inoperability [*Datta-Barua et al.*, 2014; *Doherty et al.*, 2004; *Datta-Barua et al.*, 2003]. The

phenomenology of small-scale irregularities at mid-latitudes, and their potential to cause radio scintillation, is an open and active area of ongoing research.

SED Plumes In the past two decades, observations from incoherent scatter radar and GPS TEC from dense arrays of GPS receivers have revealed large-scale features in ionospheric density in response to strong (-100 nT) geomagnetic storms. *Anderson* [1976] successfully modeled what was then called the positive and negative phases of ionospheric storms with a combination of an equatorward neutral wind carrying plasma up the inclined magnetic field lines at mid-latitudes — thereby reducing their loss rate to chemical recombination, and the influence of a northward directed electric field that drives plasma in the dusk sector sunward. Later, *Foster* [1993] described observations of SED from Millstone Hill incoherent scatter radar as latitudinally narrow regions of enhanced density plasma with an elevated F region peak altitude and enhanced sunward convection steepening the poleward gradient of the SED plume. *Foster et al.* [2002] later showed that the SED plume was connected to the plasmaspheric plume simultaneously observed in EUV images from the IMAGE spacecraft (Figures 1.11 and 1.12). *Kelley et al.* [2004] suggested SED has its roots in an enhanced equatorial fountain effect that is then pushed poleward by a penetrating zonal electric field and a poleward electric field that drives plasma toward the dayside and *Coster et al.* [2007] found in a survey of all longitudinal sectors that SED production coincided with the overlapping of the poleward Sub-auroral Polarization Stream (SAPS) electric field and the plasmapause boundary, further supporting the connection between ionospheric SED and plasmasphere. Furthermore, *Coster et al.* [2007] found the the mechanism behind SED production can last 15-20 hours, which could extend its occurrence through all phases of a geomagnetic storm. Nevertheless, a debate continues about the nature of SED formation, as *Huang et al.* [2005] observed that the enhanced

fountain effect could not account for the observed positive storm phase observed at high latitudes such as over Millstone Hill, and *Deng and Ridley* [2006] suggested that such enhancements were due to enhanced vertical flows which can drive plasma up in altitude along non-vertical magnetic field lines and thereby reducing the loss rate due to a diminished O/N_2 ratio and continuing photoionization on the dayside and equatorward thermospheric expansion in the auroral zone can also drive plasma to higher altitudes contributing to enhanced density in a similar way [*Zou et al.*, 2013] .

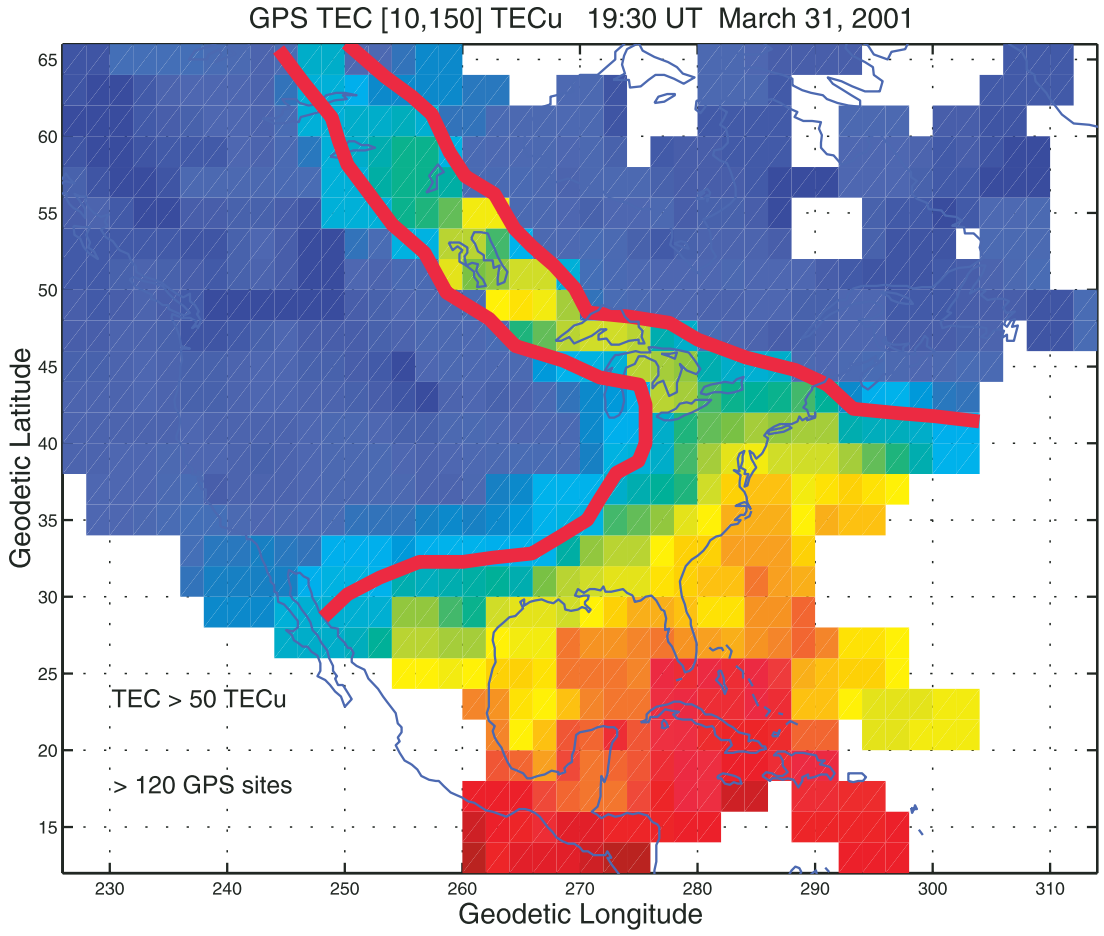

Figure 1.11: SED plume in VTEC with the bounding gradient contours outlined in red (from *Foster et al.* [2002]).

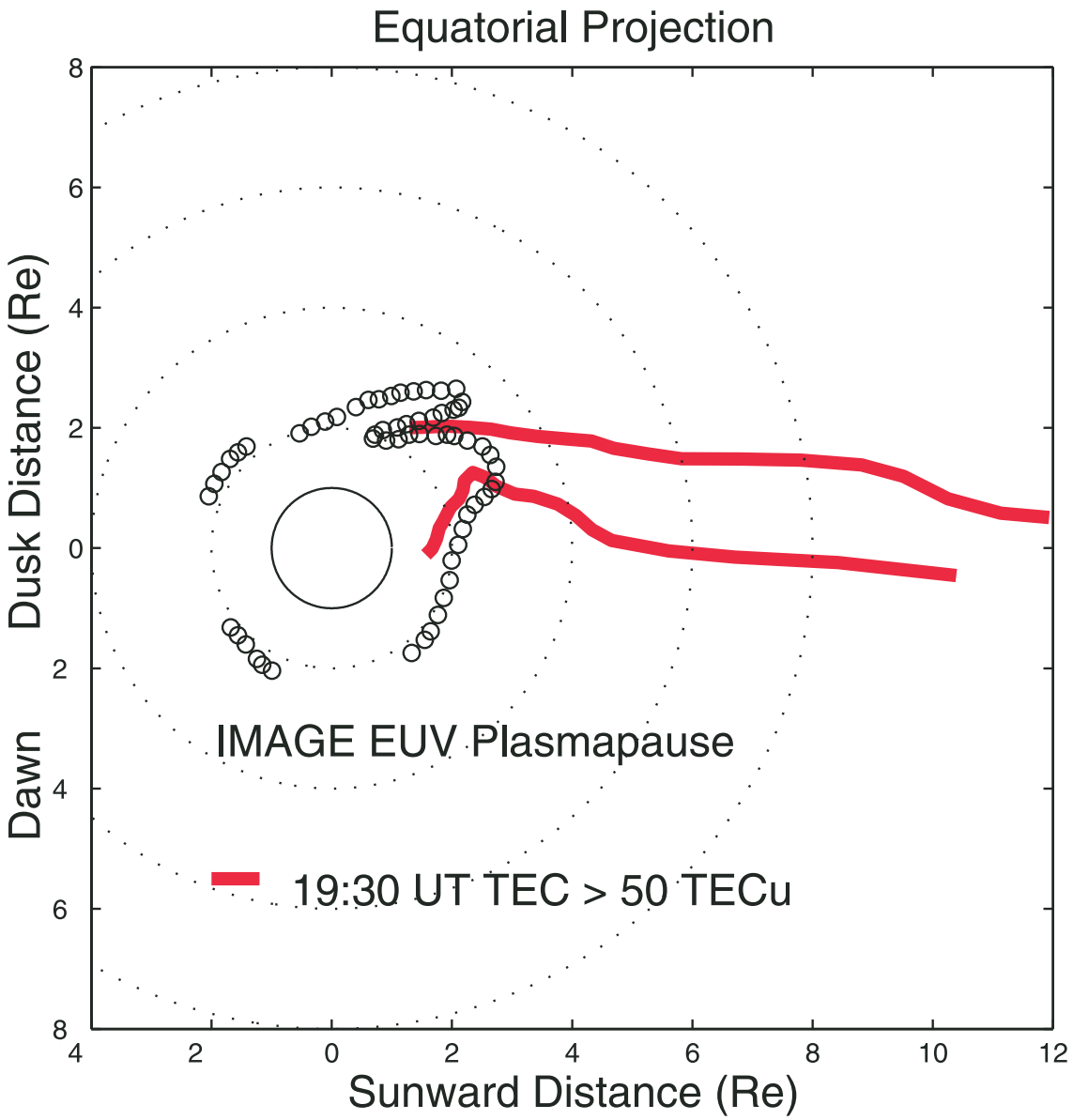

Figure 1.12: SED plume boundaries mapped to equatorial plane of the plasmasphere (from *Foster et al.* [2002]).

1.7 Ionospheric Irregularities

Ionospheric irregularities are localized changes in ion density that are produced through a number of processes and vary in size from a centimeters, in the case of those produced by auroral precipitation, to tens of kilometers as in the case of equatorial bubbles. The density change in irregularities can vary from a few percent to an order of magnitude for the largest irregularities.

1.7.1 Kilometer-Scale Irregularities and Radio Scintillation

Ionospheric density irregularities between several hundreds of meters to a few tens of kilometers in length are of specific interest both from a scientific and societal standpoint. Radio wave scintillation has been shown to occur when electromagnetic waves are scattered by ionospheric density irregularities the order of the characteristic Fresnel size [*Ledvina et al.*, 2002]. The scattering produces a diffraction pattern at distances corresponding to the integer Fresnel zones (integer interference zones with π phase shift), and this can result in fluctuations in Signal-to-Noise Ratio (SNR) as the diffraction pattern passes over the observer. For GNSS receivers, the sudden drop in SNR can cause the receiver's phase tracking loop to lose lock (i.e., cycle count) and introduce range errors. These occurrences are referred to as phase cycle slips and are discussed in greater detail in Section 4.2. The first Fresnel zone for the GPS L1 and L2 frequencies occurs on the ground for typical F peak altitudes ($\sim$300 km) and characteristic Fresnel sizes $\sim$300 m. Ionospheric density irregularities $\sim$1 km have corresponding first Fresnel zones at ground level for a large portion of the HF radio spectrum used for modern communication and signaling technology. The characteristic size, a, of irregularities at the first Fresnel zone as a function of distance from irregularity to the observer is given in Equation (1.9), where n_{Fres} is the integer Fresnel zone number, λ is the radio wavelength, and z is the distance from the aperture (irregularity) to the

observer.

$$a = \sqrt{n_{Fres}\,\lambda\,z} \tag{1.9}$$

Figure 1.13 illustrates the range of characteristic Fresnel scales that produce their first Fresnel zone for a observer depending on the distance from the irregularity (plotted from 200-400 km) for frequencies from 1-1000 MHz. Small-scale ionospheric irregularities at the Fresnel scale are the primary source HF scintillation and can have a dramatic effect on satellite-based communication and navigation systems that often operate in this frequency range and higher. Scintillation from ionospheric density irregularities has been shown to produce up to 20 dB signal fade at the GPS L1 (1575 MHz) frequency and in HF and VHF communications [e.g., *Basu and Groves*, 2001; *Ledvina et al.*, 2002; *Seo et al.*, 2011].

Scintillation is typically thought to be infrequent in the mid-latitude ionosphere, as illustrated in Figure 1.14 by *Basu and Groves* [2001]. However, during geomagnetic storms, regions of enhanced ionization are increasingly observed in the American Sector beginning at equatorial latitudes, stretching poleward and towards noon across mid-latitudes, with similar enhancements observed beginning at higher latitudes in the European and Asian Sectors [*Yizengaw et al.*, 2008; *Zou et al.*, 2014]. These SED regions have steep density gradients along their flanks that can produce a cascade of small-scale density structure (irregularities) and a worsened scintillation environment [*Foster and Rideout*, 2005].

1.7.2 Irregularity Formation Processes

The origins of kilometer-scale irregularities at mid-latitudes owe to three potential sources. In the first, spatially structured and temporally variable particle precipitation produces localized small-scale structure in the E and F regions of the

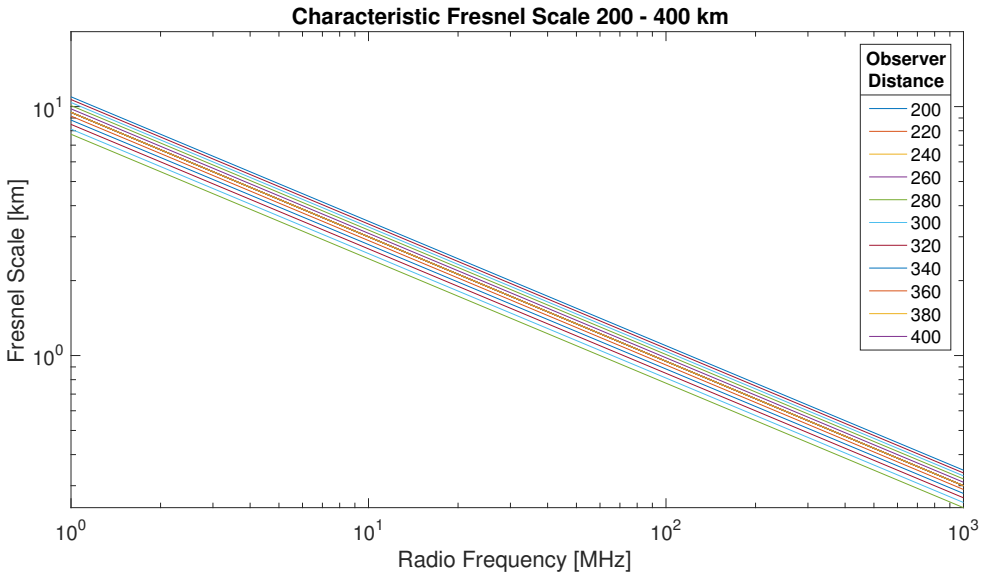

Figure 1.13: Characteristic Fresnel length scale for radio frequencies from 1 - 1000 MHz (HF to L-Band) at observer distances from 200 - 400 km.

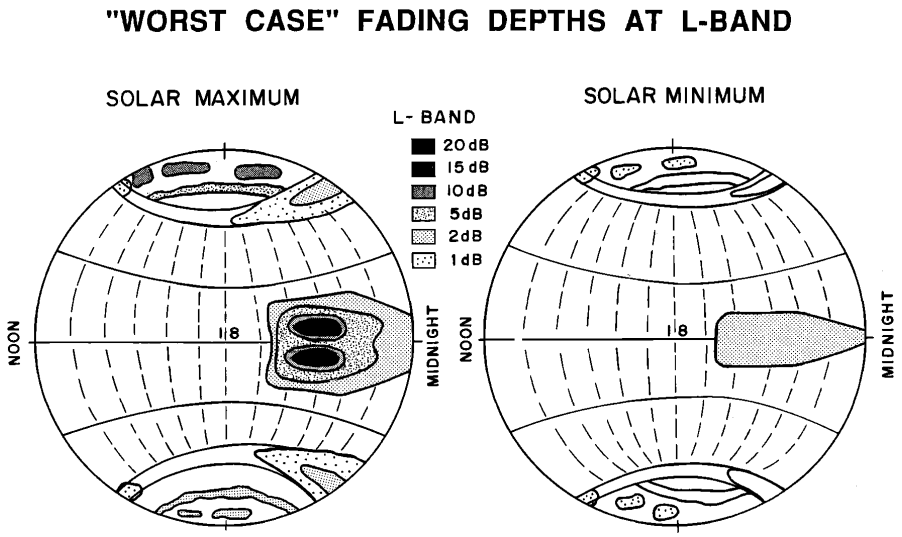

Figure 1.14: Schematic representation of global scintillation effects for L-band frequencies during solar maximum (left) and minimum (right) *Basu and Groves* [2001]. Notice the absence of L-band scintillation at mid-latitudes.

auroral zone. [Schunk and Nagy, 2009]. In the second, it has been suggested that small-scale (<20 km) irregularities are generated near the SED plume by a horizontal Rayleigh-Taylor instability (also known as the gradient drift instability) caused by the motion of lower density plasma moving parallel to the density gradient that is unstable when $(\boldsymbol{E} \times \boldsymbol{B}) \cdot \nabla n > 0$ [*Simon*, 1963; *Kelley*, 2009] . Finally, in the third, by a Kelvin-Helmholtz instability (shear instability) [Hargreaves, 1992] at the interface between to fluids at different velocities. The critical velocity difference between the fluids (assuming a magnetic field parallel to the gradient vector) is given by:

$$(\Delta V)^2 = \left(\frac{1}{\rho_1} + \frac{1}{\rho_2}\right) \frac{|B_1|^2 + |B_2|^2}{\mu_0} \tag{1.10}$$

1.8 Previous Work on SED and Small-Scale Mid-latitude Irregularities

Table 1.3: Important Loss Reactions in the Ionosphere

Reaction	**Rate Const. [$\mathbf{cm^3 s^{-1}}$]**	**Rx Type**
$NO^+ + e^- \longrightarrow N + O$	$4.0 \times 10^{-7} (300/T_e)^{0.5}$	Dis. Recomb.
${O_2}^+ + e^- \longrightarrow O + O$	$2.4 \times 10^{-7} (300/T_e)^{0.7}$	Dis. Recomb.
$O^+ + e^- \longrightarrow O + \nu$	$3.7 \times 10^{-12} (250/T_e)^{0.7}$	Rad. Recomb.
$O^+ + O_2 \longrightarrow O + {O_2}^+$	2.1×10^{-11}	Charge Ex.
$O^+ + N_2 \longrightarrow NO^+ + N$	1.2×10^{-12}	Intermediate Process
$O^+ + NO \longrightarrow NO^+ + O$	8.0×10^{-13}	Charge Ex.

Doherty et al. [2004] reported the impact of SED gradients on Federal Aviation Administration (FAA) Wide-area Augmentation System (WAAS) during the October/November 2003 “Halloween Storms" in which the WAAS Vertical Navigation System (VNAV) system was inoperable for more than 28 hours over a two day period. *Basu et al.* [2008] looked at a geomagnetic storm 7-8 November 2004 with a minimum Dst of -394 nT. They observed mid-latitude GNSS disruption

due to irregularities from an expanding auroral oval and nightime SAPS.

Datta-Barua et al. [2014] also described the impact on the WAAS during 24-25 October 2011 and 9 October 2012 geomagnetic storms that included reduced service coverage over the continental United States lasting several hours and anomalous receiver tracking due to ionospheric scintillation.

Coster [2007] reported the impact of TEC variability on the performance of key infrastructure, including WAAS, and specifically the impact of TEC gradients. Using observations of GPS tracks crossing SED plumes, *Coster* [2007] observed the TEC gradients near SED plumes can exhibit differing degrees of variability and even between the poleward and equatorward gradients.

Sun et al. [2013] analyzed the formation of irregularities associated with North American SED plumes during geomagnetic storms on 31 March 2001 (Dst = -387 nT) and 30 October 2003 (Dst = -383 nT). In their study, the presence of irregularities was indicated in TEC maps with 0.5° x 1.0° resolution using a 30 s Rate of TEC (ROT) and the ROT Index (ROTI) formulated by *Pi et al.* [1997] at each grid point. ROT and ROTI are defined as the differential VTEC between time steps converted to TEC units per minute (TECU/min), where a TECU = 1×10^{16} electrons m^{-2}, and the standard deviation of the ROT over a specified time interval — commonly 5 minutes. *Sun et al.* [2013] observed that irregularities were most present along the poleward boundary of the SED — along the low density trough — and that the irregularity intensity increased with steepening TEC gradients in some cases. They concluded that the formation of irregularities appeared to depend on both steep TEC gradients and strong ion drifts (1-2 km s^{-1}) as favorable conditions. However, while they identified the presence of irregularities and the gradients associated with ROTI, they did not specify the length-scale of irregularities present in each grid cell or the impact on GPS .

Recent work by *Liu et al.* [2016], that characterized the density profile of the SED

plume during 17-March-2015 geomagnetic storm discussed in this paper, observed an increased HmF_2 , but decreased NmF_2 with increased electron temperatures and observed that the SED plume occurred within a diminished NmF_2 , but an enhanced top-side ionosphere. This suggests that the detected irregularities may be occurring high in the ionosphere and may even be generated in the top-side ionosphere or plasmasphere.

1.9 Road Map

The small-scale density structure of the storm-time, mid-latitude ionosphere is a crucial observation needed to understand the space weather effects on key space-based infrastructure, especially communication and navigation systems. Though these systems are generally unaffected by the mid-latitude ionosphere, there can be significant technological impacts during strong geomagnetic storms. Storm Enhanced Density (SED) plumes and the sub-auroral polarization stream (SAPS) can generate radio-disrupting ionospheric density irregularities [*Foster and Burke*, 2002; *Basu et al.*, 2008] that produce up to 20 dB signal fade at the Global Positioning System (GPS) L1 (1575 MHz) frequency and scintillations in HF and VHF communications [*Basu and Groves*, 2001; *Ledvina et al.*, 2002; *Seo et al.*, 2011]. The subsequent chapters present a study of small-scale ionospheric irregularities associated with SED and identify some of the next questions in understanding stormtime small-scale variability. Chapter II describes the new methodology that has been developed to analyze variability in TEC data, and is used the Chapter III case study of small-scale variability during the 17 March 2015 geomagnetic storm, which has been submitted in [*Heine et al.*, 2016]. Chapter II also presents a simulation study developed to validate this new methodology and ChapterIV, presents a survey of small-scale variability associated with SED in twelve geomagnetic storms observed by the ANNA GPS receiver since the author

completed its installation in 2012. Chapter V describes a CubeSat mission concept to investigate small-scale ionospheric irregularities that was published in *Heine et al.* [2015]. Chapter VI concludes with a summary of the major findings of this work and describes future work to explore stormtime mid-latitude small-scale irregularities.

CHAPTER II

Detecting the Ionosphere's Small-Scale Structure

The small-scale density structure of the storm-time, mid-latitude ionosphere is a crucial observation needed to understand the space weather effects on key space-based infrastructure, especially communication and navigation systems. Though these systems are generally unaffected by the mid-latitude ionosphere, there can be significant technological impacts during strong geomagnetic storms. SED plumes and storm-time convection flows [*Basu et al.*, 2008] can generate radio-disrupting ionospheric density irregularities that produce up to 20 dB signal fade at the GPS L1 (1575 MHz) frequency and scintillations in HF and VHF communications [*Basu and Groves*, 2001; *Ledvina et al.*, 2002; *Seo et al.*, 2011]. This chapter describes the methodology used for the case study presented in Chapter III, published in *Heine et al.* [2016], and the broader survey of geomagnetic storms in Chapter IV.

2.1 Small-Scale Irregularity Observations from a Single Station Total Electron Content

2.1.1 Slant and Vertical TEC

Slant Total Electron Content was measured using a Trimble NetR9 dual-frequency GPS receiver "ANNA" located in Ann Arbor, Michigan (42.29 N, -83.71 E Geodetic; 53.31 N, -10.34 E CGM) — often in the path of the SED plume. The Slant Total Electron Content (STEC) is converted to the local VTEC at the Ionospheric Pierce Point (IPP) using a spherical mapping function. IPPs are defined as the point of intersection between a GPS signal path and the altitude of the ionospheric F-peak, which is approximated as a spherical shell at 300 km altitude (see Figure 2.1 . Measurements are made at sample rate of 1 Hz with a post-processing elevation mask of 20° is applied to reduce errors from the vertical mapping function and obstructions near the horizon.

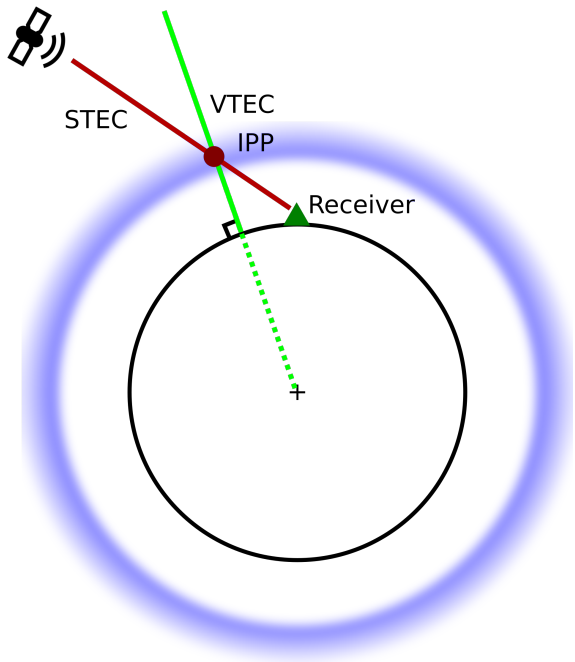

Figure 2.1: Slant Total Electron Content, measured along the red path, is mapped to the local vertical of the IPP to estimate the VTEC (green path). Most of the TEC comes from the F region (blue band).

2.1.2 Receiver Bias Estimation

TEC is derived from the differential pseudorange using Equation 1.5. However there several sources of error and uncertainty in the measured quantities P_1 and P_2. First, there are clock biases on both the satellite and the receiver which do not depend on frequency and therefore can be removed by differencing the L1 and L2 signals. Second, there are electronics implementation biases on the satellite and the receiver which are frequency dependent and and therefore must be accounted for. Furthermore, the satellite and receiver biases change over time and must be updated on a daily basis. Fortunately, NASA's Jet Propulsion Laboratory (JPL) publishes estimates of satellite biases for the GPS constellation that are updated every daily. The receiver bias however, can also vary from day to day and must be estimated for each measurement interval.

The receiver bias for station ANNA is calculated though a minimum variance algorithm that seeks a constant offset that minimizes the variance in STEC between each GPS satellite being tracked at a given time. This is recalculated every 30 s and applied to the STEC. This method makes one crucial assumption, and that is that all of the STEC measurements at a given time are seeing the same "truth" TEC and receiver bias accounts for the difference. This is reasonable because during geomagnetically quiet periods, the mid-latitude ionosphere is uniform in VTEC $\pm$ 5 TECU. However, this is not the case during periods of active geomagnetic conditions where the ionosphere is highly variable on the scale of the receiver's field of view, such as in the presence of large TEC gradients, like SED plumes. Therefore, receiver biases for adjacent quiet days should be used instead.

2.1.3 Code and Carrier Phase Leveling

The TEC calculation in Equation (1.5) is actually performed twice: first using the P code pseudorange which is accurate in terms of absolute TEC , but noisy (see

Figure 2.2), and again using the carrier phase, which is precise, but has an ambiguous starting offset in the carrier cycle count. By combining the two measurements, the carrier phase TEC can be "leveled" by adjusting to a least squares fit of the code phase measurement to remove the cycle ambiguity and produce a precise and accurate measurement of the TEC.

2.1.4 Map Interpolation

GPS based TEC maps downloaded from the Madrigal archival site at Millstone Hill, MA provide global maps of TEC on a $1^\circ \times 1^\circ$ spatial grid that are updated every five minutes. These maps were fit onto a $1/6^\circ$ x $1/6^\circ$ subgrid mesh using bi-cubic spline interpolation — a common image sharpening technique. The interpolated map clearly defines features larger than the original $1^\circ \times 1^\circ$ resolution, such as the location and boundaries of the SED plume, trough, and auroral enhancement during most storm intervals including the 17 March 2015 storm, which is studied in Chapter III . Due to interpolation, the certainty of structural dimensions appearing less than a degree in scale, such as the plume boundary's thickness, is questionable, however structure with dimensions larger than a degree, such as the plume boundary's location and length, are reasonably defined using this technique.

2.1.5 IPP Tracks

GPS pseudo random noise (PRN) codes — assigned 1-32 to each of the currently operational GPS spacecraft — are used to identify individual satellites and their associated IPP. The small-scale density structure can be determined from TEC measurements of individual GPS receivers to each visible GPS satellite, such as those shown in Figure 3.3b. High-rate (1 Hz) individual receiver TEC data such as these, are available from University of Michigan receiver upon request and from the Madrigal database. These measurements are attributed to the ionospheric pierce

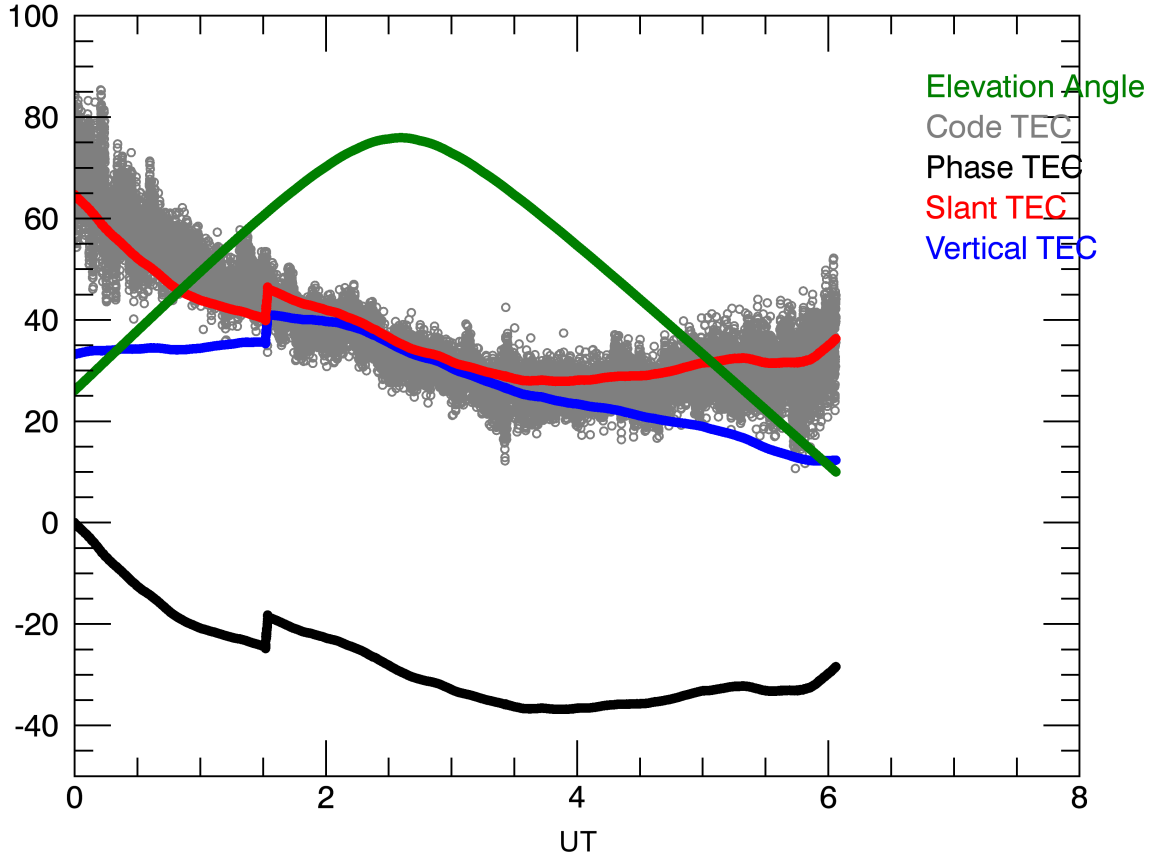

Figure 2.2: TEC measurements from PRN 2 on 15-Jul-2012. The code TEC is shown in grey while the carrier phase TEC is shown by the black curve. The red line is the leveled carrier phase Slant Total Electron Content which is then mapped to vertical at the IPP based on the elevation angle from ANNA shown in green. The blue line is the leveled and elevation adjusted VTEC. The sudden step around 01:30 UT is a slip of the receiver's phase cycle tracking loop, a phenomenon explained in detail in Section 4.2.

points (IPP), the point of intersection between a line connecting the GPS satellite and the observer, and the approximate altitude of the ionosphere's F-peak, typically ∼300 km. The IPPs are readily computed from the GPS ephemerides available through the International GNSS Service and the Jet Propulsion Laboratory in the form of .sp3 files. The pierce point locations can be seen in Figure 3.3a as short line-segments, representing their five-minute tracks within the background TEC map update period. Their locations, in the context of the background TEC map, reveal important contextual clues about the background density structure where the measurements are made.

While the Madrigal TEC maps provide the background density structure spatial scales on the order of 100-1000 km and the the Ann Arbor STEC measurements provides a measure of the density structure on much smaller spatial and temporal scales. IPP tracks are calculated from the precise GPS satellite ephemeris, provided by the International GNSS Service (IGS) and the NASA Jet Propulsion Laboratory (JPL) in Standard Product-3 (.SP3) format, and are superimposed onto the TEC maps to illustrate where the small-scale STEC measurements were taken relative to the large-scale background density structure.

2.1.6 Small-Scale Irregularity Detection

Background Density Removal In order to isolate small variations in STEC, a high-pass filter is used to remove the background large-scale density features. The STEC data are filtered using a tenth-order Butterworth highpass filter with stop and pass frequencies at 30 and 100 mHz respectively. The filter's frequency and forward phase response are shown in the top panel of Figure 2.3 and it is designed to both suppress the low-frequency background structure in STEC while maintaining the power from higher frequency fluctuations. Careful attention was paid to design the filter to minimize phase shifts in addition to the filter function

being convolved with the data both forward and backward to further cancel phase changes to the filtered signal. The unfiltered and filtered STEC are shown in the bottom panel of Figure 2.3.

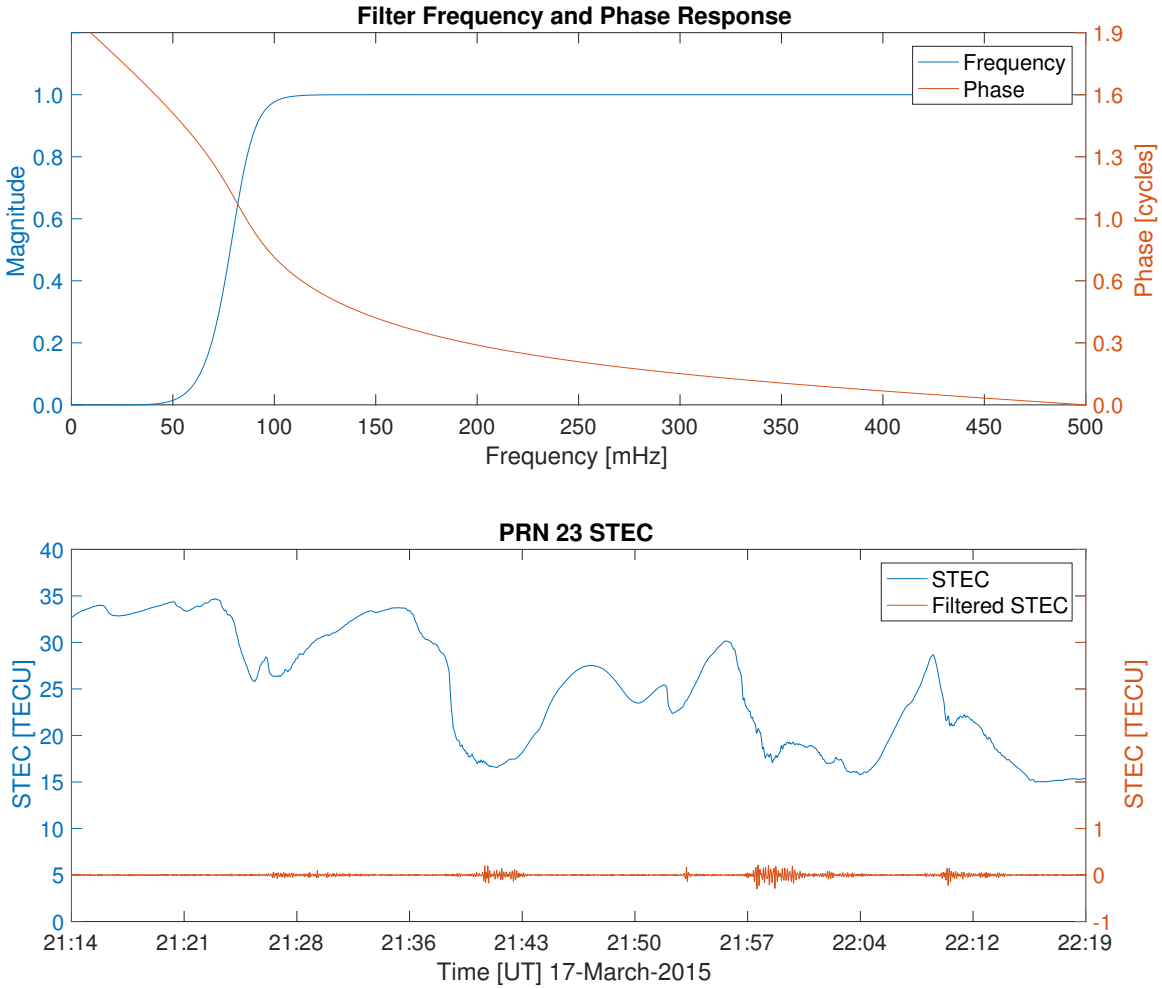

Figure 2.3: *Top:* Frequency and phase response of high pass filter used to remove low frequency (<100 mHz, long temporal) background from the STEC signal. *Bottom:* The unfiltered STEC signal from PRN 23 is shown in blue while the filtered signal is shown in orange. The filter removed the large-scale STEC variations associated with the SED plume in order to extract smaller-scale variations of interest to this study.

Fast Fourier Transform for Small-Scale Irregularity Detection The Discrete (Fast) Fourier Transform (FFT) of the filtered STEC for each PRN was computed in a sliding five-minute window advanced in ten seconds increments. The

sliding five-minute window (300 samples, 290 overlap) was chosen as a balance between three factors: first, to achieve a sufficient number of samples to resolve spectra with a resolution of at least 0.1 Hz; second, to maintain a sufficiently short IPP track (∼15 km) so that the resulting spectra can be attributed to a specific location within the SED plume system (e.g. a gradient crossing) and third, to take advantage of the maximum temporal resolution available from the TEC maps which are updated every five minutes. Additionally, to ensure a consistent number of samples between PRN in each FFT interval, measurements of PRN that were visible less than 90% of the five-minute Fast Fourier Transform (FFT) interval were excluded from analysis.

2.1.7 Irregularity Length Scale Estimation

The combination of the FFT spectra with the SuperDARN velocities allows for the estimation of irregularity length-scales. If it is assumed that the density irregularities are carried with the larger scale density structure from which they were formed, and are therefore "frozen-in" to the background flow (as has been suggested by *Yeh and Liu* [e.g., 1982]), then the temporal and frequency observations can be translated to spatial measurements provided the ion convection velocity is known and the IPP velocity $v_{ipp} \ll v_{ion}$, (v_{ipp} ∼50 m s^{-1}). With this in mind, the FFT power at various frequencies can reasonably be attributed to irregularities of certain length scales transported past the IPP at the ion velocity. Consider the simplified scenario: discrete and uniformly-spaced boxcar irregularities passing a nearly stationary IPP produce a periodicity in the slant TEC data that is revealed in the FFT frequency domain. Therefore, if the irregularity velocity is known (which is assumed to be with the background ion velocity per *Yeh and Liu* [1982]), then the irregularity length-scale can be estimated by $L_{irr} \approx v_{ion}/f_{FFT}$. The velocity of the IPP is nearly inconsequential and contributes only a small shift in

the frequency spectra within the 0 - 0.5 Hz Nyquist window.

To best illustrate the evolving variability in TEC near the SED plume, the FFT, VTEC time series, and Madrigal TEC maps are combined into a synchronized animation that shows the variability on length scales between a few kilometer (FFT spectra) and a few tens of kilometers (VTEC time series), alongside a map of the background large-scale SED density structure showing where each measurement is made (the IPPs) as shown in Figure 2.4. Each of the animation's three panes are synchronized with the five-minute TEC map update and IPP track. Since the IPP move at about 50 m s^{-1}, a five-minute window covers $\sim$15 km and the IPP tracks appear as short line segments overlaid in the mapping pane. The VTEC time series and FFT are updated more frequently — corresponding to the ten-second sliding FFT window. A windowing frame superimposed on the VTEC time series illustrates the period of the FFT interval. Meanwhile, the Madrigal TEC map is updated when the leading edge of the FFT window is at the mid-point between five-minute map update intervals. This ensures that the displayed map best represents the background against which the FFT was computed.

In addition to GPS TEC observations, observations from the Defense Meteorological Satellite Program (DMSP) and the Active Magnetosphere and Planetary Electrodynamics Response Experiment (AMPERE) are used to locate regions of auroral precipitation. DMSP measures precipitating electron and ion fluxes while AMPERE estimates the hemispherical polar radial field-aligned current density derived from reduced magnetic field perturbation data from the Iridium satellite constellation. The DMSP and AMPERE observations are used here to estimate the location of the auroral oval's equatorward boundary in order to delineate between the density irregularities and enhancements caused by aurora and those associated with the SED plume.

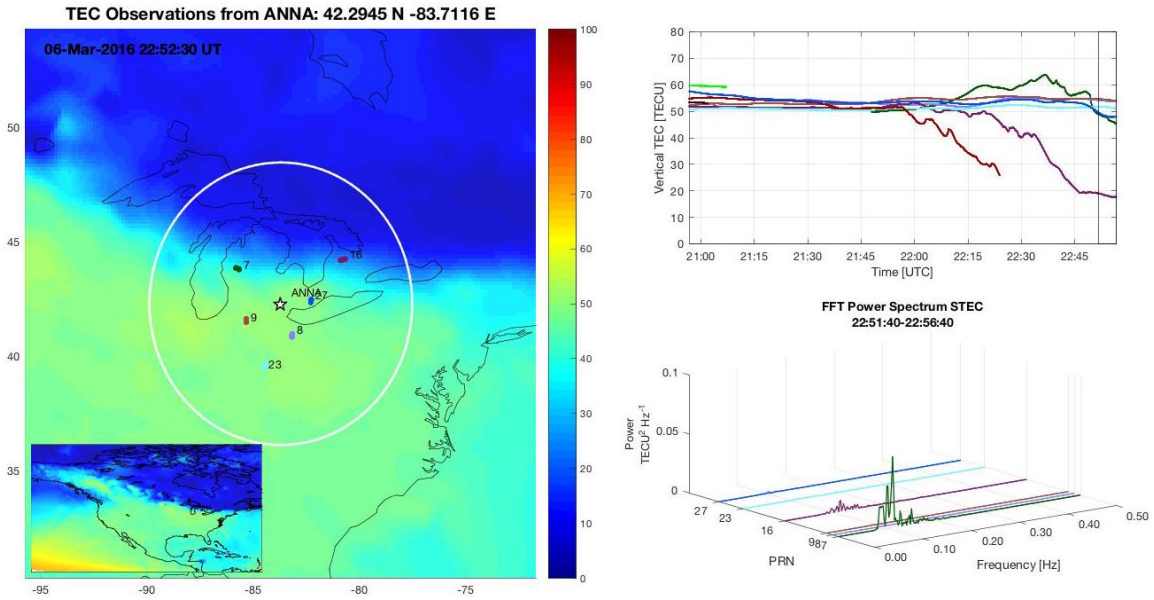

Figure 2.4: Example frame from animation combining Madrigal TEC maps (left), IPP tracks, VTEC time series (top right) with five-minute FFT window framed on the right edge of the time series, and STEC FFT for each GPS PRN during the five-minute windowed interval (bottom right).

2.2 Technique Validation

Since the actual TEC structure of the ionosphere being observed both unknown, it is uncertain how the IPP derived time series will appear in the frequency domain. In all likelihood, the irregularities of a given length scales are not evenly spaced, and their motion past the IPPs is most certainly not represented by a pure sinusoid. Consequently, they spread power across multiple frequencies. Further, there are multiple, and likely a continuum of, irregularity length scales present in the spectrum. In addition, the detected frequency spectra are influenced by a Doppler shift due to the relative motion of the IPPs during the five-minute sampling window on which the FFT is applied and the shift effects the detected frequency of irregularity length scale differently according to $\Delta f = \Delta V / l$.

2.2.1 Synthetic TEC Structure

To address these uncertainties, a synthetic TEC density structure with known irregularity length scales was created. The motion of IPPs through this structure were then simulated for different sampling rates and convection speeds. The TEC structure was generated from the superposition of random, uniformly distributed, two-dimensional Gaussians given by Equation 2.1

$$f(x,y) = A\, e^{-\left(\frac{(x-x_0)^2}{2\sigma_x^2}+\frac{(y-y_0)^2}{2\sigma_y^2}\right)} \tag{2.1}$$

The TEC amplitude of the structures (or irregularities) is modeled by parameter A and the length scale is modeled by both σ_x and σ_y, which are set equal here. The number and length scale of density irregularities are assumed to be related by an inverse power law, i.e., the larger the length scale, the fewer irregularities on that scale. The power law was generated by fitting the basic power law equation of $P = b\,x^{-m}$, where P is the number of density irregularities and x is the chosen length scale in kilometers, to representative points estimated from observations. Specifically, it was estimated that there would be one 100 km scale density structure and as many as 10^4 density irregularities on the 1 km in a 100×100 kilometer grid. A similar power law estimation of amplitudes was used and fit to amplitude and quantity with input points of 0.1 and 60 TECU corresponding to the 1 km and 100 km scale irregularities respectively. The "seed locations" for each irregularity were assigned using a uniform distribution random number generator. The resulting structure was produced through the addition of simulated of density irregularities at each grid point. This gave the flexibility to produce a wide range of length scales ranging from a single characteristic length, to a superposition of many length scales and amplitudes. Figures 2.5 and 2.6 are two examples of synthetic TEC structures. Once the synthetic structures were generated, data samples were extracted along an

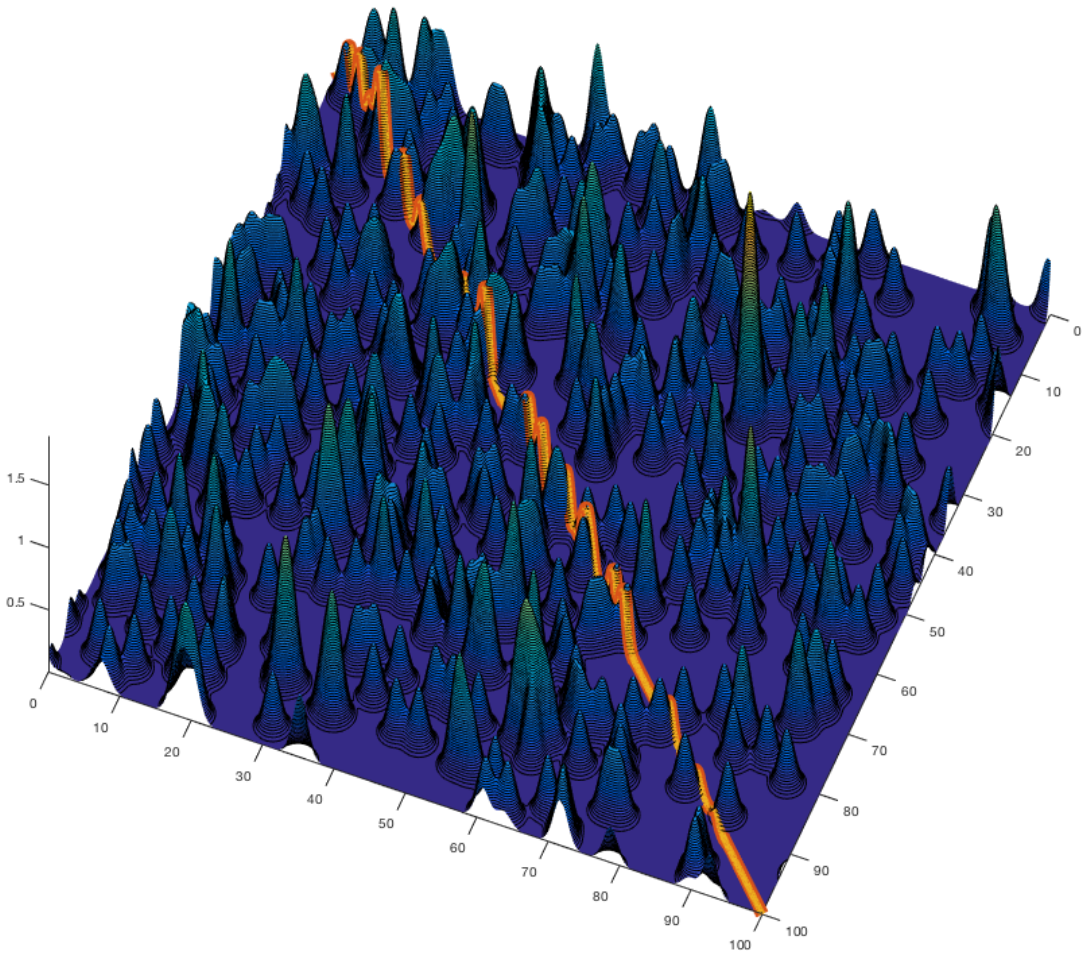

Figure 2.5: Synthetic TEC structure with a single length scale (10 km) density structure.

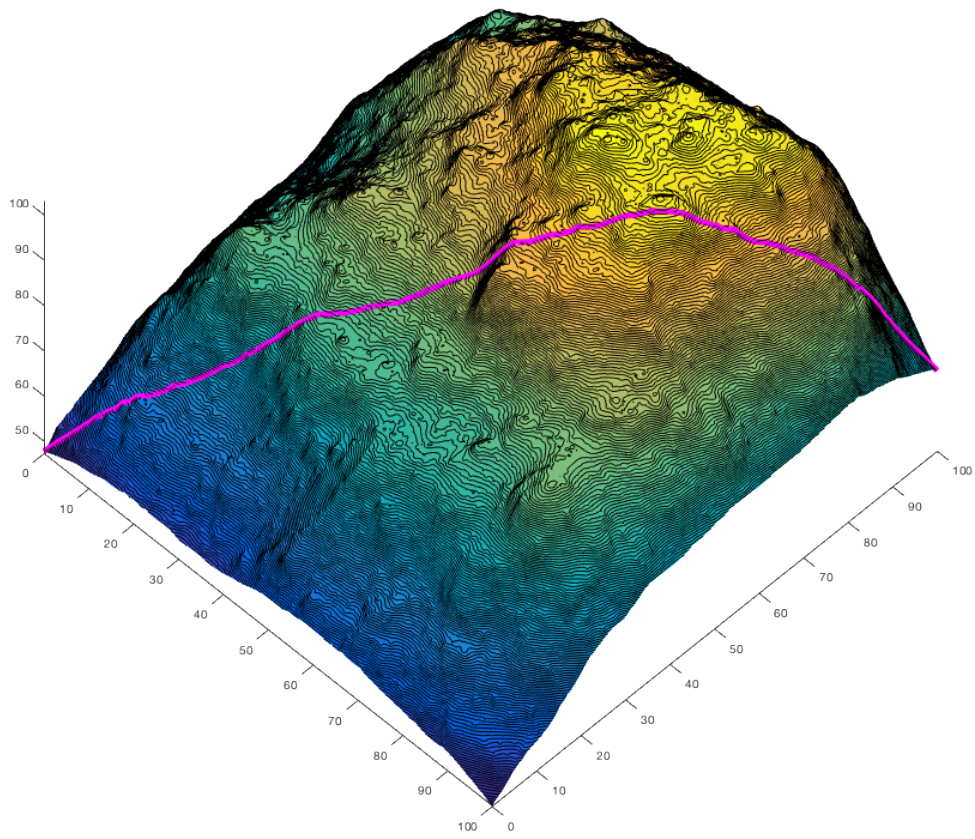

Figure 2.6: Multi-scale synthetic TEC structure with length scales logarithmically spaced from 0.1 km to 200 km.

arbitrary one-dimensional path through the density structure — in this case it is the matrix diagonal. This mimicked a IPP track that would be observed from a real ground-based receiver. IPP tracks are similar to satellite ground tracks, except that they are set at 300 km altitude and are defined as the intersection of a 300 km spherical shell with the line connecting an individual GPS satellite to a receiver. The altitude of 300 km is selected because it represents the typical height of the ionosphere's F_2 peak — the densest region of the ionosphere and the altitude where most irregularities are assumed to occur. For this purpose, each GPS satellite has a unique IPP track and TEC measurements are assigned to the location of the IPPs. This assignment is reasonable even for a line integral density because the F_2 peak contains the majority of the electron density. Figure 2.7 shows a simulated IPP track time series alongside a real IPP track time series (Figure 2.8) taken on 17 March 2015. Both time series are approximately 30 min long. Since the IPP velocity is around 50 m s^{-1}, it would cover the simulated 100 km track in 33 minutes. The magnitude of the simulated data is much larger than the real data which is a result of the summation of the large length scale irregularities. Since the interest here is on the small scale, high frequency data, the absolute amplitude becomes irrelevant after high pass filtering. The synthetic time series was filtered using the same highpass Butterworth filter used in the analysis of real TEC data and the original and filtered signal are shown in Figure 2.10 along with the filter's impulse response.

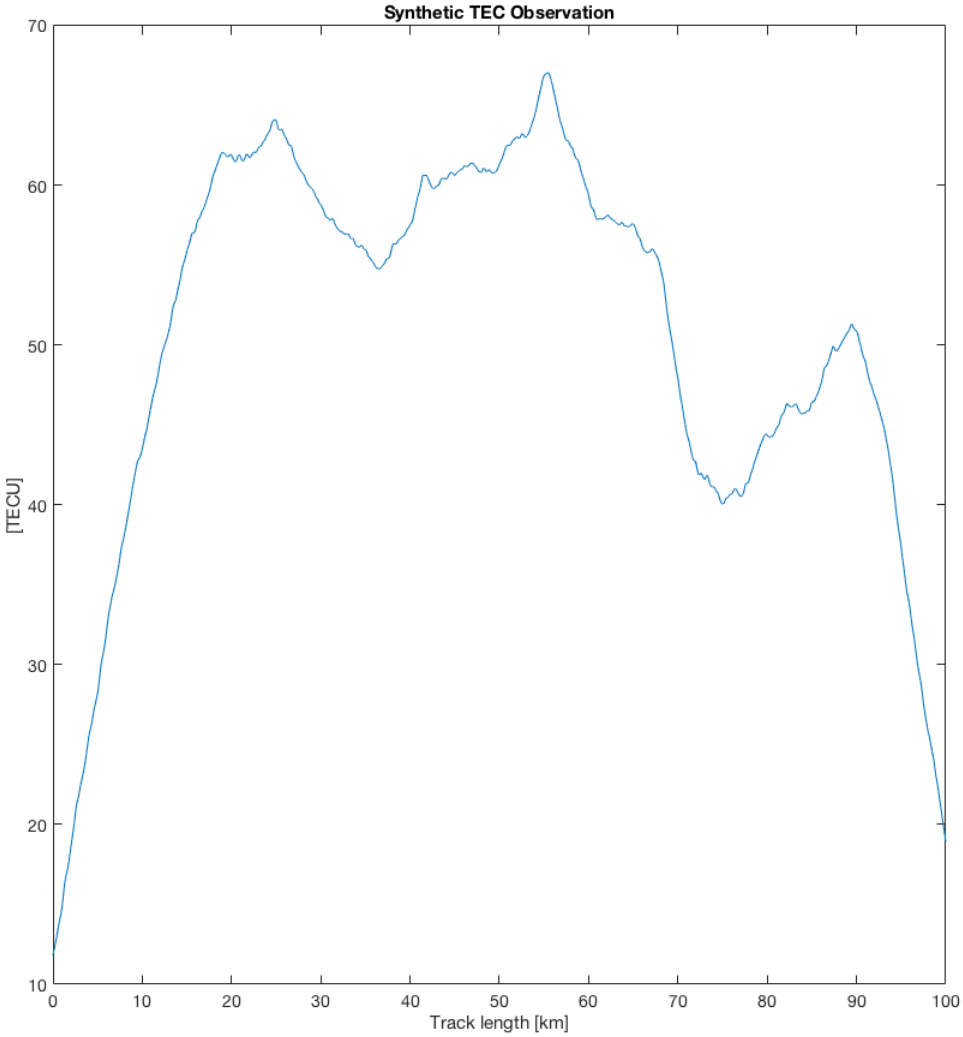

Figure 2.7: Multiple-scale synthetic TEC time series for ∼33 min.

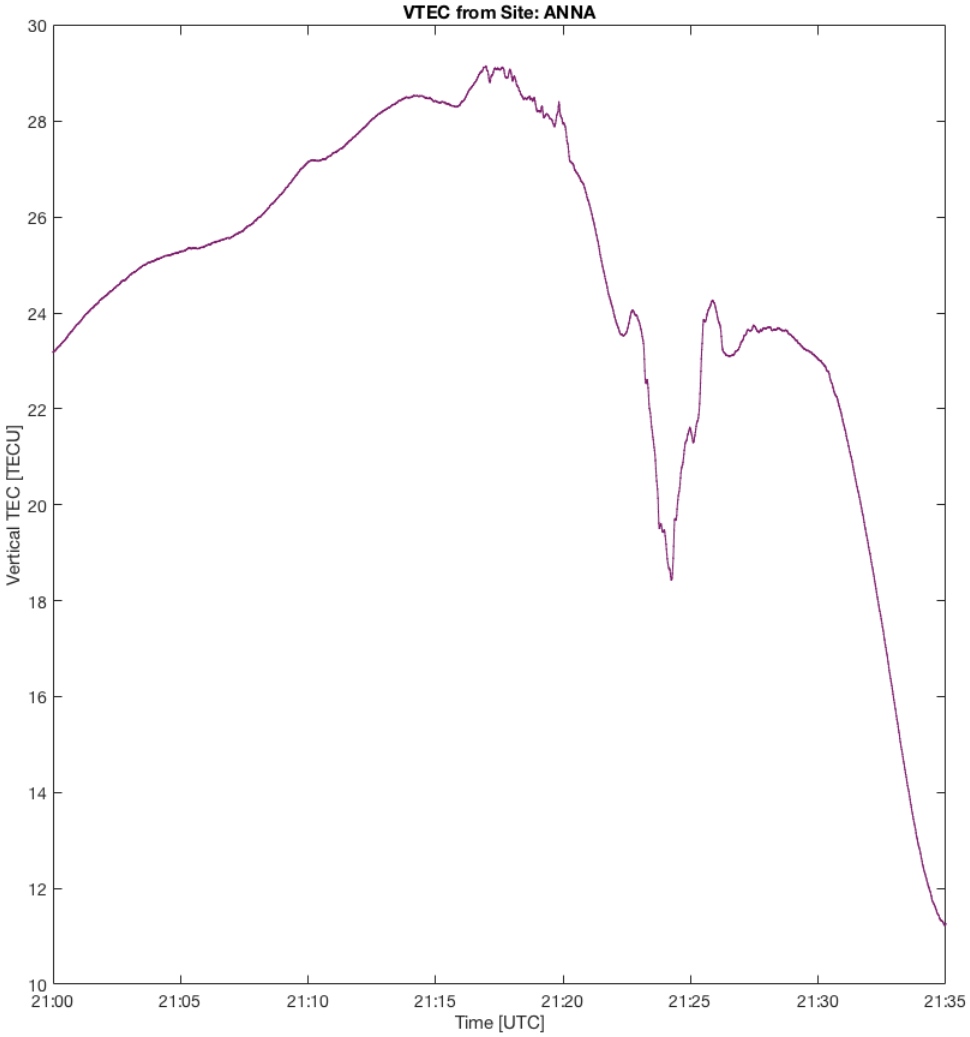

Figure 2.8: GPS PRN 16 TEC observed from
Ann Arbor, MI 17 March 2015

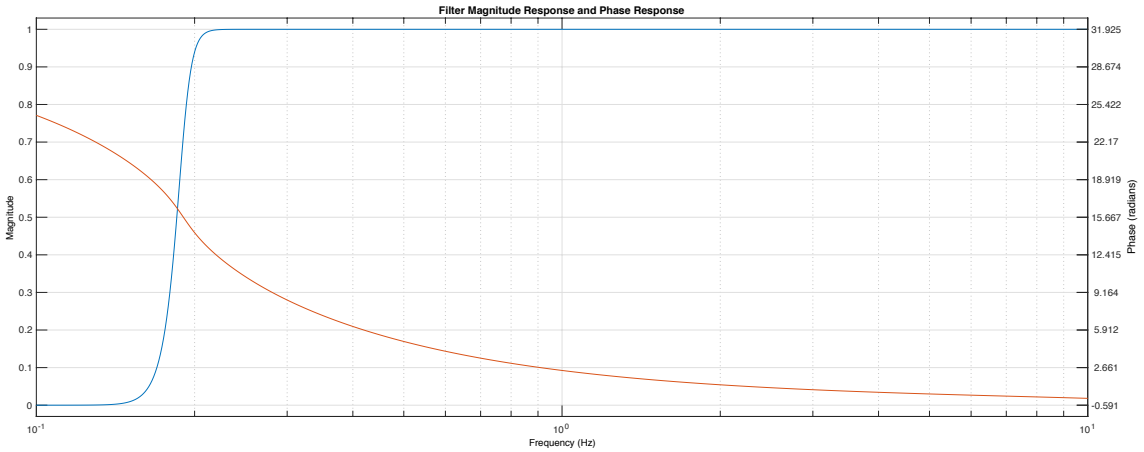

Figure 2.9: Filter magnitude and phase response for 10 Hz sample rate used in validation.

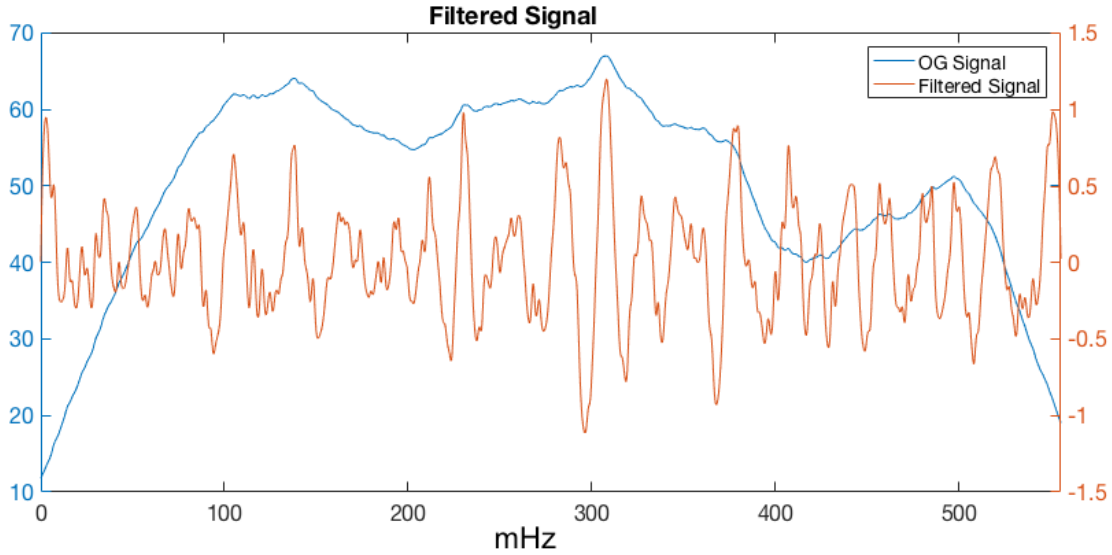

Figure 2.10: *Top:* Original and highpass filtered signal. *Bottom:* The filter impulse response.

2.2.2 Simulating Structure Convection

Convection of the simulated TEC structure was achieved by decimating the one-dimensional time series by increments of simulated velocity divided by the grid resolution. For example, if 1000 m s^{-1} convection is to be simulated, and the structure is built on a grid with 100 m per step, then the time series should be decimated by a factor of 10 (# steps/second). To simulate sampling of the convecting structure, the time series is decimated again at the sampling frequency. The resulting time series is a simulated observation of a convecting density structure. Since the real world sampling frequency knows nothing of the convection speed, an accurate spectral analysis of the simulated data should use the sampling frequency as the reference at not the combined decimation rate.

2.2.3 Pierce-Point Doppler

The motions of IPPs relative to the ion convection patterns are grouped into parallel and antiparallel categories based on the dot product of their unit vector with ion velocity, which was approximated as due west during the observation period. This assumption is supported by SuperDARN radar observations fitted to polar convection models. Since the IPPs travel at approximately 50 m s^{-1} , the maximum expected Doppler shift is due to a net difference of 100 m s^{-1} between purely westward (parallel) and purely eastward (antiparallel) IPP tracks. The expected Doppler shift varies with velocity and irregularity length scale according to $\Delta f = \Delta V/l$.

2.2.4 Results

2.2.4.1 Bounding of Small Scale Irregularities

In runs with density structures consisting of a single irregularity length scale, the filtered spectra showed power spread through all frequencies below the predicted convection frequency, $f = V_{ion}/l$ and none at higher frequencies. For example, spectral power begins around 5 Hz for a 200 m density structure convecting at 1000 m s^{-1} m/s and fills in lower frequencies — presumably because of the random overlap of irregularities producing power at lower frequencies — but does not spread to higher frequencies. This is significant because it presents a potential tool to bound the range of the smallest length scales in a real observation and moreover, runs with multiple length scales appear to show some discernible spectral power at lower frequencies that correspond to other known length scales. Figure 2.11 shows the beginning of spectral power at frequencies lower than 5 Hz and another potential peak around 1 Hz — corresponding to the 1 km contained within the structure.

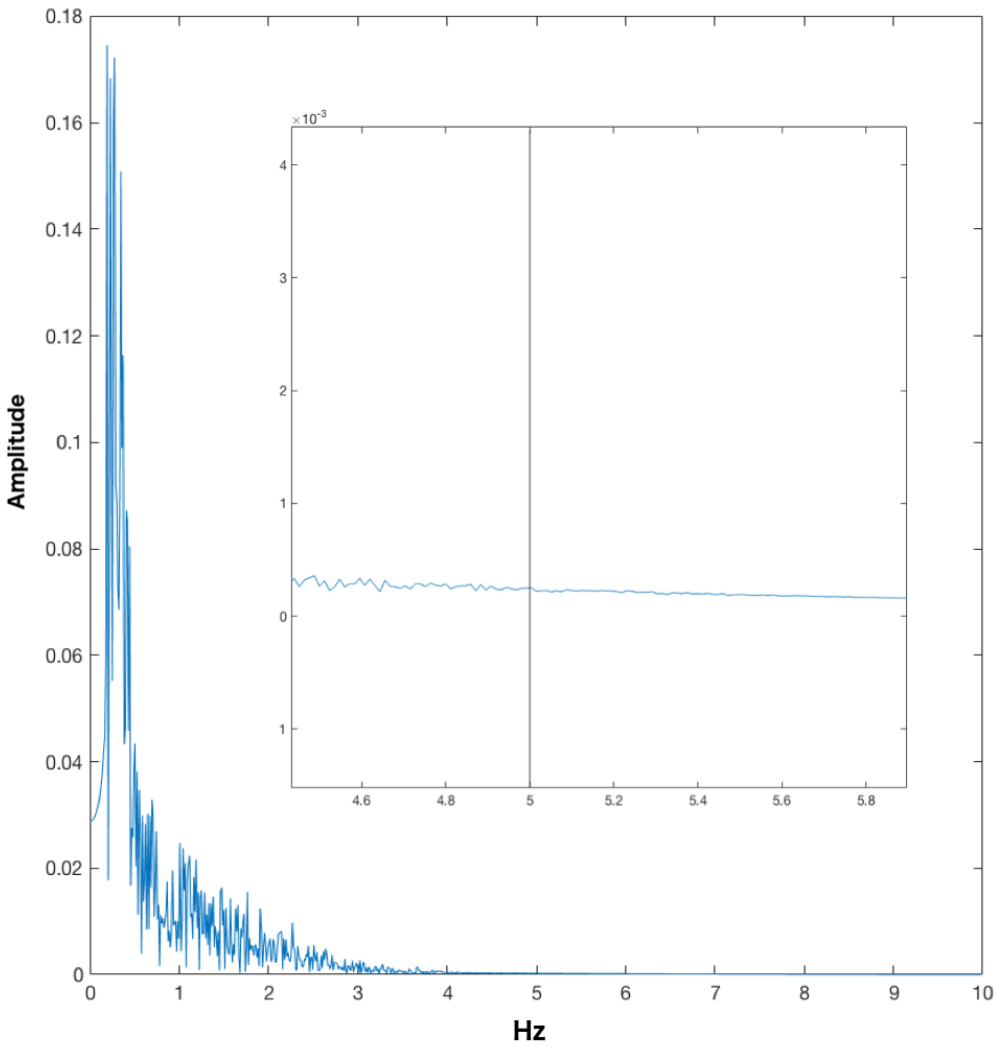

Figure 2.11: Spectrum for multi-scale synthetic TEC structure that contains simulated irregularities of characteristic length scales of 200 m and 1000 m. The spectral power begins at the frequency corresponding to 200 m irregularities convecting at 1000 m s^{-1} (5 Hz) with a secondary peak visible at 1 Hz —- corresponding to the 1000 m irregularities. *Inset:* Zoomed view near 5 Hz where spectral power is first apparent.

2.2.4.2 Simulated IPP Doppler

Figure 2.12 shows the spectra for the same density structure convecting at 1400, 1000, and 900 m s^{-1}. 1000 m s^{-1} is taken as the nominal ion velocity. It is apparent that for a higher velocities, the spectrum is shifted toward higher frequencies, and similarly, for lower velocities it is shifted lower. The difference between 900 and 1000 m s^{-1} is representative of real velocity differences between eastward and westward tracking IPPs — suggesting the observing Doppler shift in should be discernible in the real data sets which would support the validity of FFT spectra as a means for describing the ionosphere's small-scale density structure. The 1400 m s^{-1} velocity was used to illustrate the consistency in the magnitude of the Doppler shift at higher frequencies. Figure 2.13 superimposes the spectra of pure sinusoids at the characteristic length scale frequency. Notably, the spectral power increase is consistent with the Doppler shift of the characteristic length scale frequencies suggesting that if the ion velocity is well known (through radar or other measurements) there is a good chance of using FFT spectra to bound the characteristic length scales present in real observations.

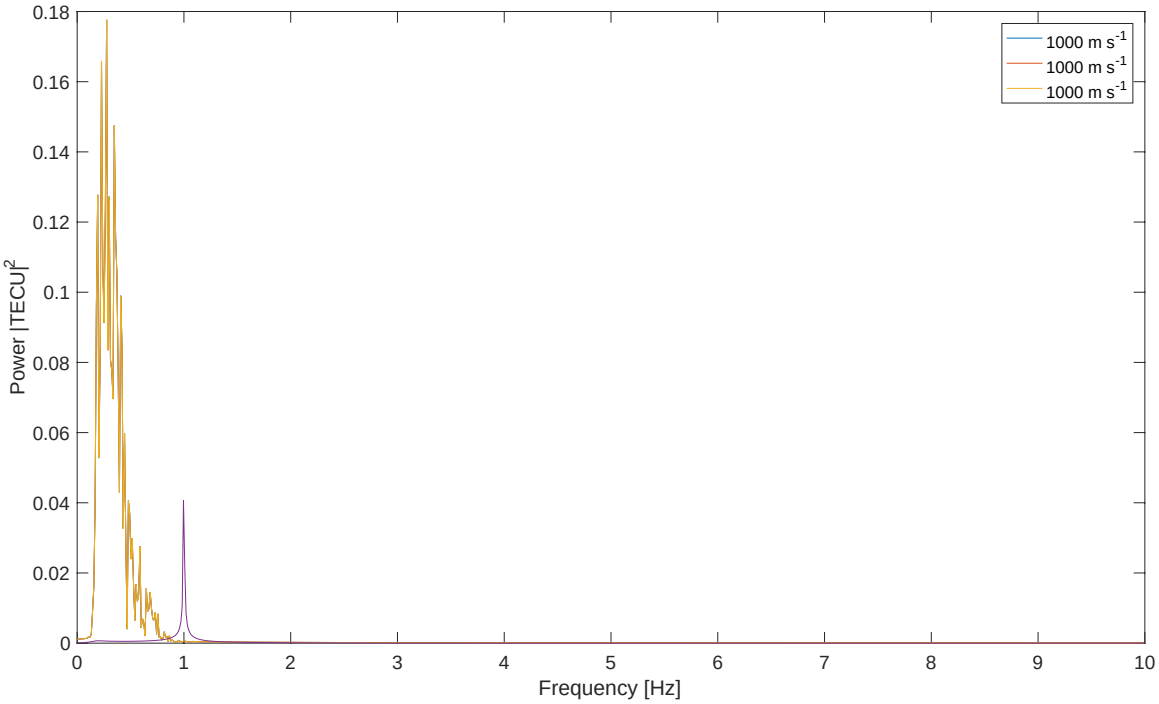

Figure 2.12: Single length scale (10 km) density structure.

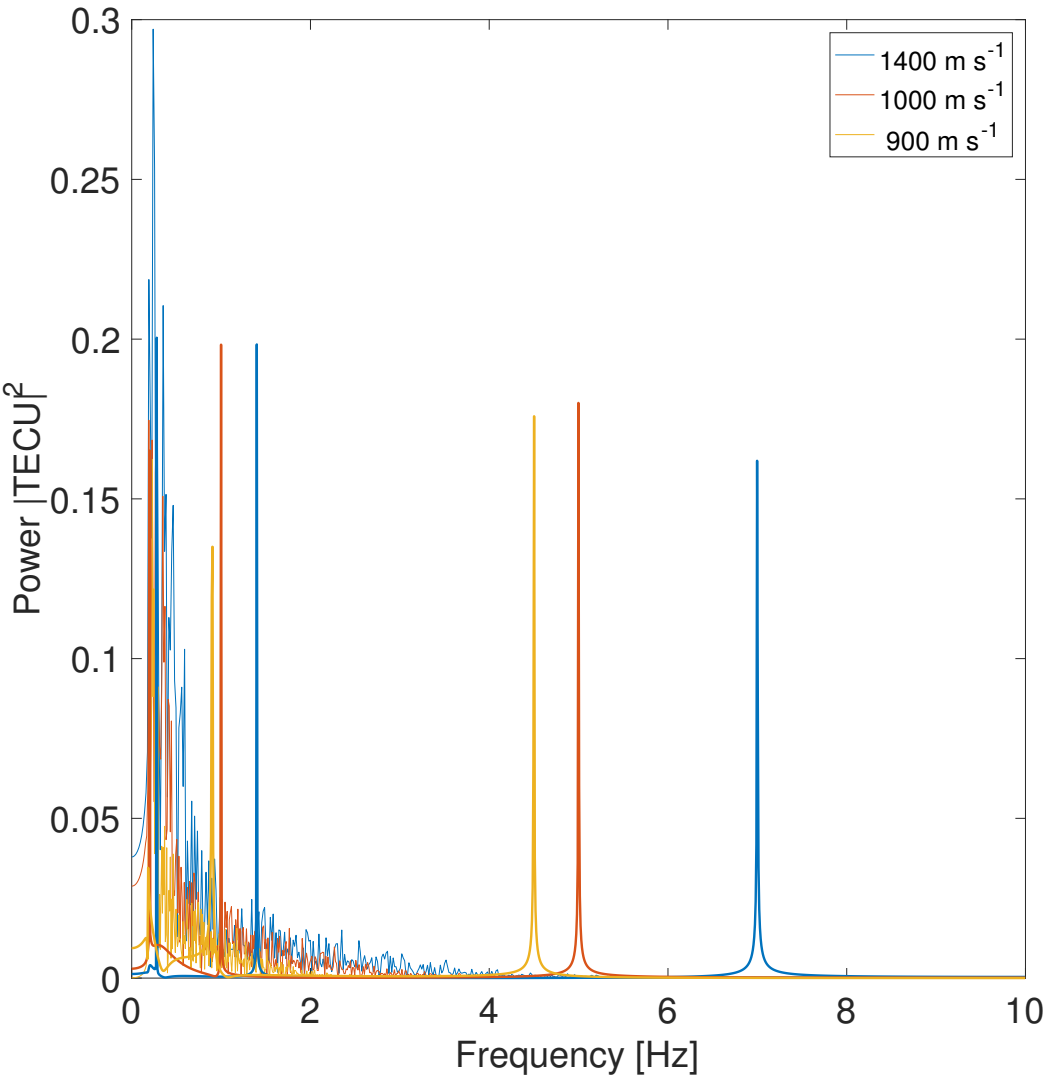

Figure 2.13: Multi-scale density structure.

2.3 Conclusion

This describes the methodology used in Chapters III and IV and validates the FFT and Radar method for detecting small-scale density irregularities from single station TEC data. Furthermore, the bounding of small-scale irregularities in the simulated data demonstrates that, not only can the presence of small-scale irregularities be detected, but it strongly supports the possibility of identification and characterization of small-scale irregularities through proper filtering and analysis and has demonstrated that the FFT spectrum provides a clear lower limit on the smallest length scales detected at a given sample rate. More work is needed comparing real-world data at higher sample rates to the simulated data sets and simulated density structures, rather than TEC structures, will provide even better characterization of the capabilities of this methodology.

CHAPTER III

Small-Scale Structure of the Mid-Latitude Storm Enhanced Density Plume of March 17, 2015

On 17 March 2015, the Earth experienced a G4 “severe" geomagnetic storm on the National Oceanic and Atmospheric Administration (NOAA) geomagnetic storm scale [*Love and Rigler*, 2015]. At 04:45 UTC, the Kyoto Dst indicated a 55 nT enhancement of the horizontal geomagnetic field which is characteristic of a sudden storm commencement. The storm reached the peak of its main phase around 19:00 UTC with minimum magnetic field disturbances: Kyoto Provisional Dst = -223 nT and Sym H = -234 nT. Over the period between 16 March 2015 and 19 March 2015, the NOAA Planetary K-index (K_p) was greater than 5 for 48 of 72 hours and $K_p = 8$ for a total of 9 hours during the main phase of the storm. Meanwhile, throughout 17 and 18 March, the NOAA $K_p \geq 7$ on four of twenty-four 3-hour periods and above 5 during sixteen periods. A SED plume was observed in the Madrigal TEC data during the North American afternoon/dusk period on 17 March (shown in Figure 3.1). The SED plume began in a region of enhanced TEC (the SED base) that was poleward and distinct from the TEC peaks of the enhanced equatorial anomaly. The plume extended to the northwest across the Great Lakes region and toward the noontime cusp. A low-density, mid-latitude trough is also visible in Figure 3.1, while the auroral oval extended as far south as 39° geographic

latitude at 23:17 UT (inferred from Figure 3.5 and discussed in section 3.5). The Dst minimum was reached at approximately 23:00 UT and this chapter includes observations from a single GPS station in Ann Arbor, Michigan: ANNA (42.29 N, -83.71 E Geodetic; 53.31 N, -10.34 E CGM) directly in the path of the SED plume, during the end of the main phase and the beginning of the recovery phase between 20:00 UT 17 March 2015 and 03:00 UT 18 March 2015. Other stations within this region (250 km radius) have 1 Hz data available during this event. Those within that radius have lower sampling rates (30 s) which are too low for the time and length scales of interest to this study. Two Canadian stations, ALGO (45.96° N -78.07° E GEO, 56.74° N -2.57° E CGM) and NRC1 (45.454° N -75.62° E GEO, 56.04° N 0.97° E CGM), do have 1 Hz data for this time, but are too high in latitude and too far ahead in local time to distinguish between auroral precipitation and plume generated irregularities and are therefore not used. Within 1000 km, there are six stations in the UNAVCO database with 1 Hz data rates. Stations in Ames, IA (AMES: 41.98° N -93.68° E GEO, 52.58° N -25.37° E CGM) and near St. Clairsville, PA (P817: 40.14 N -78.51 E GEO, 52.59° N -3.51 E CGM) were analyzed using the the same methods described in Chapter II and produce similar results to the data observed at ANNA in terms of general trend, but being 900 km west and 700 km east of ANNA respectively, exhibit the expected localized differences in density structure >10 km. This suggests that for the purpose of this study, ANNA is representative of the available 1 Hz GPS TEC data for this event.

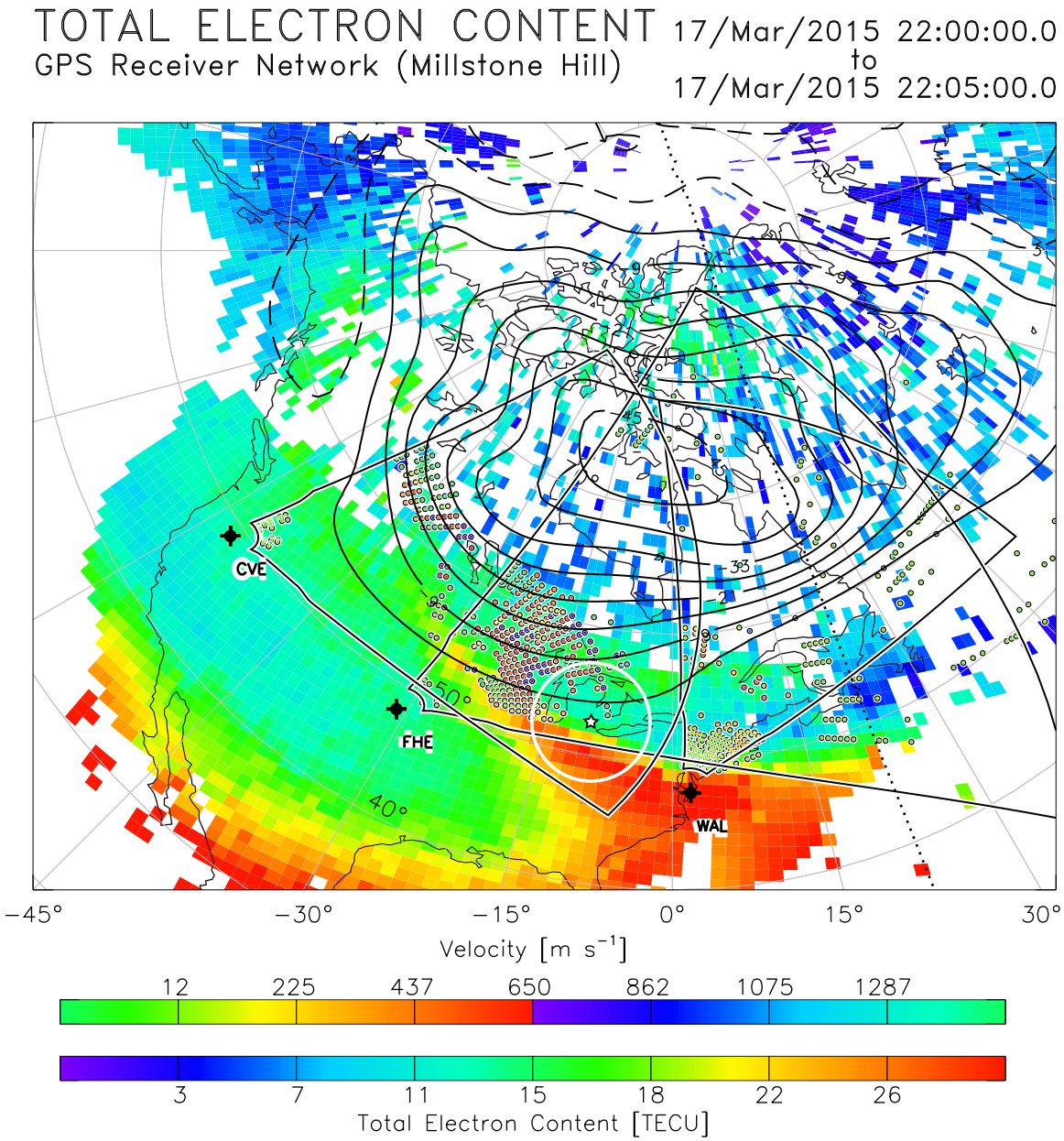

Figure 3.1: The SED plume is visible in the 1° x 1° TEC map as a red band stretching toward the northwest at 22:00 UT. The colored circles indicate the location of SuperDARN Radar backscatter and line-of-site ion speeds from Christmas Valley East, Fort Hays East and Wallops Island while the polar equipotential lines (solid lines) show the direction of plasma convection (westward within the Great Lakes region). The day/night terminator is shown as a dotted line. *Figure courtesy of Evan Thomas, Virginia Technological University.*

An animation, available here, encompasses the period from 20:00 UT 17 March 2015 to 03:00 UT 18 March 2015 and combines the VTEC time series, sliding FFT, and TEC maps into three panes. Each of the animation's three panes are synchronized with the five-minute TEC map update and IPP track. Since the IPP move at about 50 m s^{-1}, a five-minute window covers ∼15 km and the IPP tracks appear as short line segments overlaid in the mapping pane. The VTEC time series and FFT are updated more frequently — corresponding to the ten-second sliding FFT window. A gray vertical bar superimposed on the VTEC time series illustrates the period of the FFT interval. Meanwhile, the Madrigal TEC map is updated when the leading edge of the FFT window is at the mid-point between five-minute map update intervals. This ensures that the displayed map best represents the background against which the FFT was computed.

The SED plume is clearly visible from VTEC data in the observation area beginning around 20:00 UT. Figures 3.2-3.5 show results from key intervals, 20:45, 21:30, 22:00, 23:00, and 23:20 UT, during the SED plume's passage over the Ann Arbor observation area. Each of these figures contains: *Left:* the track of IPPs in relation to the SED plume, *Right Top:* the VTEC time series, and *Right Bottom:* the 5-minute STEC FFT. Observations for the entire period of 20:00 UT 17 March 2015 to 00:00 UT 18 March 2015 are contained in the supplemental animation.

3.1 20:00 to 20:45 UT, Entering the SED Plume

During the period from 20:00 to 20:45 UT, the SED plume's equatorward edge and density peak passed over Ann Arbor (Figure 3.2). Overall, VTEC measurements from PRN IPPs that tracked equatorward of the SED plume were comparable to quiet time levels, and those that tracked near or inside the plume showed VTEC that was elevated above quiet time levels with minimal increased variability seen in the VTEC time series. For example, PRN 3, shown in bright green in Figure 3.2,

has an IPP that remained ahead of the plume's advancing equatorward edge and showed smooth and relatively constant acVTEC values with littleacFFT power above 100 mHz. By contrast PRN 16 (purple), which tracked poleward into the plume, showed smooth, but increasing VTEC. Around 20:37, as it traveled $> 1°$ equatorward of the plume's equatorward edge, PRN 3 exhibited an increase in acFFT power just above 100 mHz, though there were no variations observed at other frequencies or in the VTEC times series.

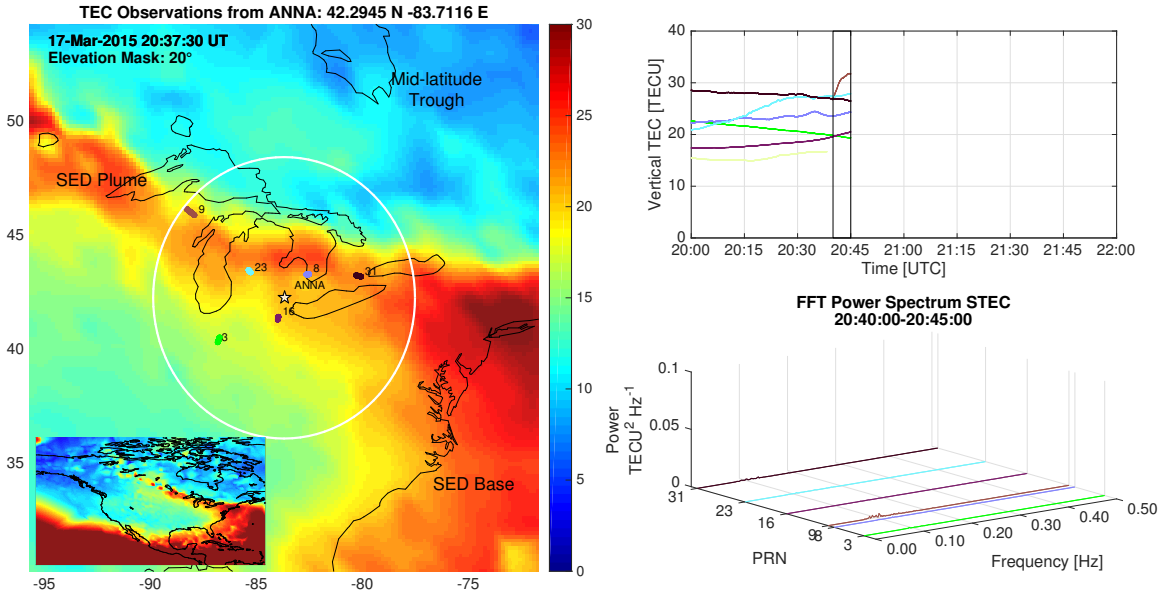

Figure 3.2: *Left:* Interpolated Madrigal VTEC map with 5-minute IPP tracks for the interval ending at 20:45 UT. The location of the ANNA receiver is marked with a five-pointed star and a white circle demarcates the field-of-view boundary with a 20° elevation mask. The SED plume, SED base region, and mid-latitude trough are visible. *Inset:* TEC over North America. *Right Top:* The cumulative VTEC time series from 20:00. The five-minute FFT window is indicated by the two black vertical lines at the end of the time series. *Right Bottom:* The 5-minute FFT for the observable GPS PRN.

PRN 23 (light blue) and PRN 31 (black) were first observed inside the plume and near its equatorward edge (not shown). PRN 23 was located in the narrower, westward portion of the plume at -86° E, while PRN 31 was located to the east (near -81° E) and closer to the SED base region. Both exhibited elevated VTEC, although PRN 23 was initially ∼7 TEC Unit, TECU = 10^{16} [e^- m^{-2}] (TECU) lower

than PRN 31. Between 20:00 and 20:45, the plume moved so that both PRN 23 and 31 were tracking across the plume. PRN 23 VTEC increased steadily, though with persistent small-scale variations and a slight increase in FFT power (low amplitude) near and slightly above 100 mHz at 20:20 UT — corresponding to its crossing into a large-scale bite-out in VTEC along the SED plume's poleward edge. PRN 31 VTEC held at a consistent 26-27 TECU and exhibited small variations in the VTEC time series, but these did not significantly affect the FFT power spectra. PRN 31 also tracked between some of the plume's large-scale (1-2° lon.) high density structures visible in the VTEC map — suggesting a possible explanation for its near constant VTEC.

3.2 20:45 to 21:20 UT, Longitudinal Asymmetries and Inside the Plume

At 20:45, PRN 9 (brown), entered the observation area near -88° E as it crossed into the plume and tracked parallel its poleward edge. It registered an increase of 5 TECU accompanied by a slight increase in FFT power around 100 mHz upon entering the plume before it was again crossed by the plume's poleward edge, when it recorded a drop in VTEC of ∼15 TECU and exhibited rough, large-scale VTEC fluctuations through the decrease. PRN 31 was observed along a similar path along the plume's poleward edge, though further east — near -80° E. VTEC for PRN 31 was 5 TECU less than PRN 9, but registered a comparable decrease in VTEC after crossing the plume's edge. However, in contrast with PRN 19, the decrease exhibited smooth fluctuations over distances of ∼30 km, which were accompanied by a broadband increase in FFT power that continued until PRN 31 left the observation area at 21:25 UT. Meanwhile, PRN 16 and 23 both showed increased VTEC as they moved through the SED plume. PRN 23 initially continued its track

inside the plume along its length, from -87° to -85° E and near the poleward edge. It crossed the poleward edge around 21:00 and the arc of its IPP track continued a southward turn that followed behind the plume's advancing poleward edge. This afforded sustained observations of the plume's poleward boundary which exhibited large undulations in VTEC of ∼10 TECU over periods of approximately ten minutes. PRN 16 continued tracking northward through the plume and toward the the poleward edge near -80° E. Instead of small-scale variations observed in PRN 23 as it crossed the plume, PRN 16 exhibited only smooth increases in VTEC with large-scale variations of 1-3 TECU over ∼10 km were observed, similar to PRN 23, with no observable change in FFT power until 21:20 when it crossed the poleward edge.

3.3 21:30 to 22:50 UT, Entering the Mid-latitude Trough

Around 21:30, the plume's poleward edge passed over the observation area and PRN 9,16, 23, and 31 showed sudden increases in FFT power while near the plume's poleward edge — PRN 23 especially showed a large increase in FFT power between 100 mHz and 300 mHz during 21:50-22:00 UT (Figure 3.3).

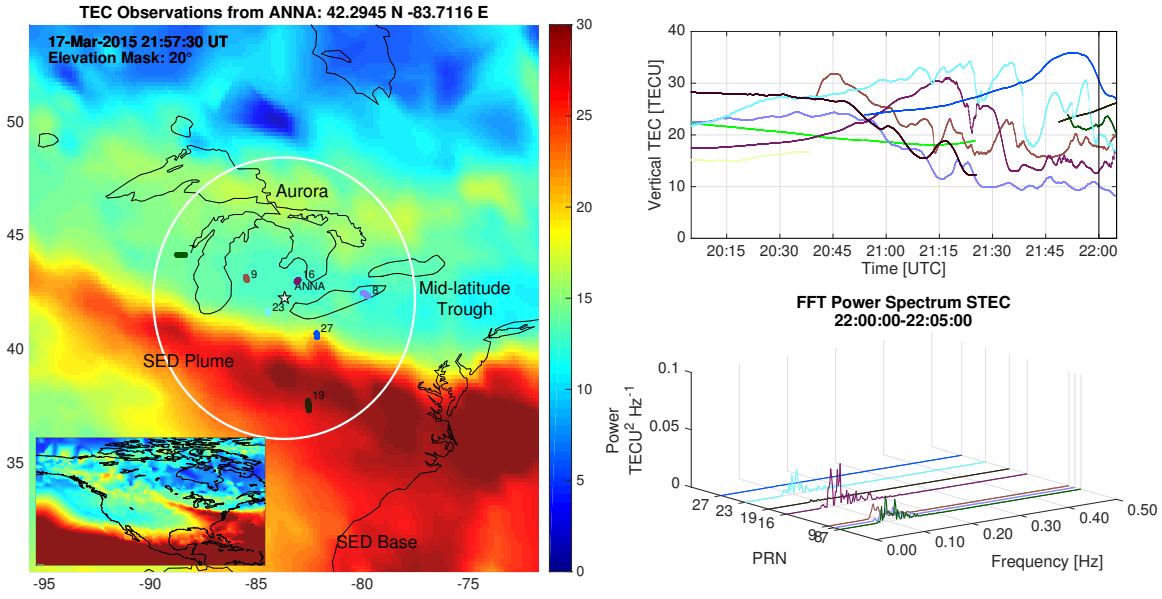

Figure 3.3: *Left:* Interpolated Madrigal VTEC map with 5-minute IPP tracks for the interval ending at 22:00 UT. The location of the ANNA receiver is marked with a five-pointed star and a white circle demarcates the field-of-view boundary with a 20° elevation mask. The SED base region, SED plume, mid-latitude trough, and auroral enhancement are visible from bottom to top. *Inset:* TEC over North America. *Right Top:* The cumulative VTEC time series from 20:00. The five-minute FFT window is indicated by the two black vertical lines at the end of the time series. *Right Bottom:* The 5-minute FFT for the observable GPS PRN.

During this interval, PRN 7 (dark green), 9 (brown), and 16 (purple) were inside the low-density trough and also exhibited increased FFT power, but much lower than was observed for PRN 23. PRN 19 and 27 were located entirely within the SED plume with FFT spectra that were largely unchanged.

At 22:40 UT PRN 7 and 9 were in the vicinity of a gradient between the trough and the trough minimum and, unlike the other PRN observed at this time, showed an increase in FFT power beginning at ∼80 mHz and extending as high as 300 mHz. PRN 16, 19, 23, and 27 were also within the trough — though either well inside the trough minimum or far away from its edge gradients and showed no increase in FFT power.

3.4 22:50 to 23:30, The Mid-latitude Trough

Figure 3.4 shows the interval between 22:50 and 23:00 UT. Most of the observable PRN were located within the trough and away from density gradients near the SED plume or low-density trough minimum. VTEC values leveled off between 10 and 15 TECU and there were only minor changes in FFT power — mostly associated with PRN 9 and 16, which were approaching the observed VTEC enhancement of the auroral oval. PRN 23 (light blue) was the closest to the SED plume and headed equatorward, though still lagging behind the SED plume's poleward edge. It recorded increasing VTEC as it tracked toward the plume and its poleward gradient, but no change in FFT power was observed.

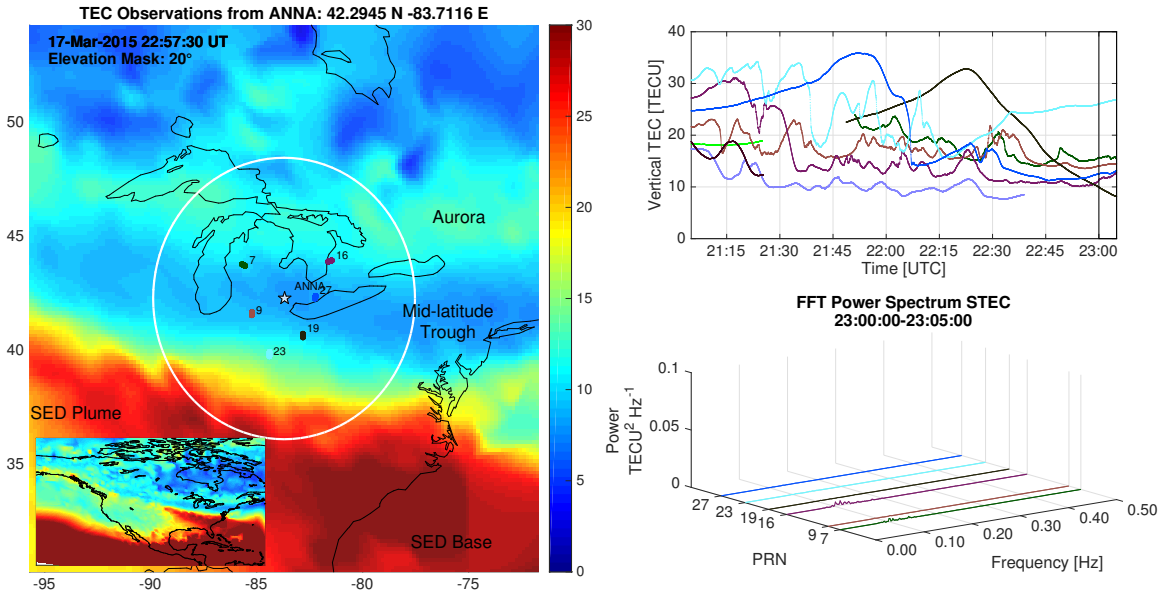

Figure 3.4: *Left:* Interpolated Madrigal VTEC map with 5-minute IPP tracks for the interval ending at 23:05 UT. The SED base region, SED plume, mid-latitude trough, and auroral enhancement are visible from bottom to top with all IPP tracks (with the exception of PRN 23) are located in the mid-latitude trough. *Inset:* TEC over North America. *Right Top:* The cumulative VTEC time series from 21:00. *Right Bottom:* The 5-minute FFT for the observable GPS PRN.

PRN 19 (black) traversed a similar portion of the plume during this time, but moving poleward, and showed a steady and smooth, but slightly steeper decrease in density away from the plume with no FFT power changes. PRN 9 (brown) and 27

(blue) were near the trough region and showed a difference of ∼2 TECU between the trough's poleward gradient (PRN 9) and its base (PRN 27) and their FFT spectra do not show any obvious small-scale variations. Meanwhile, PRN 7 (dark green) and 16 (purple) were on the poleward edge of the trough, near the positive gradient into a region of density enhancement due to auroral precipitation. Both IPP time series showed low VTEC (10-15 TECU), with a slight increase in the FFT power for PRN 7 — likely due small-scale structure in the auroral enhancement — and also, though less clear, for PRN 16.

Figure 3.5 shows the interval between 23:10 and 23:20 UT. Shortly after the period shown in Figure 3.4, PRN 23 continued to track just poleward of the SED plume and showed a slight decrease in VTEC with some increased FFT power near 100 mHz.

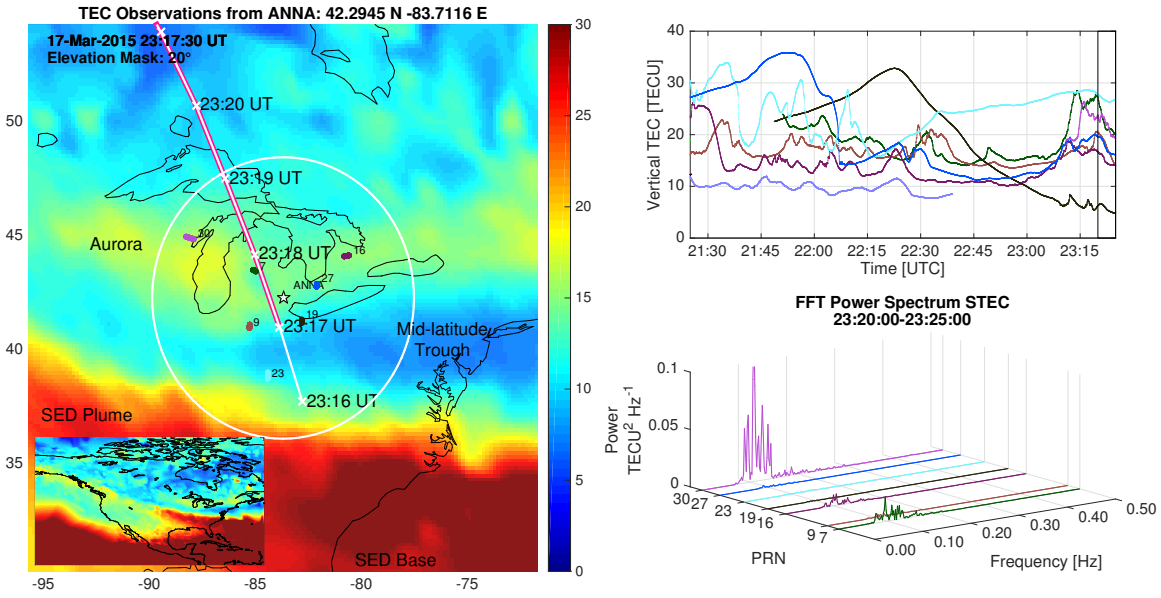

Figure 3.5: *Left:* Interpolated Madrigal VTEC map with 5-minute IPP tracks for the interval ending at 23:205 UT. The SED plume, SAPS, trough, and auroral enhancement are visible from bottom to top and all of the IPP tracks (except PRN 23) are located within the auroral zone. The magnetic footprint track for DMSP F17 mapped to 300 km altitude (white line) is also shown with the detected enhanced particle precipitation (shown in Figure 3.6) flux highlighted in magneta along the track beginning near ∼41°N. *Inset:* TEC over North America. *Right Top:* The cumulative VTEC time series from 23:25. *Right Bottom:* The 5-minute STEC FFT for the observable GPS PRN.

PRN 19, which had previously been parallel to PRN 23, continued its poleward track and traversed the low-density trough — measuring VTEC ∼5 TECU. PRN 9, 16, and 27 continued to track poleward and crossed into the region of auroral enhancement. They showed the expected increase in VTEC and strongly increased FFT power on a band around ∼100 mHz extending to 350 mHz (in the case of PRN 7). PRN 7 and 30 (violet) traverse the edges of the densest regions of the auroral enhancement. They showed the expected increase in VTEC from auroral ionization and also a strong increase in FFT power centered around 100 mHz, but also broad increases to 200 mHz. Similar observations are made through 23:30 after which VTEC decreases for most PRN with low amplitude fluctuations in FFT power near 100 mHz. During this time PRN 11 (sea green) crossed the plumes poleward edge, but tracking northward from inside the plume it observed only slight increases in FFT power beginning near 100 mHz and extending to nearly 400 mHz. This is contrasted with earlier crossings of the plume's poleward edge that were closer to the tip of the plume and observed much more intense variations.

3.5 Auroral Observations

Figure 3.6 shows DMSP particle flux intensity at 22:00, 23:00, and 23:20 UT measured near the observation region. At 22:00 UT DSMP satellite F19 observed increased proton and electron flux at 44.4°N, -60.2°E geodetic, suggesting the auroral boundary was poleward of the SED plume within one hour of the Ann Arbor observation magnetic local time (MLT). AMPERE summary plots also indicate upward radial current beginning at ∼44-45°N geodetic latitude at Ann Arbor MLT, further suggesting that electron precipitation, and consequently the equatorward auroral boundary, began at least several degrees poleward of the SED plume's poleward edge. Similarly, at 23:00 and 23:17 UT, DMSP satellites F16 and F17 both observed increased precipitation fluxes beginning at least ∼5° latitude

poleward of the SED plume. Figure 3.5 shows the magnetic footprint track for DMSP F17 mapped to 300 km altitude as a white line with the enhanced particle flux shown in Figure 3.6 highlighted in pink beginning near $\sim$41°N.

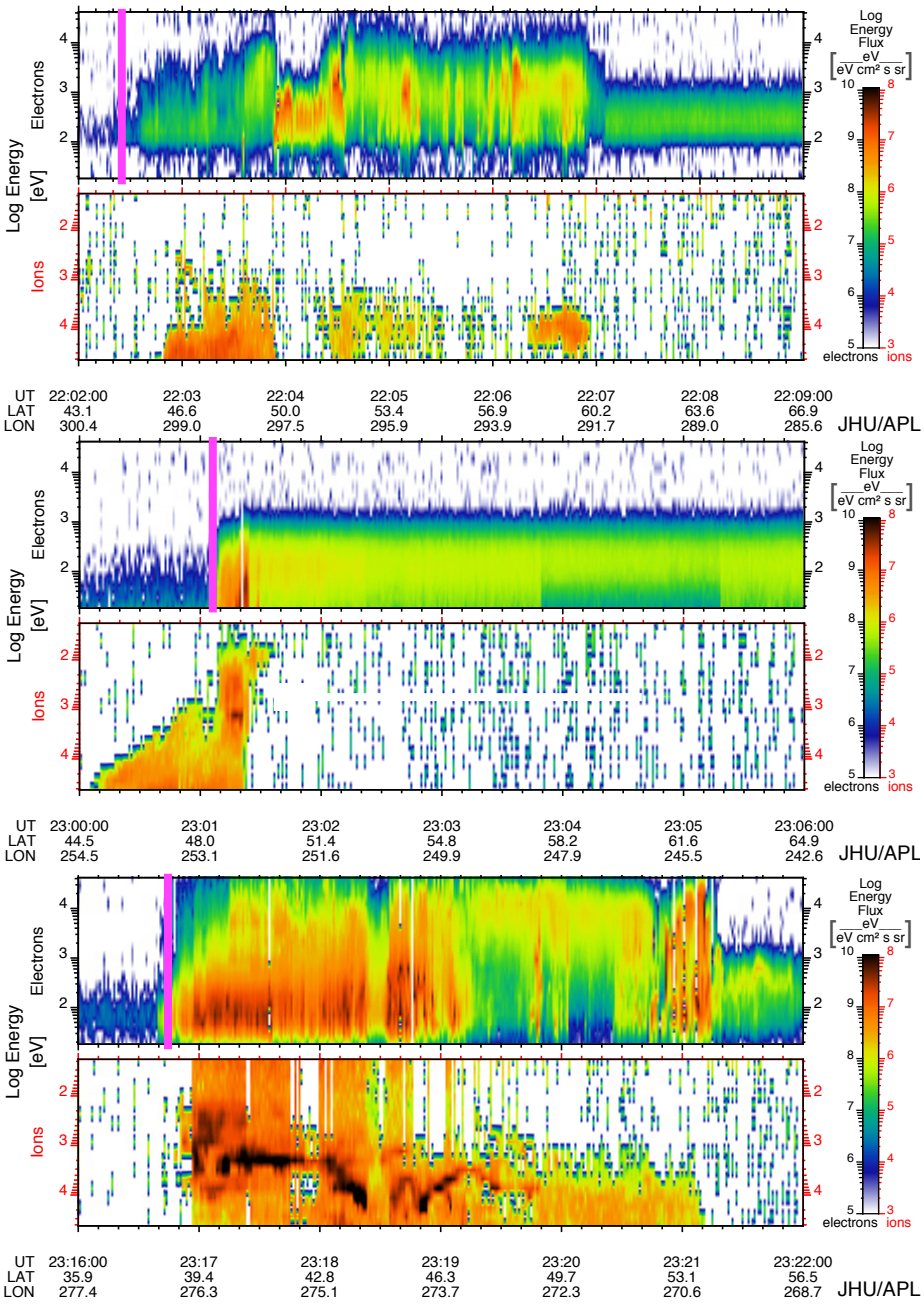

Figure 3.6: DMSP particle precipitation fluxes. Equatorward auroral boundaries are indicated in magenta. *Top:* DMSP F19 particle flux showing auroral electron precipitation was 4° poleward of the SED plume within 18° east (1.2 hours MLT) of the observation area. *Middle:* DMSP F16 showing auroral precipitation beginning $> 2°$ poleward of the SED plume within 15° west (1 hour MLT) of the observation area. *Bottom:* DMSP F17 showing auroral precipitation beginning $> 2°$ poleward of the SED plume within the observation area consistent with TEC enhancement observed in this region at the time.

3.6 Discussion

During the passage of the SED plume on 17 March 2015, TEC measurements between 17-Mar 20:00 UT and 18-Mar 03:00 UT are consistent with the pattern illustrated by Figures 3.3, 3.4, and 3.5. Several general trends are observed. First, there is little observed TEC variation equatorward of the advancing SED plume, along its equatorward edge, or through the plume peak. This is illustrated clearly by PRN 3, which does not cross the SED plume and travels ahead of the advancing equatorward edge of the plume throughout the observation, and showed only occasional TEC variability — comparable with FFT spectra during quiet-time conditions. Meanwhile, the TEC time series and FFT spectra of other PRN traveling poleward and crossing the SED plume show smooth increases in TEC with very little spectral power above the background. This suggests that small-scale irregularities are scarce equatorward of the SED plume and that the plume itself also contains few small-scale variations.

However, observations near the plume's poleward edge are quite different. As the PRN IPPs crossed the poleward edge of the SED plume and its boundary with the trough, sudden decreases in VTEC were accompanied by rapid fluctuations on multiple scales as indicated by the VTEC time series and FFT spectra, which showed increased power between 100 and 300 mHz. This is consistent with the variability asymmetry between equatorward and poleward gradients reported by *Coster* [2007] and *Sun et al.* [2013]. Minor TEC fluctuations at similar frequencies occurred around the edge gradients of the trough minimum, but diminished once the IPPs had tracked inside it. Finally, as the PRN IPPs moved into the trough/auroral boundary, there was again an increase in VTEC variability and the FFT spectra showed increased power around 100 mHz that was similar to that observed during crossings of the SED plume's poleward edge. This demonstrates that the SED plume's poleward edge is capable of exhibiting TEC fluctuations of

comparable amplitude to those observed in the aurora.

Importantly, DMSP and AMPERE observations confirm that GPS TEC variability observed in and around the SED plume was not due to colocated auroral irregularities. At both 22:00 and 23:00 UT, DMSP indicated vertical proton and electron fluxes beginning poleward of the SED plume respectively by four degrees latitude within one hour MLT to the east, and two degrees latitude directly in the observation area. AMPERE Field-Aligned-Current (FAC) plots at 22:00 (Figure 3.7) also indicate downward FAC extending equatorward to $\sim$44° geographic latitude while the SED plume's poleward edge was located at $\sim$42°.

During this same period, data from both Millstone Hill Incoherent Scatter Radar (ISR) and the SuperDARN radars at Christmas Valley East, Blackstone, Fort Hays East, and Wallops Island (e.g., Figure 3.1) show ion velocities within the Ann Arbor observation area of $\sim$1000 ($\pm$300) $\mathrm{m\,s^{-1}}$ in the F-region. Assuming the irregularities are frozen-in with the bulk ion flow, the increased spectral power observed in IP crossings of the SED/trough and Auroral /trough interfaces is consistent with what would be expected for irregularities between 3 km ($\pm$900 m) and 10 km ($\pm$3 km) in size transported past the IPPs at those velocities. Meanwhile, the IPPs move at 50 $\mathrm{m\,s^{-1}}$, which is nearly stationary relative to the ion flow and only slightly influence the observed frequency of FFT power ($\pm$10 mHz). The presence of intermittent phase cycle slips (loss of cycle count tracking) logged in the Ann Arbor GPS Receiver Independent Exchange Format (RINEX) files also strongly suggest the presence of small-scale ionospheric structures interfering with the GPS signal. Importantly, it should be noted that the cycle slips do not contribute to the FFT spectra because any contributions to the STEC time series are occasional, sporadic and step-like within the five-minute FFT window and contribute power at much lower frequencies ($\sim$1 mHz) with periods on the order of tens of minutes to hours — well below the highpass filter's frequency stop at 30

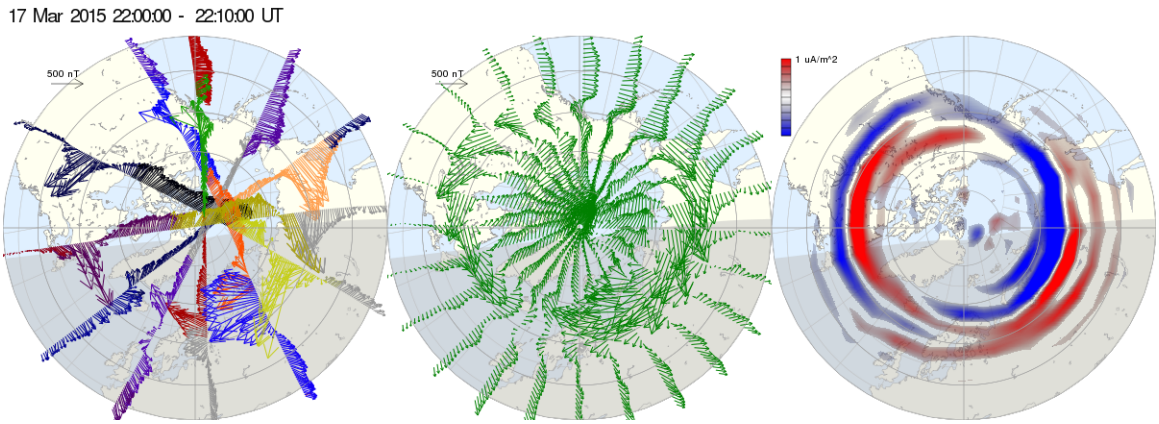

Figure 3.7: *Left:* Measured horizontal magnetic field disturbances measured by AMPERE onboard the Iridium constellation of spacecraft. *Middle:* Fitted magnetic disturbance vectors. *Right:* Corresponding current flux to magnetic disturbance showing the approximate location and intensity of the FACs.

mHz.

In their recent paper, *Cherniak and Zakharenkova* [2015] suggest that irregularities observed in the polar cap may be transported from the mid-latitude SED plume. The present observation and detection of small-scale irregularities are evidence supporting this suggestion. It further suggests that SED associated irregularities have an impact that reaches beyond mid-latitudes into the high latitude polar cap and underscores the importance of research into SED associated irregularities. Furthermore, observations of longitudinal asymmetries in TEC structure between PRN with near-simultaneous crossings of the SED plume, such as those described in sections 3.2 and 3.4 demonstrates that the plume exhibits medium-scale variability observed at higher latitudes along the boundary of the plume that are not observed closer to the SED base region. This suggests that structuring of the plume on the order of tens to hundreds of kilometers may be occurring as the plume moves toward the cusp and may be an early indicator of the formation of patches [*Zou et al.*, 2014].

CHAPTER IV

Characterization of Mid-Latitude TEC Variability in SED Plume Systems

This chapter surveys twelve of the largest geomagnetic storms that produced SED plumes in the available dataset from 2012-2016 to extend the analysis that was done for the 17-March-2015 storm to a broader variety of storms. All twelve storms had Dst <-80 nT and were selected for this study based on the strength of the storm and the production of an SED plume observable by the ANNA station. The objectives of this chapter are to demonstrate the applicability of the approach developed for the case study in Chapter III and described in Chapter II, to demonstrate variety of small-scale TEC variability in SED plume systems across just a subset of available storms, and to motivate and inform future studies of small-scale, mid-latitude TEC variability. In doing so, it seeks to answer the following questions:

1. What level of variability should we expect to see in such storms at mid-latitudes?

2. Are some regions of the SED system more prone to higher variability and thus potentially scintillation?

3. Which factors, such as Universal Time (UT) and Local Time (LT) dependency, storm strength, and storm phase during SED observations, affect

the small-scale variability of the SED plume system?

4. How frequent are phase cycle slips and where within the SED system should we expect them to occur?

4.1 Methodology for Multi-Event Studies

Table 4.1 shows the storms that were used in this analysis. Candidate storms were identified using an algorithm that searched one-hour Dst data for local peak values and their relative prominence in relation to other local extrema. This reduced the misidentification of storms due to multiple dips below the threshold during a single event. Sudden Storm Commencement (SSC)s were detected in a similar manner, though with a positive threshold of 10 nT. For the purpose of illustration, Figure 4.1 shows the period 2007-2016 with detected storm minima and SSC. Each storm

Table 4.1: List of Storms Surveyed

Storm No.	**Date & Time of Min Dst [UT]/[LT]**	**Min Dst [nT]**	**Storm Phases of SED Observation**
1	15-Jul-2012 19:00/14:00	-127	Initial, Main, Recovery
2	01-Oct-2012 05:00/00:00	-119	Initial, Main, Recovery
3	09-Oct-2012 09:00/04:00	-105	Initial, Main, Recovery
4	19-Feb-2014 09:00/04:00	-116	Main, Recovery
5	28-Feb-2014 00:00/19:00	-94	Main, Recovery
6	17-Mar-2015 23:00/18:00	-223	Main, Recovery
7	23-Jun-2015 05:00/00:00	-204	Initial, Main, Recovery
8	09-Sep-2015 13:00/08:00	-98	Main, Recovery
9	20-Dec-2015 23:00/18:00	-155	Main, Recovery
10	20-Jan-2016 17:00/12:00	-93	Initial, Main, Recovery
11	06-Mar-2016 22:00/17:00	-98	Recovery
12	08-May-2016 09:00/04:00	-83	Recovery

was then processed using the methodology described in Chapter II to produce animations for the full interval during which an SED plume was visible. In order to standardize the analysis performed on the 17-March-2015 storm in Chapter III, the

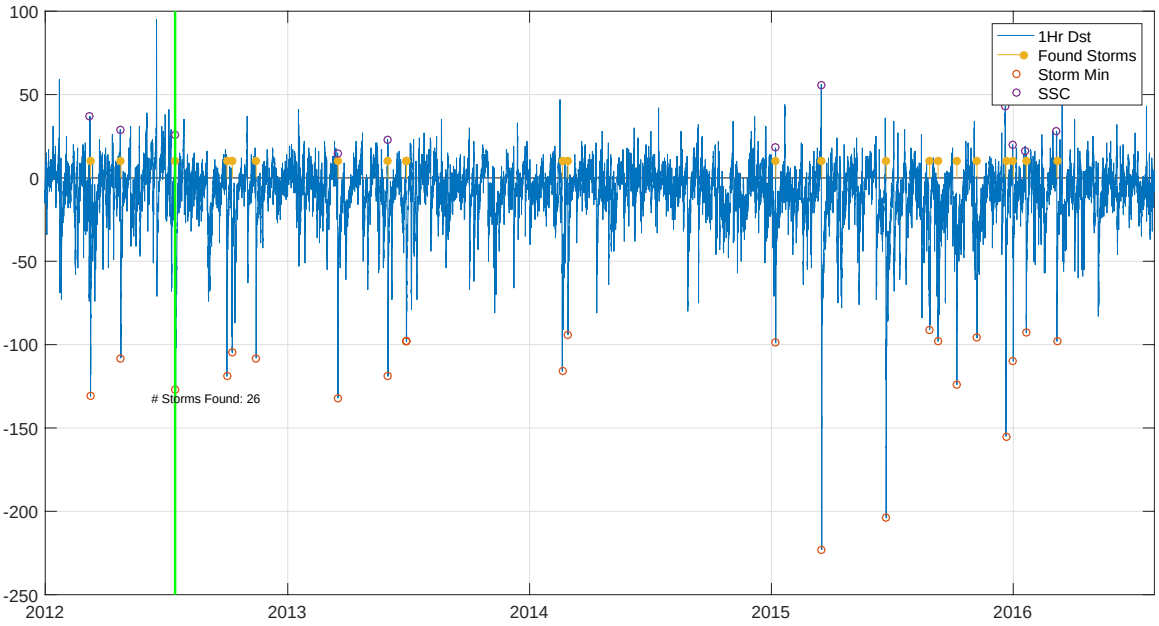

Figure 4.1: Storms and SSC detected from the one-hour Disturbance Storm-Time index Dst spanning 2007 to 2016. Red open circles show the detected storm minima and the yellow flags (filled circles with stems) indicate their place during this time interval while the purple open circles show sudden storm commencement events. The green line indicates the beginning of Ann Arbor GPS TEC data availability.

three metrics shown in Table 4.2 were devised to characterize the FFT spectra for each five-minute interval during the storm. These metrics were calculated for each

Table 4.2: FFT Spectrum Metrics Description

Spectrum Metrics	**Description**
Maximum Amplitude	Highest peak in the FFT spectra above the high pass filter threshold (0.08 Hz)
Frequency of Maximum Amplitude	Frequency of maximum amplitude
Maximum Frequency	Highest frequency above threshold amplitude of 0.005 $TECU^2$ Hz^{-1}

candidate storm in five-minute windows every 150 seconds. In the case study, the advancement was done in ten second increments, however that study revealed that FFT could be adequately characterized at a slower cadence with 50% overlap between spectra. The spectrum metrics were then tabulated by time and PRN. Finally, the table was populated with IPP location classifications using the

animations (VTEC and TEC maps) as a guide. The IPP locations were then assigned one of nine regions in the SED plume system as defined in Table 4.3 and labeled in Figure 4.2.

Table 4.3: SED plume regions used to describe the locations of Ionospheric Pierce Points

Label	**Region**	**Description**
A	Plume Base Region	The region of Storm Enhanced Density at lower latitudes from which the plume originates
B	Equatorward Plume Edge	The region of increasing density marked with an inflection point in VTEC time series
C	Plume	The region of Storm Enhanced Density prior to the inflection point marking the poleward plume edge
D	Equatorward	The relatively undisturbed ionosphere equatorward of the advancing plume
E	Poleward Plume Edge	The region of decreasing desnity marked with an inflection point in theVTEC time series
F	Mid-latitude Trough	The region of low density poleward of the SED plume
G	Aurora	The region of auroral enhancement indicated in the TEC map and DMSP observations of electron flux

Two additional descriptors were recorded to describe observations that weren't adequately described by these seven location classifications. "Plume Pocket" and "Plume Dissipation" describe two special cases of IPP classification. "Plume Pocket" describes a region that is westward and/or equatorward of the SED plume, but simultaneously near the poleward edge of the SED base region and appears to fit the description of the "notch" described by *Goldstein et al.* [2003] when mapped into the ionosphere. In these observations "pocket/notch" essentially corners the IPP which then encounters both poleward and equatorward gradients while still on the opposite side of the SED plume from SAPS or convection flow. Figure 4.3 shows an example of this case. The other special case of IPP classification, "Plume

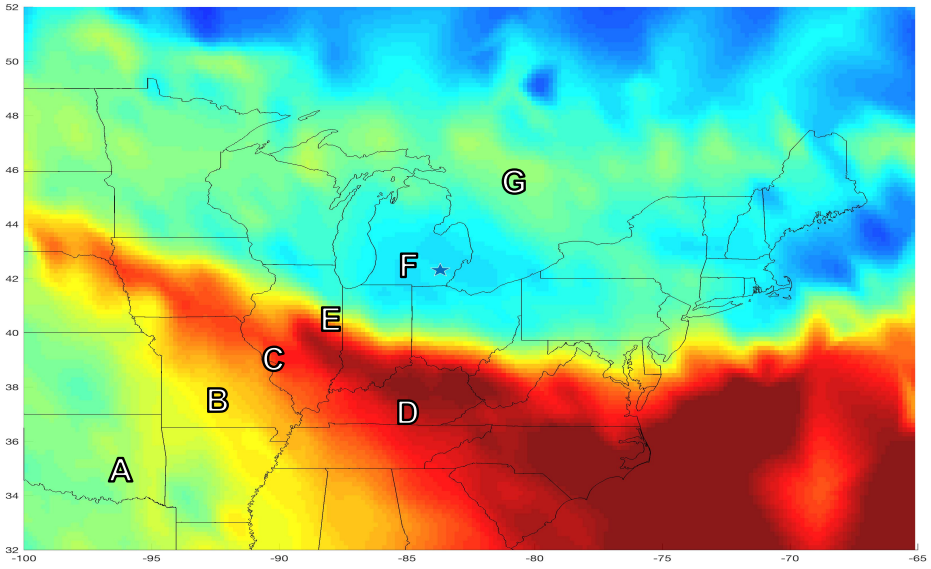

Figure 4.2: Examples of distinct regions within an SED plume system.

Dissipation" refers to the circumstance where the plume rapidly loses its coherent structure over a few minutes while the IPPs are still within its bounds. In this case, the IPPs don't track across the SED plume's boundary and the plume essentially fades away around them.

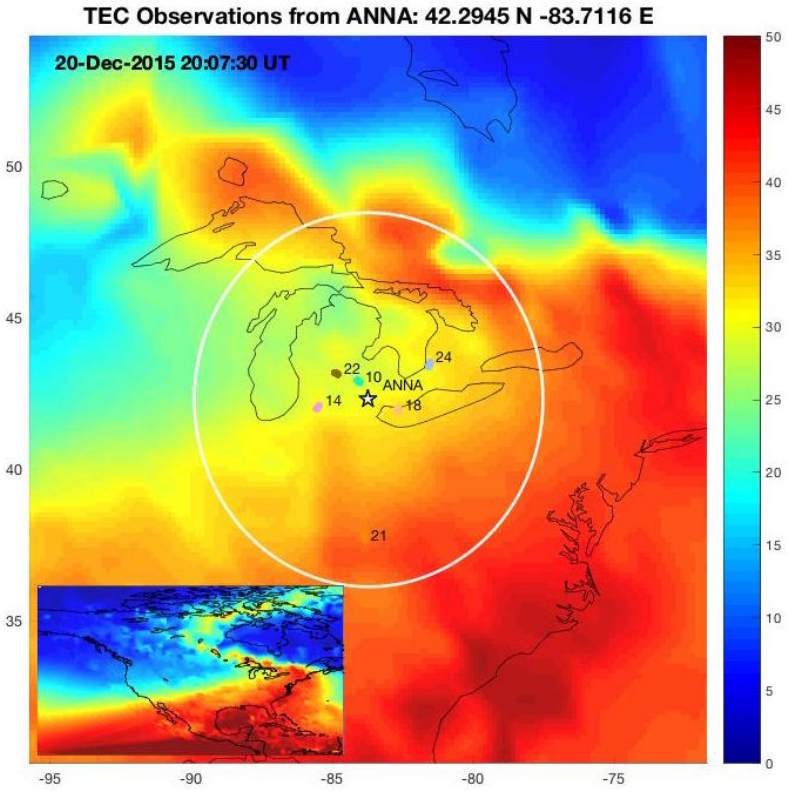

Figure 4.3: Plume Pocket example. The plume pocket is defined as an equatorward region of the SED plume that is also near the poleward edge of an extended SED base region.

4.2 Cycle Slips

A complicating factor in analyzing the STEC FFT spectra in some storms is the presence of phase tracking slip, or cycle slips, by the receiver. This occurs when the receiver, which tracks both the PRN code sequence (coarse acquisition tracking) and the carrier phase (fine precision, uncertain accuracy), loses count of the integer number of carrier cycles it uses to maintain precise positioning. Typically this is acquired after several seconds of comparison with the PRN code phase, but sudden changes in the usually steady-state tracking loop can cause the receiver to lose carrier phase tracking and reacquire. This can occur for a variety of reasons including doppler shift for a fast moving receiver and multi-path effects due to reflections off of objects nearby. However, in the case of the ANNA station, there is

no motion from the fixed receiver, and multi-path effect are typically not observed. In this case, the cycle slips are mostly like attributed to sudden changes in ionospheric density causing a fluctuation in signal intensity or phase. The cycle slips manifest themselves in TEC data as sudden step functions which are followed by the usual characteristic damped sine function step response as the receiver reacquires carrier phase tracking. Unfortunately, the response to the step function in the frequency domain puts power across the spectrum and contaminates the analysis of small scale TEC structure. Therefore, it is necessary to identify the intervals with cycle slips and exclude them from the irregularity analysis, but owing to their intrinsic impact on the GPS signal and subsequent TEC measurement, the time and location of cycle slip intervals is also a valuable observation.

Horvath and Crozier [2007] used a method to identify cycle slips in detrended TEC data as discontinuities >1.5 TECU and gaps between samples greater than the 30 s sampling period used in that study during a given GPS spacecraft pass. This method has been frequently cited and employed with customizations appropriate to the application e.g., *Afraimovich et al.* [2005]; *Prikryl et al.* [2010]; *Carrano et al.* [2016]. In this study, cycle slips were identified similarly. The STEC data were detrended using the same tenth-order Butterworth filter described in Chapter II to remove the large scale, low frequency background. However, the method for cycle slip detection differs from that used by *Horvath and Crozier* [2007] because a fixed amplitude threshold did not adequately catch cycle slips and misidentified changes in STEC where tracking was maintained. Instead, a peak prominence method was applied that ranked each peak in the detrended STEC time series according to its height above the shallowest trough between the next highest peak to either the left of right. The results were then validated against the VTEC and FFT animations for intervals with obvious cycle slips.

4.3 Normalization of Observations

The number of observations in each region of the SED system depends on the relative size of the feature. For example, the SED plume is generally horizontally narrow compared to the trough or SED base region. Therefore, to make fair comparisons of variability within regions, the occurrence of variabilities in a region must be normalized by the total number of observations in the region. Similarly, storm phases were observed in different periods for different durations of time. These results also are normalized by the total number of observations as appropriate. Figures 4.4 and 4.5 illustrate the proportion of observations in the SED system and during different storm phases respectively.

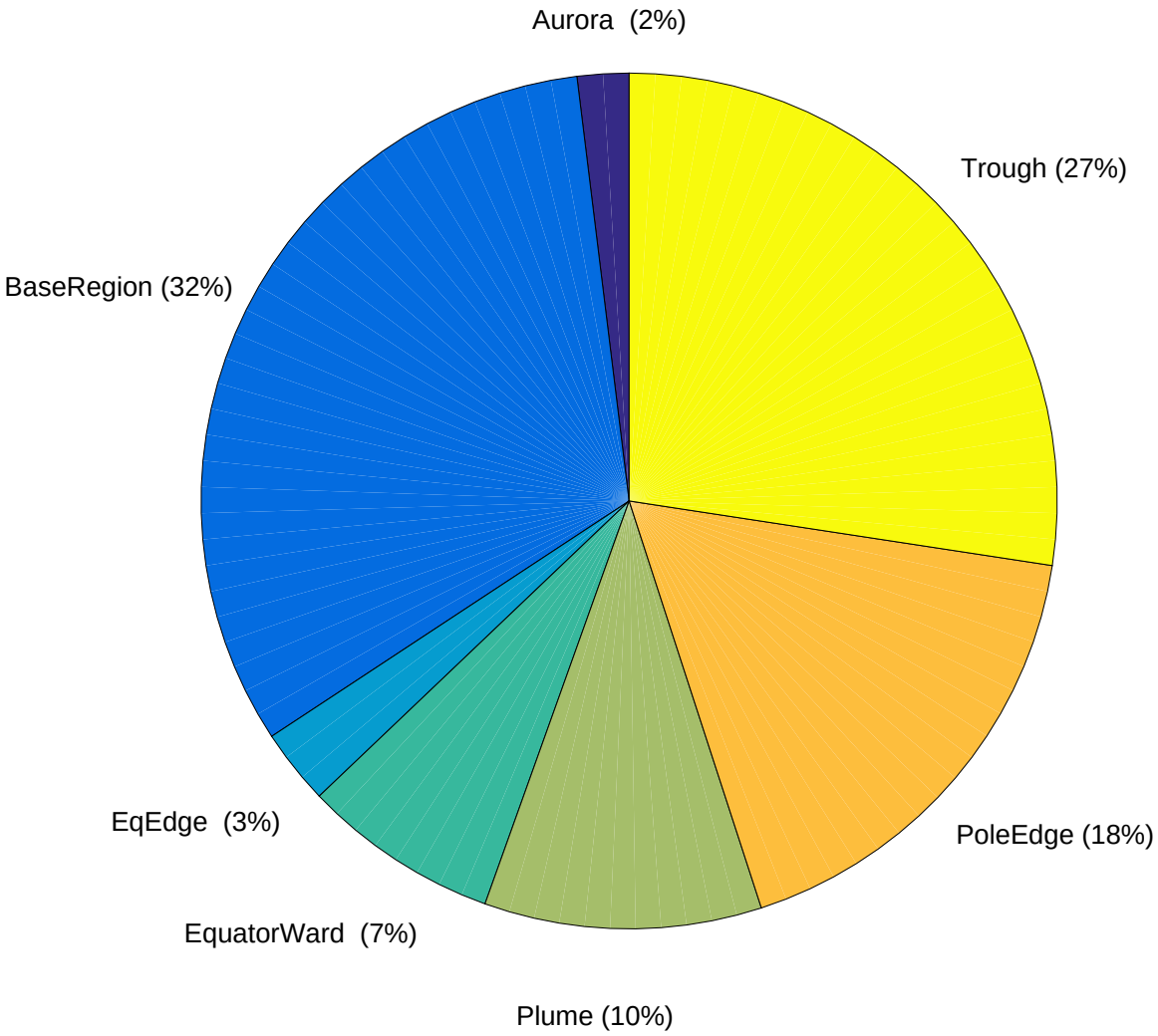

Figure 4.4: Relative proportion of SED regions observed.

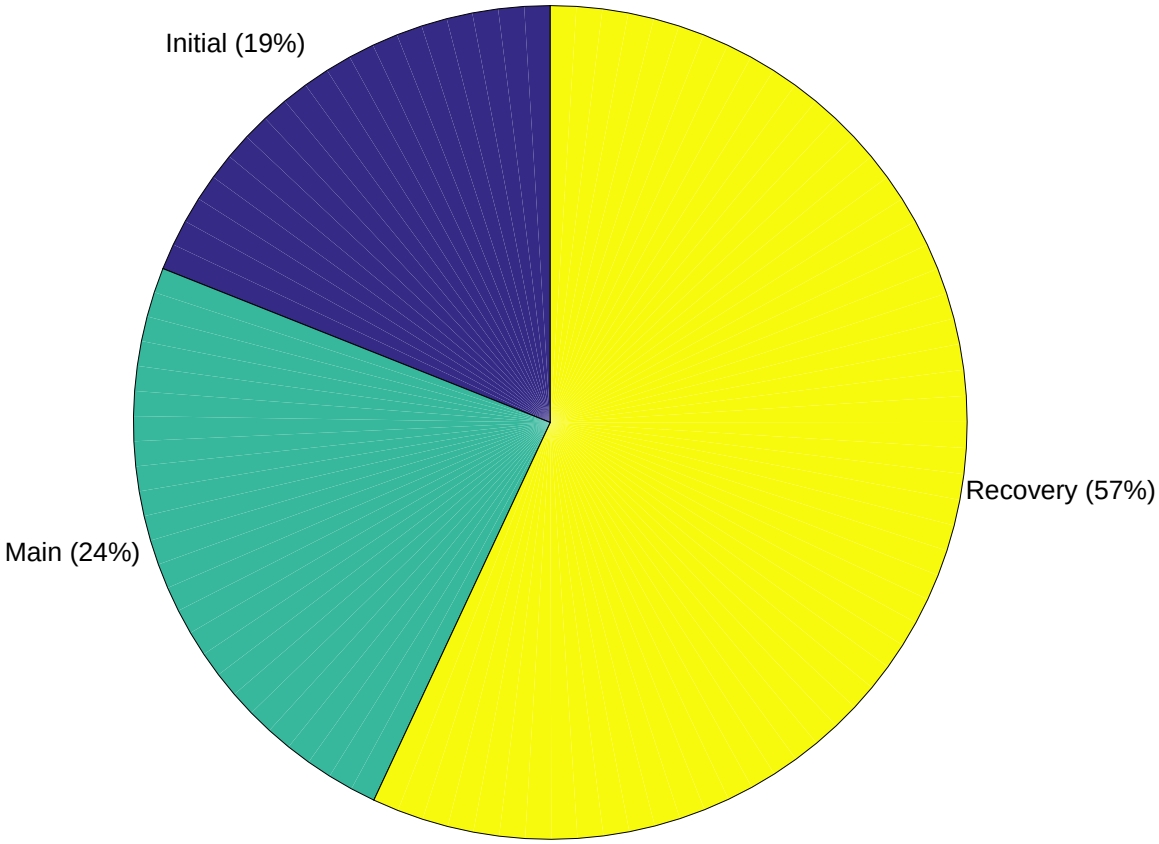

Figure 4.5: Relative proportion of observations in each storm phase.

4.4 Results

Storms were first compared against each other by each of the three metrics from Table 4.2 identify different characteristics in each storm as shown in Figures 4.6, 4.7, and 4.8. Each storm was then decomposed into the relative contributions from each of the SED regions to determine which regions were most influencing the storms' characteristics (Figures 4.9, 4.10, and 4.11). Finally, observations were separated by storm phase first by storm and then by the relative contributions of SED regions to determine what role storm phase has in influencing TEC variability.

4.4.1 Storm TEC Variability

Highest Frequency Overall Figure 4.6 illustrates that some storms only have spectral power below 200 mHz, suggesting that most TEC variability is occurring due to larger variations on the order of ∼10 km or more. For others, e.g., Storms 1, 2, 3, and 9, show power at higher frequencies up to the Nyquist frequency at 500 mHz. For these storms, the increased number of observations with power near Nyquist also suggests that there is power at higher frequencies above the Nyquist rate and therefore even greater TEC variability in those storms.

Frequency of Maximum Power Figure 4.7 shows that the most power occurs at low frequencies near 100 mHz for all storms in this study. Since this near the band-stop frequency of the filter, the consistent power here is likely due to that cut-off and does not reflect a characteristic of the storms observed. However, storm 5 does show some spectra that peak in power ∼280 mHz, but the power is very low because it does not show in Figure 4.6 meaning that the power at frequency must be below the 0.005 $TECU^2$ Hz^{-1} threshold. Furthermore, this also suggests that the amplitude of variability at frequencies above 200 mHz is very low compared to the low frequency power. This is expected as the irregularity amplitude and length scale

are expected to follow a power law distribution for intensity and size.

Maximum Power Figure 4.8 shows that most observations were at low power below 0.1 $TECU^2$ Hz^{-1}. However, Storms 2, 3, and 9 show power reaching up to 0.2-0.3 $TECU^2$ Hz^{-1}. Since Figure 4.7 shows that the highest power for these storms occur at low frequency, this suggests that there were more steep, large-scale gradients in these storms than in the others.

4.4.2 Storm TEC Variability By Region

Highest Frequency Analysis of each storm by SED system region shows that power at higher frequencies (above 200 mHz) tended to come from the same core group of regions, with a few additional contributors. Focusing on storms 1, 2, 3, and 9 — based on Figure 4.6 because of their observed power at high frequencies — Figure 4.9 reveals which SED regions contribute to those higher frequencies. For Storm 1, regions D, E, and F (see Figure 4.2 for region labels) contributed all of the power above 400 mHz. Storms 2 and 3 show the same pattern, but with the addition of the aurora (region G). Aurora was observed in Storms 1 and 6, but it those instances, it did not have power at frequencies above 200 mHz. Storm 9 again shows the same pattern, but with a contribution from the plume (region C).

Frequency of Maximum Power All twelve storms consistently show that the maximum spectral power occurred at low frequencies near ∼100 mHz. There are two exceptions: Storms 5 and 6. Storm 5 had a small percentage of observations where the maximum power occurred near 300 mHz — occurring in regions E and F. Storm 6 showed power up to ∼450 mHz in region F.

Maximum Power Most storms in this study show essentially no distinction between regions for maximum amplitude. The two exceptions to this trend are

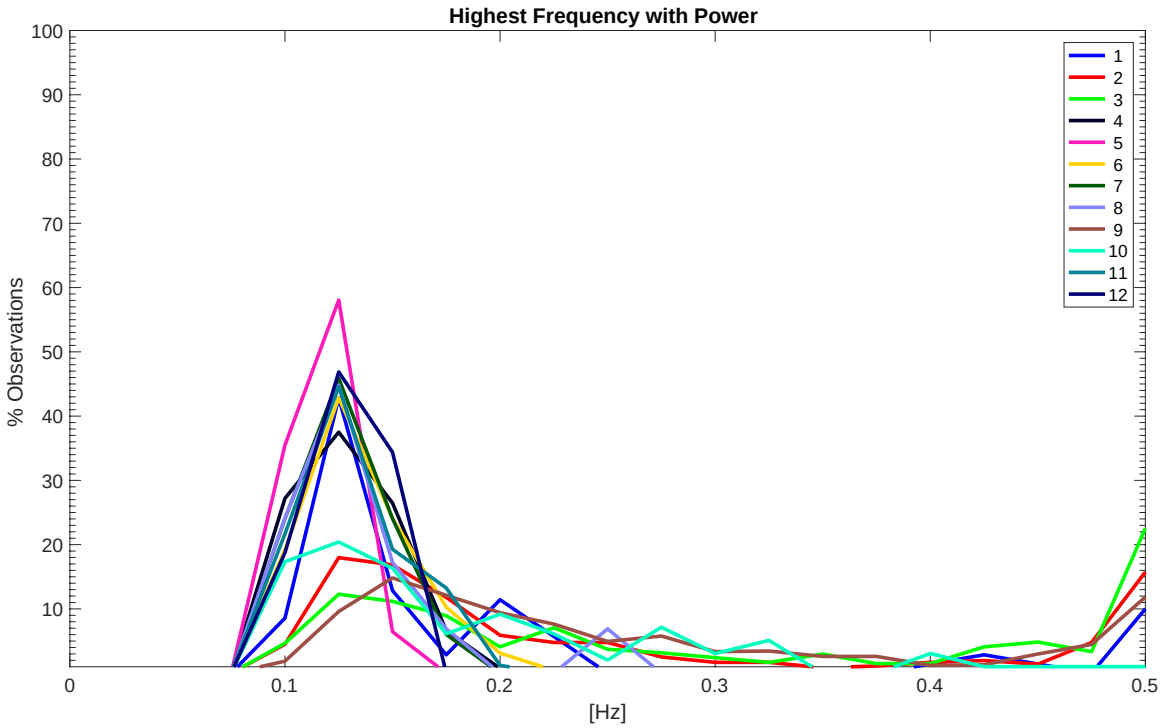

Figure 4.6: Percent distribution of maximum spectral frequency over observations from all twelve storms with each storm indicated by color.

Storms 3 and 9. Storm 3 had nearly 10 percent of observations with power above 0.2 $TECU^2$ Hz^{-1} contributed at the poleward edge (region E) and Storm 9 had over 10 percent of observations with 0.2 $TECU^2$ Hz^{-1} observed in region F. This, along with Figure 4.10 suggests that, in some cases, these regions (E and F) can exhibit higher amplitude variability at higher frequencies than are produced from larger scale gradients. This suggests that small-scale irregularities can have intensities sufficient to stand out from the background gradients in some cases.

4.4.3 Effect of Storm Phase on TEC Variability

Observations from each storm were classified and sorted by the storm phase during which they were observed and the same metrics were compiled as before. This showed higher power in main and recovery phases (Figure 4.12) , the distributions of frequency of maximum power was unchanged with storm phase (Figure 4.14), and

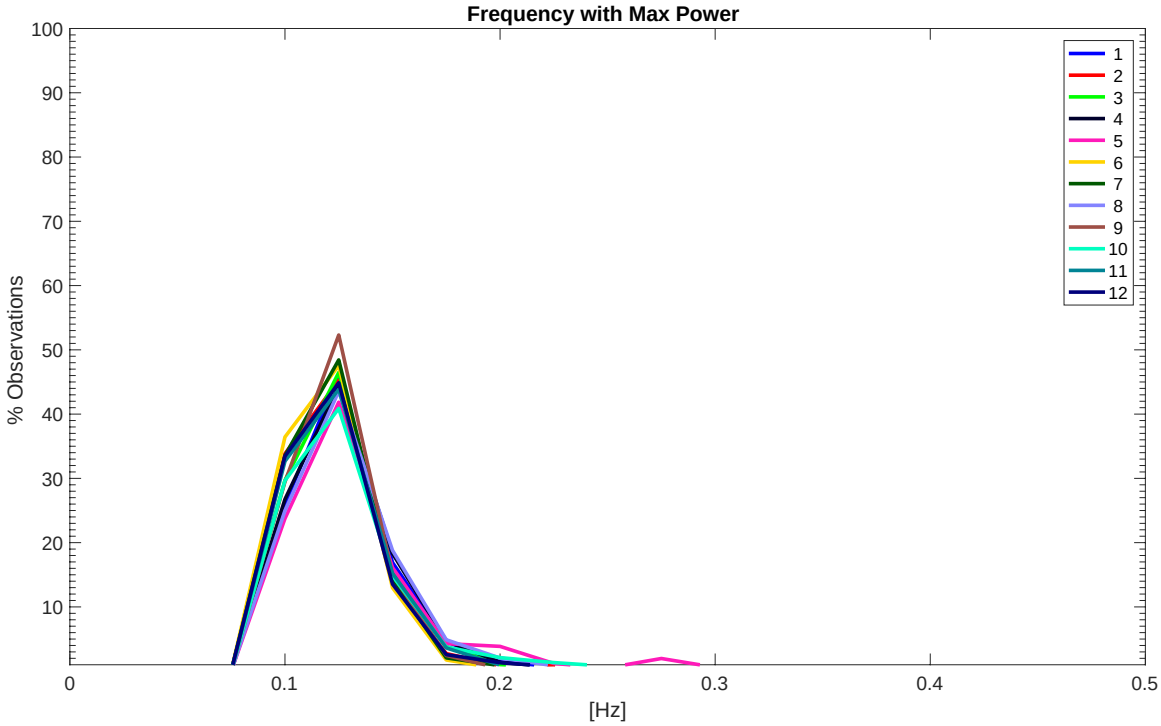

Figure 4.7: Percent distribution of maximum spectral power for each storm.

the highest frequency (Figure 4.13) showed differences in which storms had variability at frequencies above 400 mHz, but no clear pattern as to why. Storms 1, 2, 3, 7 and 10 were observed during the initial phase and storms 1, 2, and 3 contributing power above 400 mHz. Whereas during the main and recovery phases, storms 2, 3, and 9 contributed the most to higher frequencies.

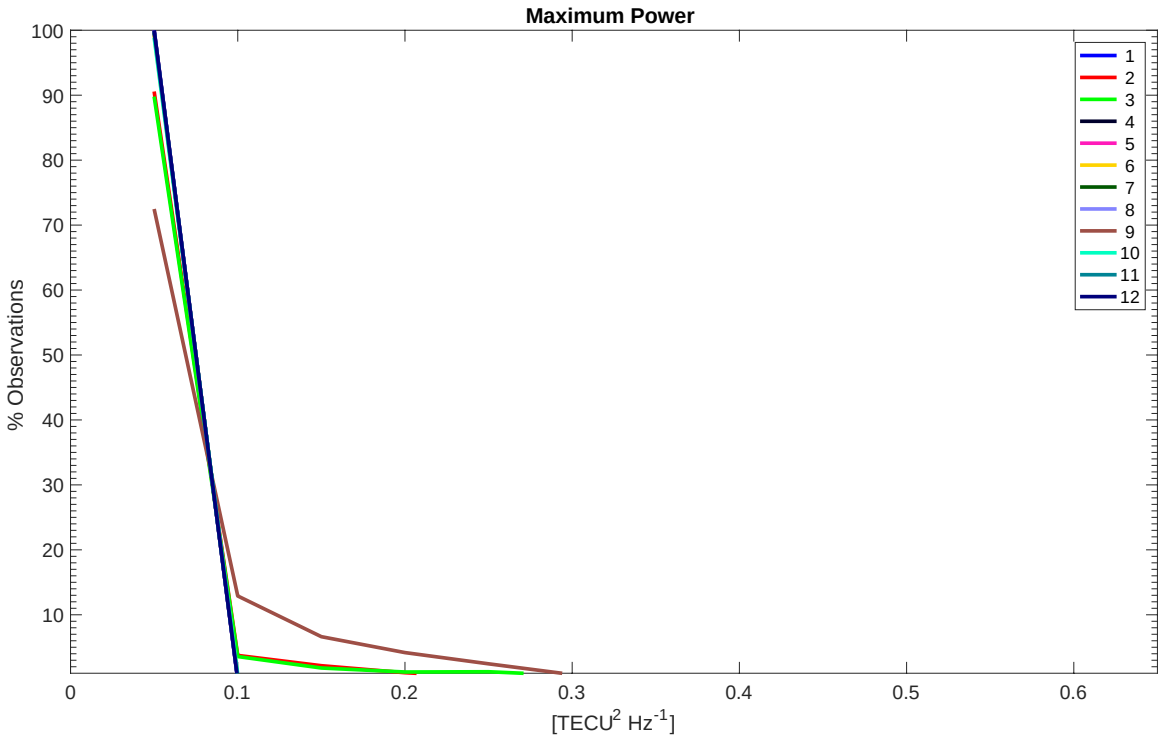

Figure 4.8: Percent distribution of maximum spectral power distribution for each storm.

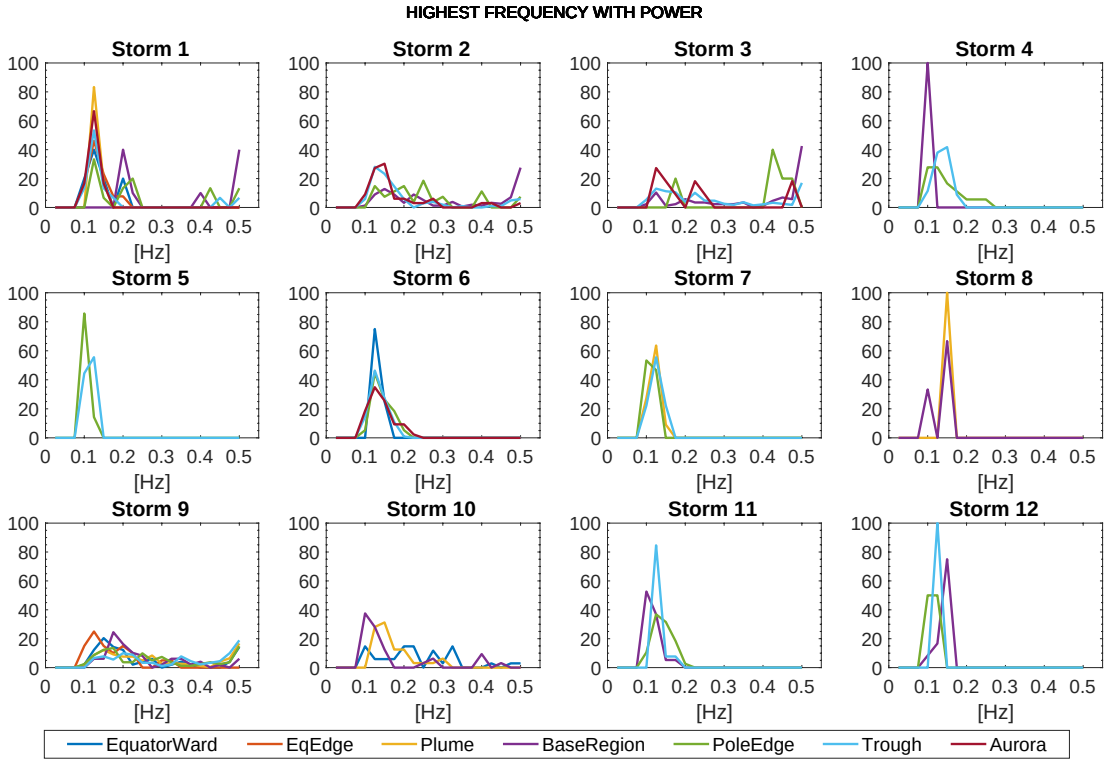

Figure 4.9: Percent distribution of maximum spectral power for each storm.

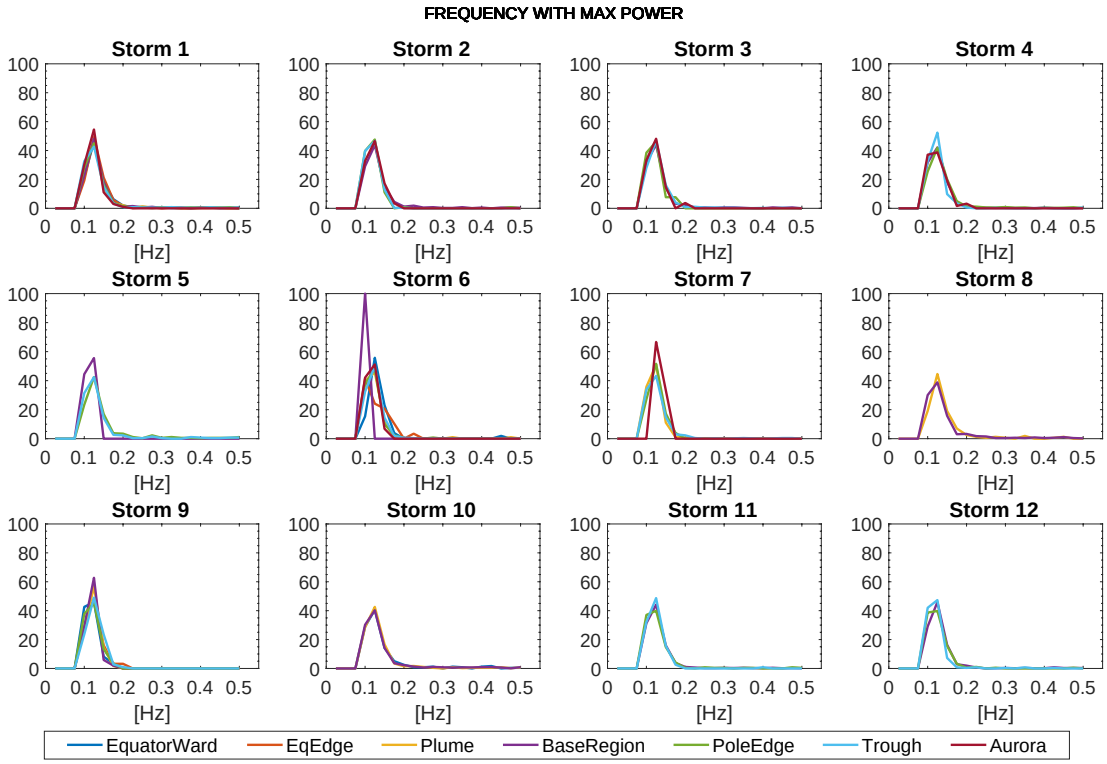

Figure 4.10: Percent distribution of maximum spectral power for each storm.

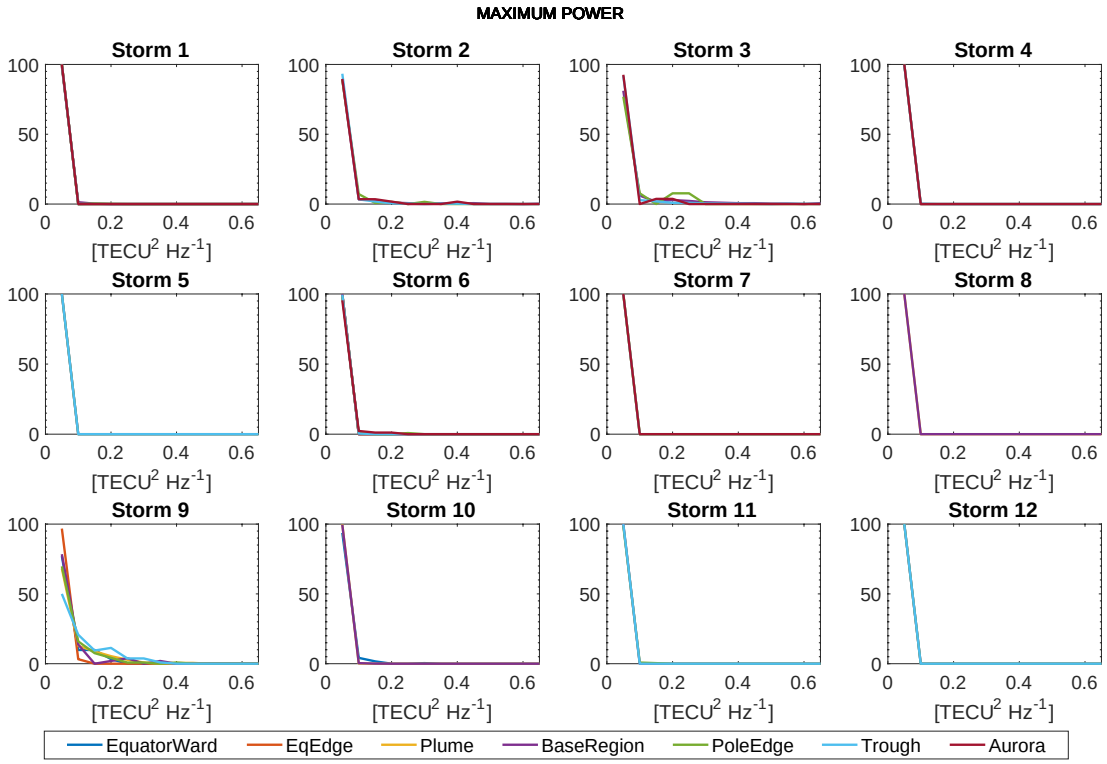

Figure 4.11: Percent distribution of maximum spectral power for each storm.

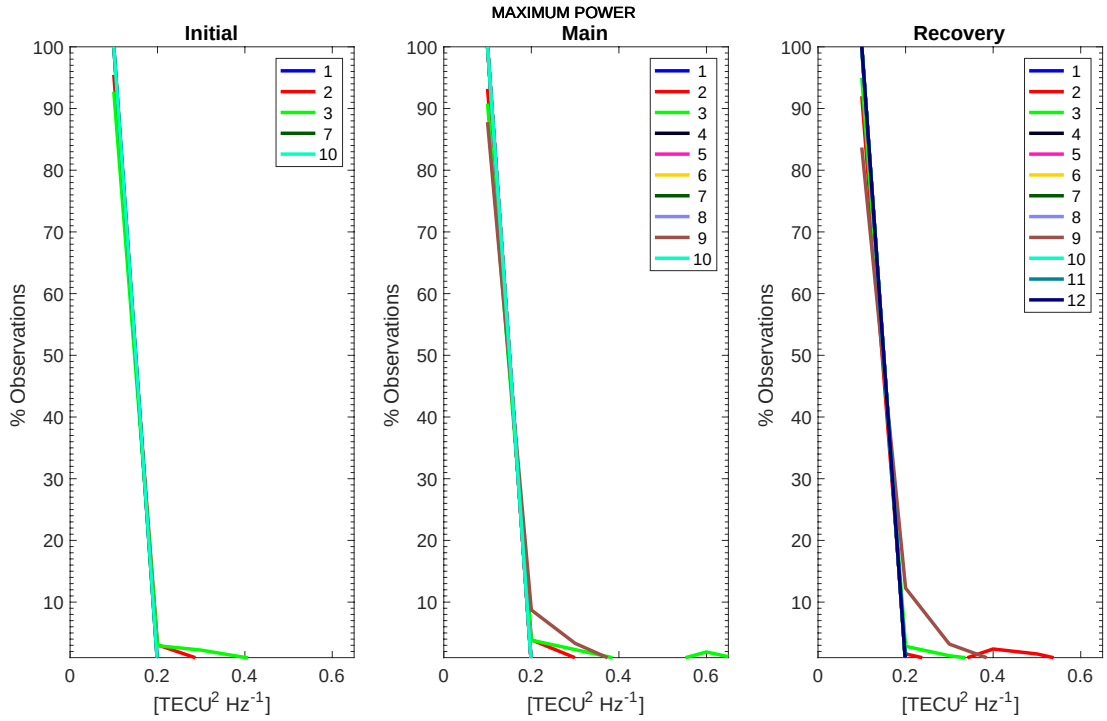

Figure 4.12: Maximum power of storms (indicated by different colors, see legend) separated by storm phase during observation.

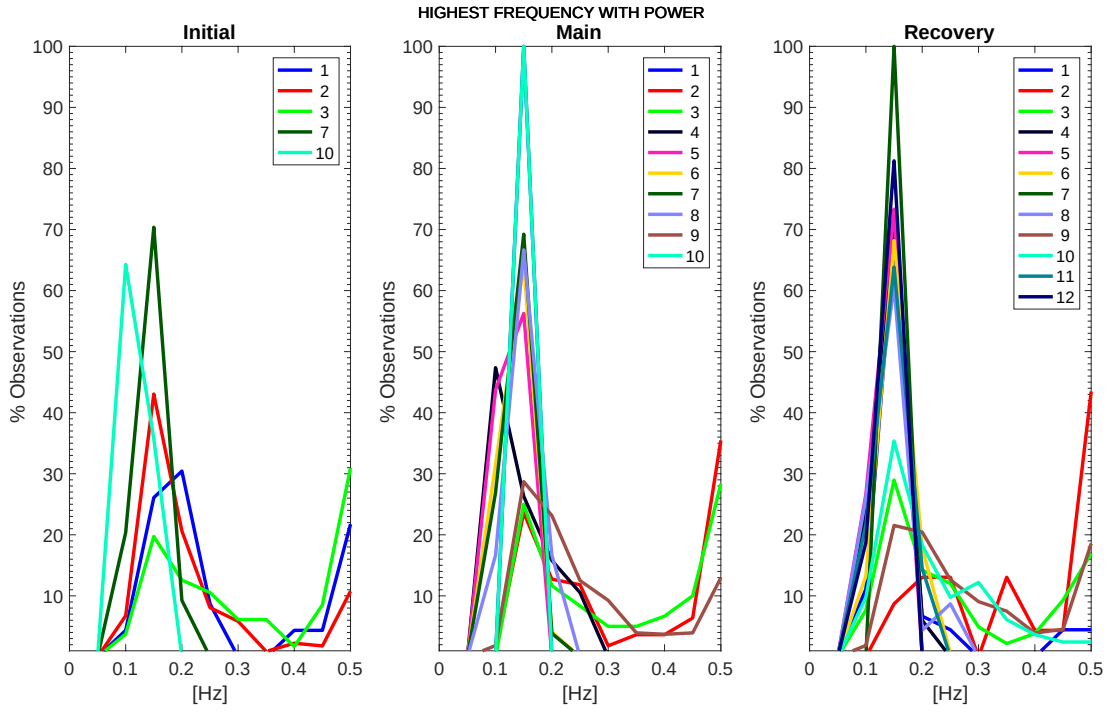

Figure 4.13: Maximum frequency observed separated by storm phase.

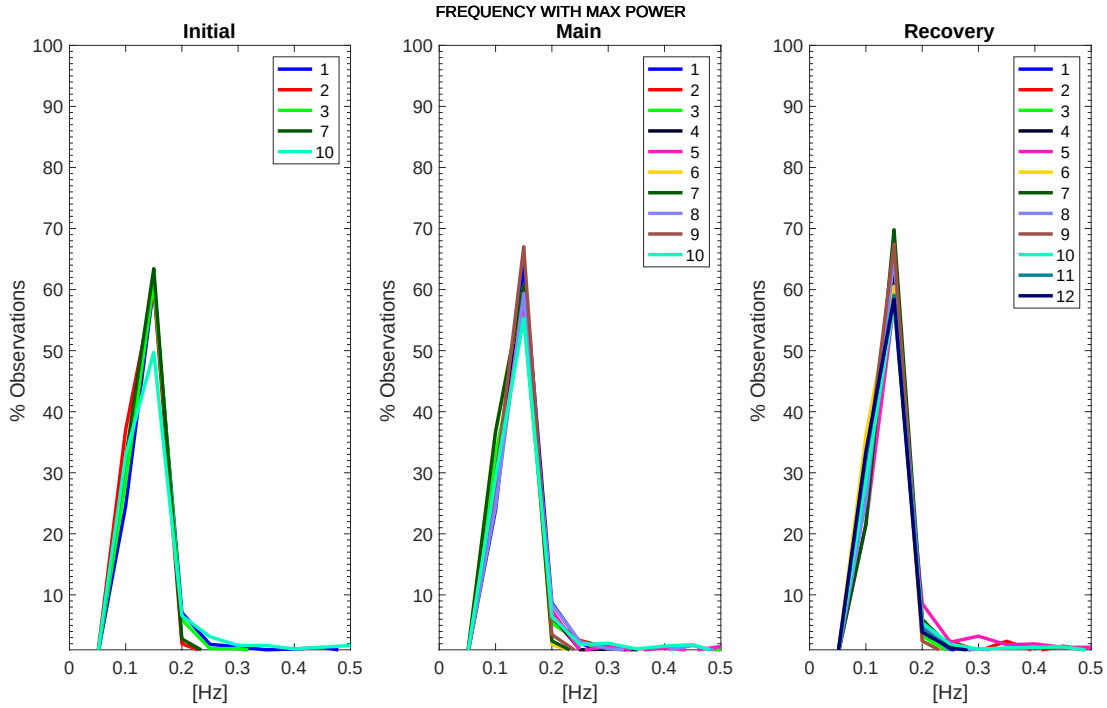

Figure 4.14: Frequency of maximum power separated by storm phase.

4.5 Conclusion

This study has demonstrated the applicability of the methodology described in Chapter II to analyze variability in the SED plume system across multiple storms. It has also has demonstrated the range of variability within the SED plume system and indicated the role of storm phase in ionospheric variability. This limited study should prompt further study in this manner over many more storms to improve the counting statistics, but more importantly improving the possibility to establish correlations between parameters such as Dst, Universal Time and Local Time of storm dynamics, and ion velocity vectors. Additionally, the identification of the plume pocket as a special region may be of importance to the predictability of ionospheric variability since its location structure changes the orientation of gradients from the usual configuration described in the literature [e.g., *Sun et al.*, 2013]. Future work should extend this study to additional storms to establish the existence of more general trends across storms, investigate the role of SED TEC and n_e gradients in addition the SED regions investigated here, and explore additional filter designs to further isolate the contributions of small-scale irregularities from those of larger scale structure in the FFT spectra.

CHAPTER V

CubeSat Mission Design for Space-Based Observation of Small-Scale Irregularities

5.1 Space-Based Observations of Small-Scale Irregularities

There are several ground-based methods for observing ionospheric density structure [*Zou et al.*, 2013]. Ionosondes, radar, and GPS total electron content (TEC) can produce vertical measurements of density, but are limited by the relatively small number of stations and limited coverage areas, especially over the oceans. Ionosondes are further limited to measurements below the height of the ionosphere's maximum electron density—the F peak. Sounding rockets can provide in situ density measurements at high temporal and spatial resolution, but they are limited to localized observations and short flight durations. Space-based measurements of ionospheric density structure allow long duration observations, expand the coverage area, including over the oceans, and allow for unique measurement geometries not possible from the ground, such as horizontal TEC used in constructing vertical density profiles [*Hajj and Romans*, 1998] and topside TEC that measures ionospheric densities above the F Peak [*Yizengaw et al.*, 2005].
Furthermore, small-scale irregularities are especially difficult to detect from ground-based TEC observations. While incoherent scatter radars (ISR) are capable

of detecting them, there are only a small number of such facilities around the world. Consequently, the Rate of Change in TEC Index (ROTI) [*Pi et al.*, 1997] has been used to infer the presence of mid-latitude density irregularities on the order of several kilometers in scale over broad regions. This method assumes that irregularities are steady structures on the timescale in which they drift past the GPS raypath and measurements are made at 30-second intervals. The raypath from a GPS satellite with a 12 hour period moves through the F region at velocities ∼30-400 m s^{-1}, and ion drift velocities at mid-latitudes have been detected by Millstone Hill radar at 200-1000 m s^{-1} [*Sun et al.*, 2013], while the observed density variation is attributed to the drift of stable density structures. Consequently, for low and mid-latitudes, the size of irregularities that have been reliably detected with this method is only a few kilometers. Recently, *Sun et al.* [2013] combined ROTI with an improved filtering algorithm to resolve TEC gradients on the order of a few degrees latitude in scale (∼100 km) from TEC maps of the continental United States. The ROTI calculated from TEC data was then superimposed on the filtered TEC gradients. *Sun et al.* [2013] suggest that regions of high ROTI in the vicinity of larger gradients may be due to the formation of small-scale irregularities under drift-dependent instability criteria. However, since the ROTI can be attributed to either the size or the drift of these structures, some ambiguity remains in confirming the occurrence of small-scale irregularities in the vicinity of SED regions. What is needed is the detection of scintillation causing small-scale irregularities that can separate spatial and temporal variation, such as possible with the SCION multipoint mission.

Variability of the ionosphere's density structure was also investigated by the Dynamic Ionosphere Cubesat Experiment (DICE) twin CubeSat formation. DICE measured density structure using in situ Langmuir probes in an eccentric orbit of 456 x 808 km at 101° inclination. Consequently, density observations were limited

to the local plasma environment. In addition, without spacecraft separation control, DICE did not maintain the close formation necessary for resolving spatial and temporal ambiguity at the ∼1 km scale [*Crowley et al.*, 2011]. DICE's variable separation, eventually separating to >300 km between spacecraft, allowed it to make in situ measurements across a range of spatial scales. However, the variable separation combined with in situ measurements precluded focused and broad observation of small-scale structure across a range of geomagnetic activity. The COSMIC mission launched in 2006 made multipoint occulted and topside GPS TEC measurements, along with measurements of GPS scintillation; however, COSMIC's observations were tens of kilometers and several minutes apart. Unfortunately, since COSMIC was designed for global coverage as an operational mission, its spacecraft also did not maintain the close formation geometry required for continued multipoint observations [*Anthes et al.*, 2008; *Fong et al.*, 2007; *Brahmanandam et al.*, 2012]. SCION seeks to extend the period of irregularity observation for small-scale multipoint observations <5 km, and continue multipoint TEC and scintillation observations through the remainder of the one year mission. This chapter has been published in *Heine et al.* [2015].

5.2 Science Mission Implementation

SCintillation and Ionosphere Occultation NanoSats (SCION) is a CubeSat–based mission specifically designed to make multipoint, GPS TEC and scintillation observations of the ionosphere on the spatial scales associated with communication and navigation system degradation. SCION especially focuses on the mid-latitude ionosphere where small-scale irregularities can form along the boundaries of larger, meso-scale gradients, such as those that form along storm enhanced density (SED) regions [*Foster and Rideout*, 2005]. To do so, SCION takes high-rate (1-50 Hz) TEC and amplitude scintillation measurements using commercially available

dual-frequency GPS receivers onboard two low-Earth-orbit (LEO) CubeSat spacecraft. Combining TEC and scintillation allows SCION to detect and quantify small-scale structure near larger ionospheric gradients. The separation between the spacecraft achieves two simultaneous, independent measurements of TEC per GPS spacecraft in view, that can be used to infer ionospheric electron density structure. Early in the mission, these spacecraft will be in close proximity and gradually separate over the one year mission lifetime, spanning a range of ionospheric spatial scales. The TEC observations are also used to measure vertical density profiles that are important for the quantification of the background large-scale density structure. Meanwhile, the multipoint scintillation measurements help to define edges of scintillating regions and locate regions of small-scale irregularities not directly detected in TEC variations by the two spacecraft. SCION is the first multipoint LEO GPS TEC mission dedicated to investigating the formation and evolution of scintillation causing small-scale density structures at mid-latitudes along the boundaries of SED regions.

5.2.1 Measurement Geometry

SCION's two spacecraft target observations of small-scale ionospheric irregularities $<$5 km in size for at least the first three months of the mission. Observations will be in three measurement geometries: topside, side scanning, and limb occultation, which observe different regions of the ionosphere. Since at any given time, there are GPS satellites in one or more of these measurement geometries, all line-of-sight accesses to the GPS constellation are potentially valid observations. These measurement geometries are shown in Figure 5.1.

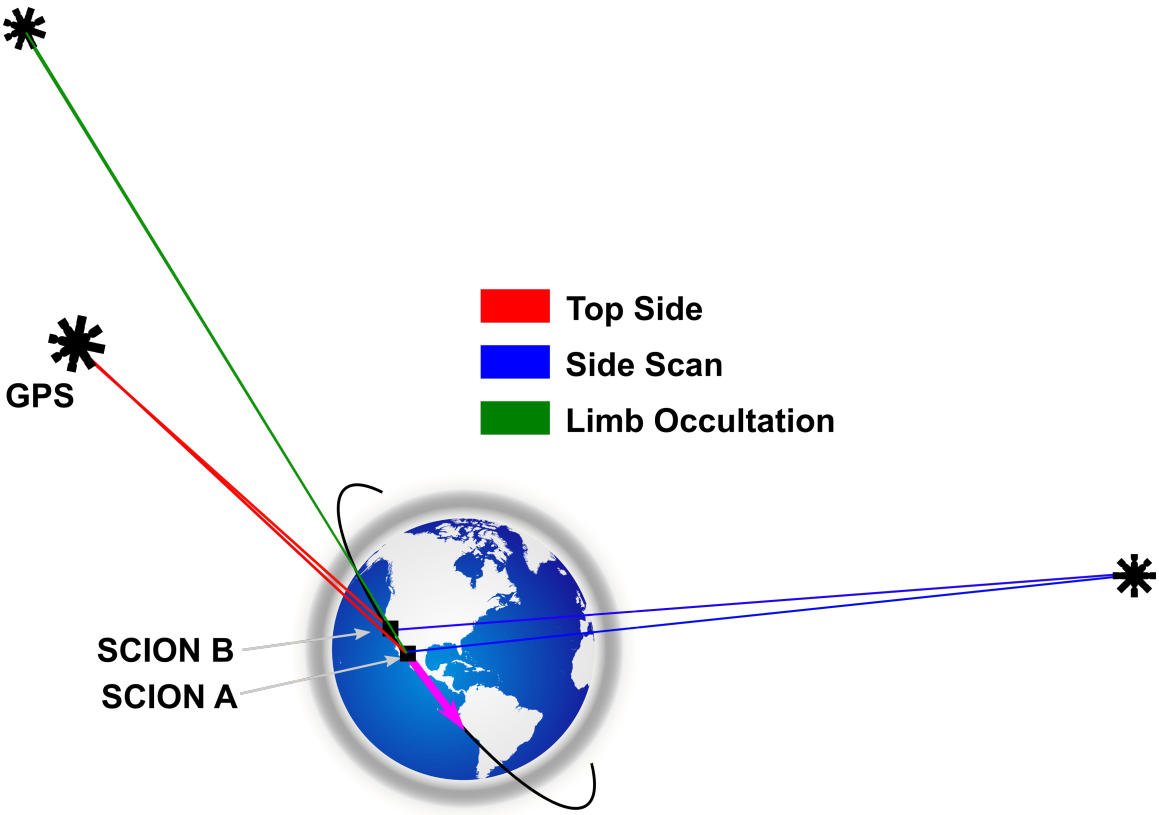

Figure 5.1: The two SCION spacecraft follow the same orbit with their velocity vector indicated in magenta. Measurement Geometries: Rearward limb occultation (green), topside VTEC (red), and side-scan in-situ (blue). (Earth image credit: VectorTemplates.com)

5.2.1.1 Limb Occultation

Rearward looking limb occultations (Figure 5.1, shown in green) produce vertical density profiles of the ionosphere while tracking GPS satellites as they set behind the local horizon [*Hajj and Romans*, 1998] relative to SCION. Setting satellites are preferred for limb occultation over rising satellites because they have already been acquired by the GPS receiver and do not require lose time while acquiring a new signal lock before making measurements, which can take up to ten seconds. The vertical distance between samples in a vertical profile depends on the direction and relative velocity between the GPS satellite and SCION. The relative velocity can then be attributed chiefly to the motion of SCION, since its orbital velocity is much faster than the GPS satellites, which can be considered stationary when estimating the vertical resolution of a limb occultation profile. Analysis shows a GPS satellite setting directly behind SCION sampled at 1 Hz produces ionospheric profiles in $\sim$150 m increments.

5.2.1.2 Topside VTEC

SCION also measures the topside vertical TEC (VTEC) of the ionosphere (Figure 5.1, shown in red). The local VTEC is measured by mapping the slant TEC within a 20° half-angle cone around zenith to the local vertical. The topside region is of special interest because it connects the low altitude dense regions of the ionosphere to the inner edge of the plasmasphere. Topside TEC measurements isolate the density structure of the topside ionosphere and plasmasphere up to the the GPS altitude at 4.2 R_E. Small scale structure at these altitudes are not easily resolved against the dense F region in ground-based TEC measurements, so topside measurements can only be made from spacecraft. This measurement also lends itself to tomographic inversion of the topside density structure by inverting the structure from multiple slant TEC measurements, similar to the structure in Figure 5.2

constructed by *Yizengaw et al.* [2006] from FedSat LEO measurements.

5.2.1.3 Side Scanning Near Field

SCION also measures variations in local ionospheric density near the two SCION spacecraft by observing low-elevation GPS satellites in the cross-track direction (Figure 5.1, shown in blue). In this case, the relative vertical velocity of the GPS satellite is negligible and observations are at nearly constant altitude. One of the challenges in performing ionospheric occultation from a single spacecraft is the double crossing through the ionosphere's F peak for any single raypath between GPS spacecraft and the observing spacecraft. Unlike the neutral atmosphere where density decreases with altitude, the ionosphere has a high density band (the F Region) that peaks around 300 km during geomagnetic quiet times. Consequently, any given raypath during an occultation intersects this dense band at two "pierce points" due to the curvature of the Earth [*Tsybulya*, 2005], and it is nearly impossible to distinguish the TEC contribution of each F peak crossing. With two spacecraft, however, this becomes much easier. Since the SCION spacecraft are several times closer to the near pierce point than the far pierce point, it is reasonable to assume both ray paths effectively observe nearly the same density at the far pierce point. In this case, any observed TEC variations observed in the side scanning geometry can be attributed to the near pierce point. Therefore, in this configuration, SCION measures TEC gradients in the near field, similar to an in-situ measurement at the near pierce point. The left panel of Figure 5.3 shows in situ electron density measurements made by DMSP spacecraft when crossing SED boundaries. SCION's side scanning geometry will be used to produce analogous measurements of the near field density structure.

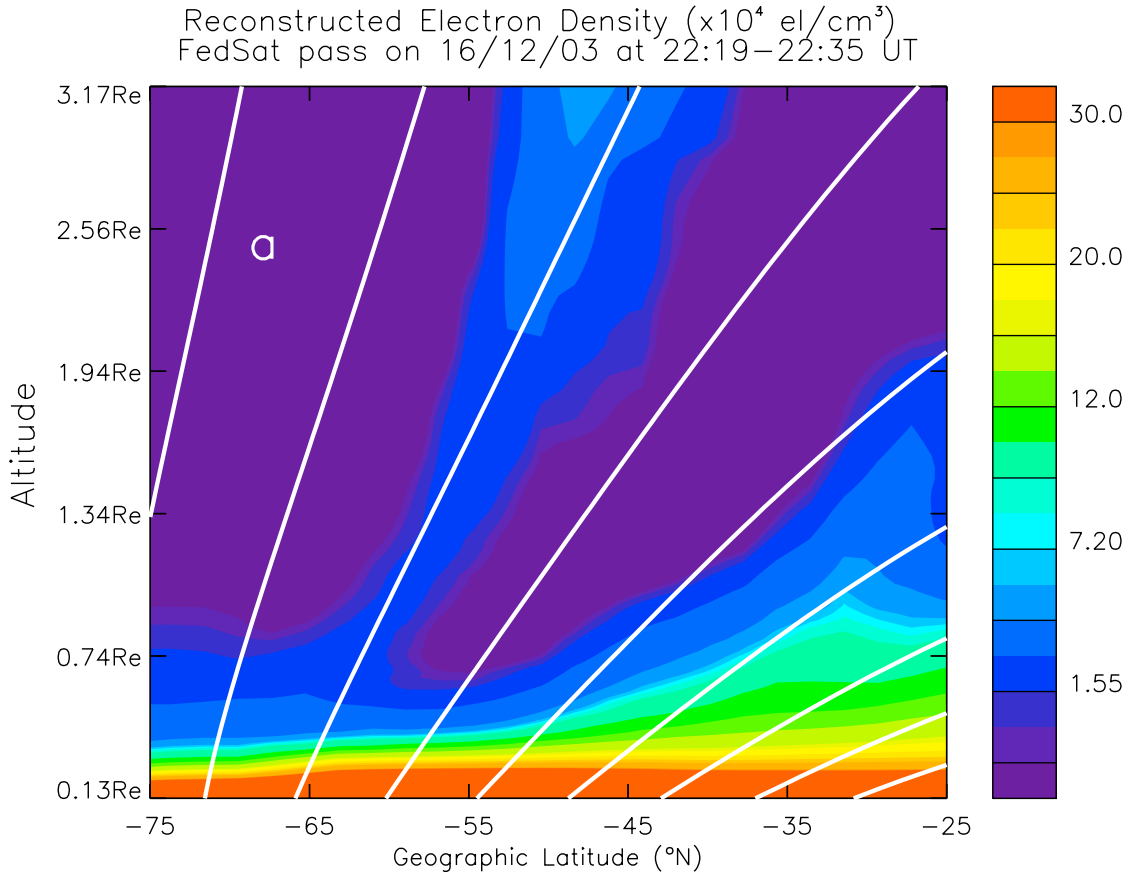

Figure 5.2: Tomographically reconstructed vertical density profiles FedSat slant TEC measurements (adapted from *Yizengaw et al.* [2012]).

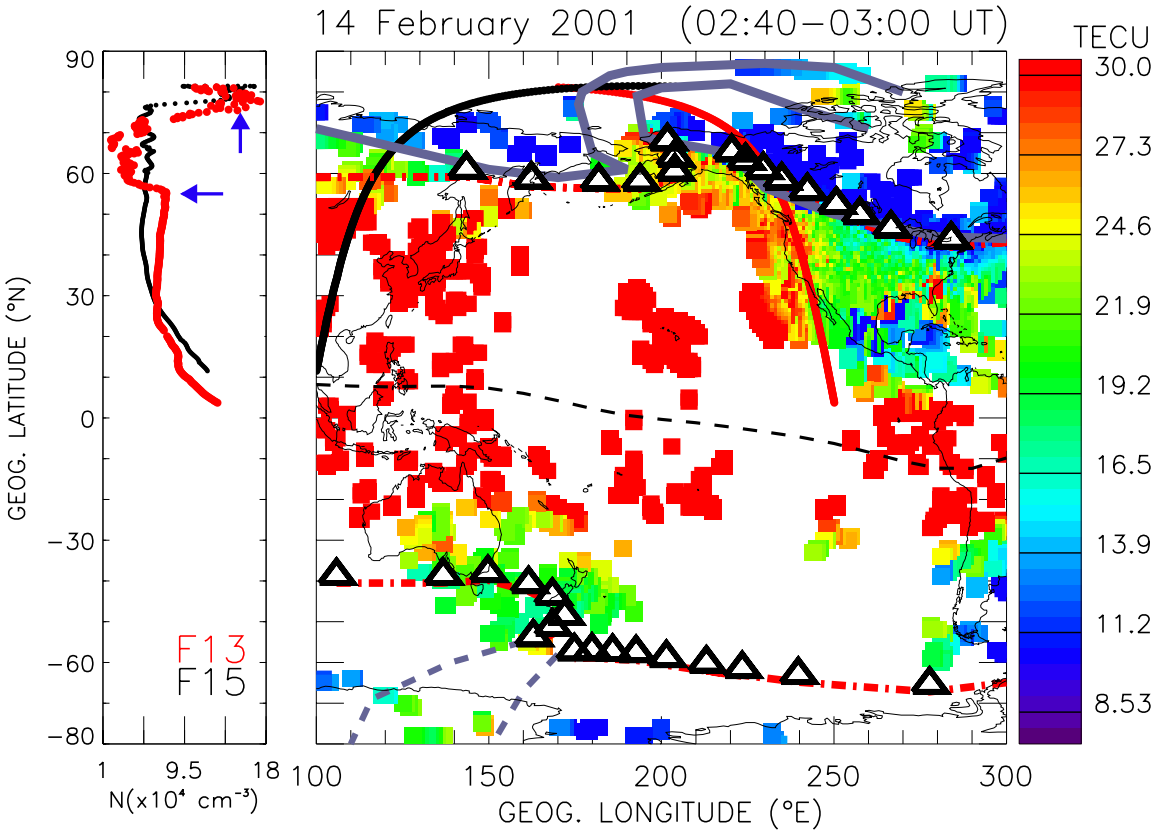

Figure 5.3: Right: GPS TEC map showing a SED plume in the North American sector. The white triangles correspond to the magnetic footprints of the plasmapause as observed by IMAGE EUV. Left: Two in situ density measurements observed by DMSP F-13 and F-15 at ∼870 km altitude [*Yizengaw et al.*, 2008].

5.3 CubeSat Mission Feasibility

Preliminary spacecraft design work for SCION was completed by Space Systems Master of Engineering students as part of the space systems design curriculum of the University of Michigan's Atmospheric, Oceanic, and Space Sciences program. This section outlines the spacecraft and subsystem sizing that demonstrates the feasibility of the SCION mission.

5.3.1 Concept of Operations

SCION's mission objectives are well-suited to the focused and highly cost-effective nature of CubeSat missions. Many of SCION's subsystems benefit from previous CubeSat missions, and SCION itself belongs in a pipeline of CubeSat development at the University of Michigan. SCION consists of two identical CubeSat spacecraft that launch as a secondary payload and are ejected from a Poly PicoSatellite Orbital Deployer (PPOD) at an orbit determined by the specific primary launch vehicle payload, but desired within 500 - 600 km and 40° and 60° inclination as described in Section 5.3.3. The 1U spacecraft each feature two fixed, deployable solar arrays 10 × 10 cm in size, and a deployable tape-measure whip antenna tuned to ∼437 MHz for uplink and downlink communication. The solar arrays and antenna will autonomously deploy no earlier than 30 min after ejection from the PPOD per CubeSat Design Specification Rev 13, [**?**]. The two spacecraft will begin the mission while in contact with one another, and with nearly zero ΔV difference at ejection from the PPOD. They are allowed to drift freely while being gradually separated by aerodynamic forces. The separation rate will be minimized to extend the duration the two spacecraft are able to make observations between 0.2 and 5 km, which is expected to be at least three months from ejection. The spacecraft separation concept is described further in Section 5.3.3.4. SCION uses a "store-and-forward" data delivery system. Science data and housekeeping telemetry

will be downloaded per ground command to a single dedicated ground station in Ann Arbor, Michigan. The minimum success lifetime for the SCION mission is six months, with a goal of one year.

SCION has five operational modes: Safe, Detumble, Deploy, Standby, and Science Operations. The spacecraft are in Safe Mode immediately following ejection from the PPOD, and are returned to that state automatically after an anomalous restart. During Safe Mode, only the flight computer, power system, and communication uplink system (in standby) are active. Detumbling occurs after ejection, actively using coarse attitude sensors and magnetic torquers prior to deployment of the solar arrays and communication antenna. During detumbling, there is a slight battery charging deficit accumulating 5.5% per orbit until the solar arrays are deployed. Detumbling is expected to be accomplished within two orbits. Deployment is identical to Safe Mode, but includes powering the release mechanisms to deploy the solar arrays and communication antenna. Standby Mode is similar to Safe Mode, but requires a command from the ground to initiate (typically out of Safe Mode). It includes uplink and downlink communication and attitude sensor monitoring. Lastly, the Science Operations Mode adds the activation of the GPS receiver science payload, and performs active attitude determination and control.

5.3.2 Science Payload

Each of the two SCION spacecraft will carry either a Novatel OEMV-1DF or a Septentrio AstRx-m GPS receiver. These receivers have lower cost, mass, and a better form factor for CubeSat applications when compared with other dual-frequency receivers that have flown in space, such as the Broad Reach/JPL BlackJack receiver [*Dyrud and Fentzke*, 2011]. The final receiver selection will be determined by ongoing testing. Performance tests were done with an OEMV-2, which is functionally identical to the OEMV-1DF. The OEMV-1DF has a compact

form factor (7.1 × 4.6 cm) that fits well on a conventional 1U CubeSat board stack and, in its single-frequency version, has flight heritage on RAX and RAX-2 [*Arlas and Spangelo*, 2013]. The OEMV-1DF is capable of sampling up to 50 Hz and consumes 1.3 W of power. The AstRx-m, manufactured by Septentrio Satellite Navigation, is a lightweight, small form factor GPS receiver capable of sampling the GPS constellation at up to 50 Hz. The dominant advantage of the AstRx-m is that it only consumes 0.5 W during operation. Further testing will inform the final payload selection from these two receivers.

SCION's GPS antenna configuration is designed to ensure a minimally obstructed view of the GPS constellation and maximize the opportunity for observations without the need for precise attitude determination and control. Each SCION spacecraft will have two dual frequency GPS patch antennas mounted on opposite (+/-X) faces of the CubeSat. Since each antenna has a 100° field of view for both frequencies, the spacecraft will slowly rotate about the Z axis. A baseline rotation rate of 0.3 RPM was chosen because it ensures that a GPS spacecraft crossing the antenna center has at least 60 s within the 3 dB gain peak. This is followed by 48 s where the GPS satellite falls outside of this range before being reacquired via the second antenna. The Novatel OEMV-2 testing showed that individual GPS satellites reacquire L1 lock within 2 s, and L2 in within 8 s. It is likely the receiver is able to maintain lock at elevation angles outside of the 100° 3 dB gain pattern, which would further expand the opportunity for observations. This will be confirmed in future tests, but for the present analyses, observations were limited within a 100° field of view.

5.3.3 Orbit Selection

SCION's orbit should maximize the opportunity for observations of the mid-latitude ionosphere, which is quantified by the frequency of access to the GPS constellation

while SCION is below ±60° latitude. This condition is valid for observing the mid-latitude ionosphere because the distance from SCION to the F-peak during side scanning observations is within ∼6°, latitude or longitude, putting most observations at mid-latitudes (Figure 5.4). There are three additional constraints that inform orbit selection. First, the orbit shall allow a minimum mission lifetime of six months, with a goal of one year while, not exceeding the provisions of *NPR 8715.6A* [2009] which requires deorbit within 25 years of end-of-mission. Second, the orbit should maximize number of daily accesses to the University of Michigan ground station in Ann Arbor. Third, the altitude shall allow observations at the desired spatial scale for at least 90 days. Though the orbits used for this analysis are all circular, circular orbits are not required, and the suitability of eccentric orbits would be similarly analyzed given such a launch opportunity.

5.3.3.1 GPS Constellation Access

The opportunity for observation of the mid-latitude ionosphere depends on the frequency and duration of access to the GPS constellation. While all line-of-sight accesses to the GPS constellation are potentially valid observations within the three measurement geometries of topside, side scanning, and limb occultation, orbits were assessed on the average total daily access time to GPS spacecraft below the SCION local horizon. Since SCION is above the ionosphere's densest altitude, accesses below the local horizon have the best opportunity to observe F region irregularities. To estimate the observation opportunity possible with different orbits, the Systems Toolkit (STK) by Analytic Graphics Inc. was used to compute the cumulative access time to the GPS constellation over a one year time period, shown in Figure 5.5. For this analysis, the spacecraft was assumed to be +Z northward pointing with two 100° beam width antennas, pointing in opposite directions perpendicular to the spin axis, and a rotation rate of 1 RPM. With slower spin rates, access time

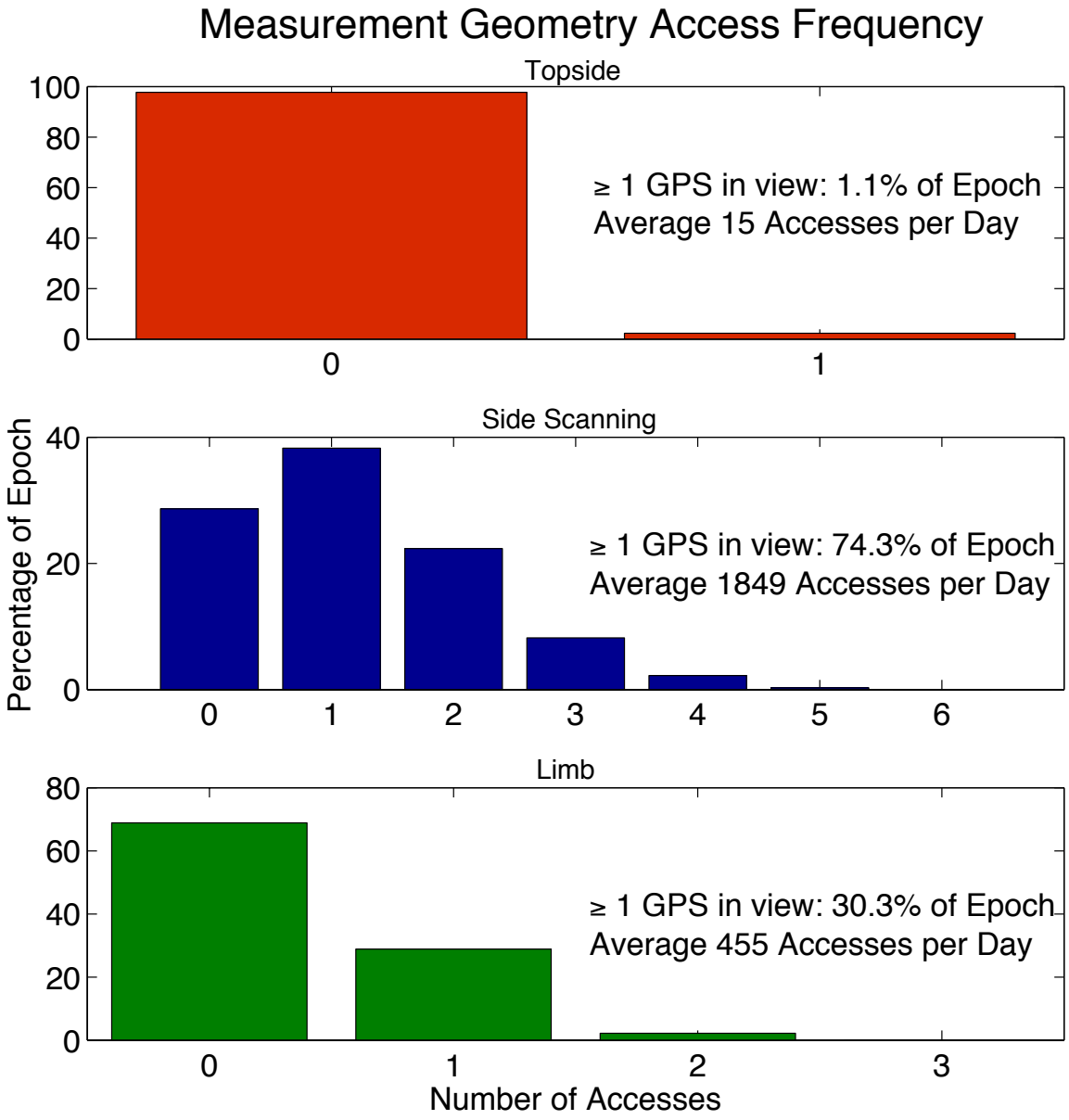

Figure 5.4: Typical number of GPS spacecraft within each of the three measurement geometries over a one-month epoch of mission time.

increases linearly, independent of altitude and inclination. The orbits analyzed were circular inclined orbits from 20° to 80°, and between 400 and 800 km. From Figure 5.5, it is clear that higher orbits provide greater access to the GPS constellation, suggesting that higher orbits allow more GPS satellites into view that would otherwise be obscured by the Earth. Furthermore, mid-latitude inclinations provide more constellation access than low or polar inclinations, since the GPS constellation itself is at 55° inclination. This analysis shows that 40° inclination would provide the greatest GPS access at most orbit altitudes and 60° provides the next best access opportunity up to 650 km. 50° inclination showed less, but comparable average daily GPS access time to 60°. There was also comparable access time at 30°, but with insufficient coverage of the mid-latitudes.

5.3.3.2 Ground Station Access

SCION will be operated from a single ground station at the University of Michigan in Ann Arbor, which is capable of communicating with multiple spacecraft simultaneously (described further in Section 5.3.4.4). More ground stations would be beneficial, but were not included in this study due to cost and use constraints. Total ground station access is a key factor in orbit selection, because SCION produces a large volume of data. Since ground station access is intermittent, SCION will not provide realtime science data; instead, it will store and forward data collected over one or more orbits. Orbit selection is further constrained by the requirement that all of SCION's data be downlinked by the end of the mission. This requirement allows for temporary lags in data transmission, and requires only average ground station access times, rather than placing unnecessarily stringent requirements on day-to-day access, which can vary considerably. Potential SCION orbits were analyzed in STK over one year to determine the average daily contact time for several inclinations and altitudes, for a period of one year. Only circular

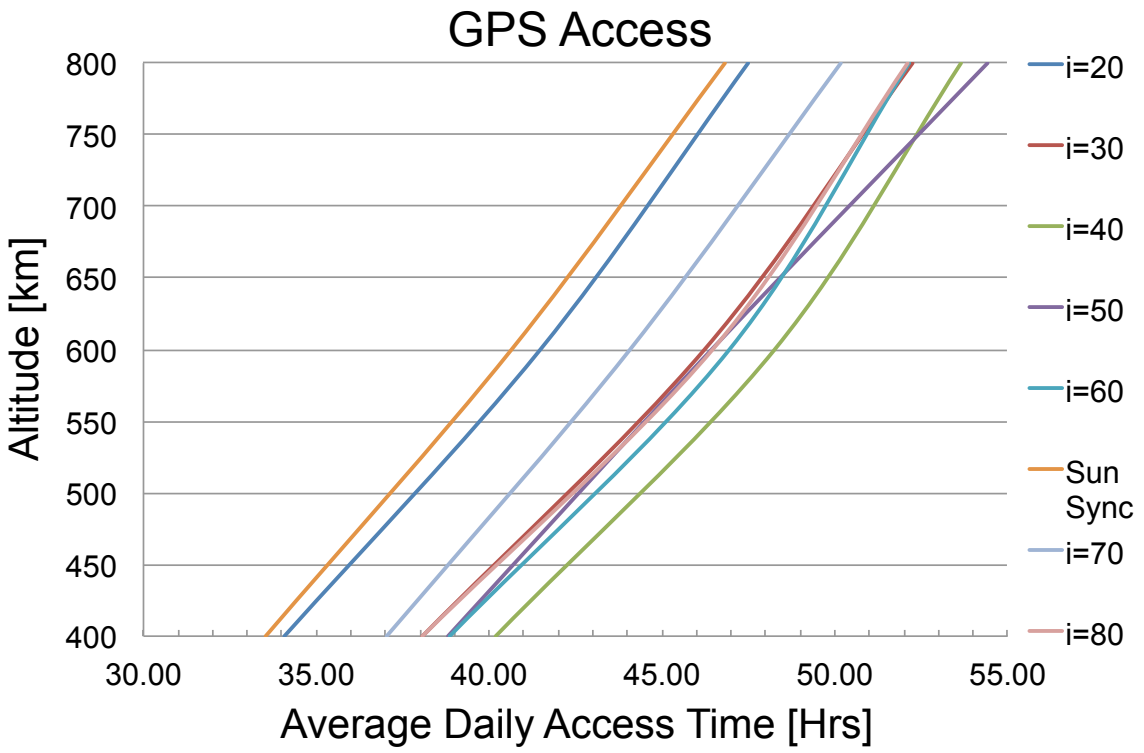

Figure 5.5: One year access time to the GPS constellation below SCION local horizon in one day averages. The accesses were modeled with two 100° FOV antennas, and Z axis rotation at 1 RPM.

orbits were analyzed. Figure 5.6 indicates that inclinations between 40° and 60° provide the greatest average access time for altitudes below 700 km, and inclinations between 50° and 70° above 700 km.

5.3.3.3 Mission Lifetime

The minimum SCION mission lifetime is six months with a desired lifetime of one year. The minimum lifetime of six months, allows for spacecraft checkout, formation separation, an operational duration sufficient to observe several SED events [*Yizengaw et al.*, 2008]. In addition, SCION's total orbital lifetime must be less than twenty-five years from the end of the operational mission. This requirement is a condition of the *CalPoly CubeSat Specification* (Req. 2.4.5) levied on all PPod deployed missions [*Institute*, 2014] and inherited from *NASA Procedural Requirements for Limiting Orbital Debris*, Requirement 56876 [*NPR 8715.6A*, 2009; *NASA-STD-8719.14A*, 2012]. Representative orbits between 400-700 km, and 40° inclination were propagated in STK using the High Precision Orbit Propagator (HPOP) for a 1U CubeSat (1.33 kg) with a 2.2 drag coefficient. The atmospheric density was estimated from the US Naval Research Laboratory MSISE-2000 atmospheric model (valid up to 1000 km), using the predicted solar 10.7 cm radio flux $F_{10.7}$ and $\langle F_{10.7} \rangle_{81\,\mathrm{Day}}$ $[(10)^{-22}\,\mathrm{W\,m^{-2}\,Hz^{-1}}]$ and geomagnetic (Kp and Ap) conditions with a three-hour update rate from the Space Weather Data file by Celestrak and the Analytical Graphics Inc. Center for Space Standards and Innovation. The STK lifetime tool was used to calculate the lifetime of altitudes at 400, 500, 550, 600, 650, and 700 km, with effective drag areas of 0.01 and 0.34 m^2 representing the minimum and maximum possible effective drag areas. The results of this analysis, shown in Figure 5.7, suggest that orbits below 450 km will not meet the six-month lifetime requirement for minimum success, whereas orbits above 600 km will exceed the 25-year limit. These conditions propagated at 40° and 60°

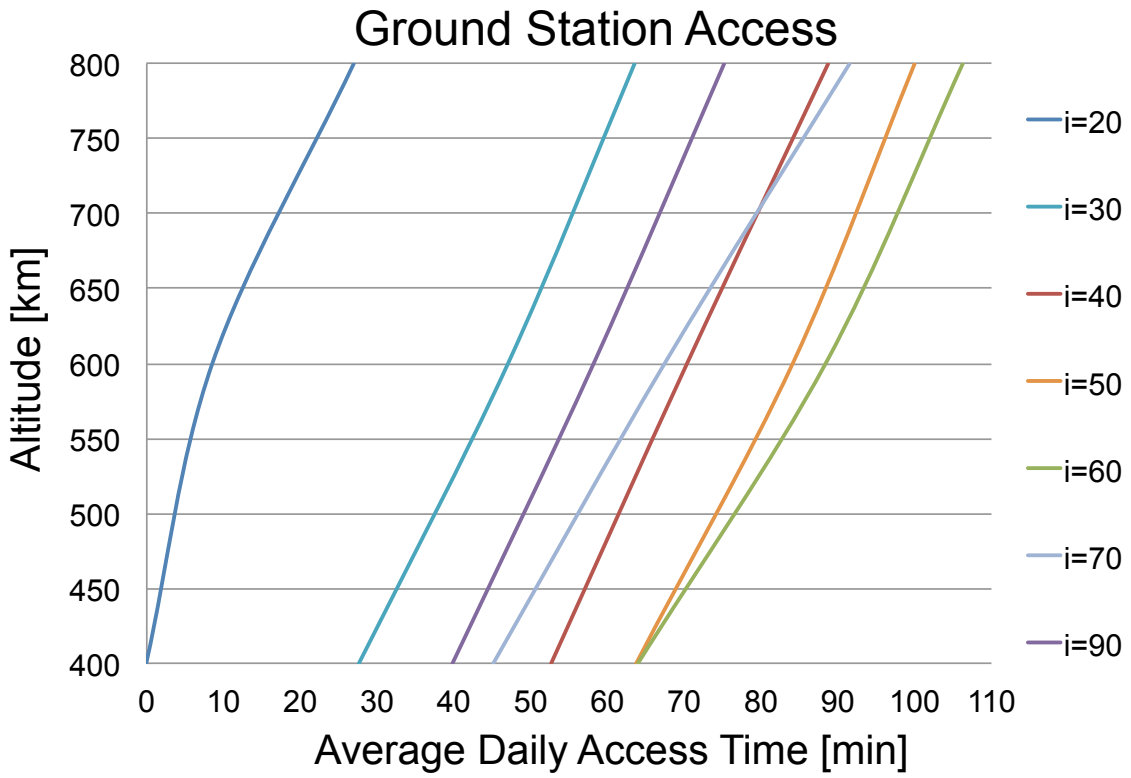

Figure 5.6: One year average daily access time to a ground station in Ann Arbor, Michigan, with near omnidirectional UHF whip antenna and Z axis rotation at 1 RPM.

inclination produced the same result.

5.3.3.4 Spacecraft Separation

Controlled separation between the two SCION spacecraft is one of the greatest challenges of the mission design. Upon deployment, the two SCION spacecraft are allowed to drift freely. Despite both CubeSats' initial deployment into the same orbit and position, there are three primary forces that can act to separate them. Additional forces, such as tides and gravitational variation, act equally on both spacecraft, and are therefore neglected [*Sabol et al.*, 2001]. The three primary forces affecting SCION spacecraft separation are: 1) the plunger springs required between CubeSats deployed from the same PPOD [**?**]; 2) the PPOD main spring that ejects the CubeSats; and 3) differential drag forces acting on the CubeSats depending on their orientation and any surface inconsistencies. Fortunately, the first two forces can be mitigated prior to launch. Per personal correspondence with the CalPoly CubeSat Program, the requirement for separation springs between the two SCION spacecraft can be waived, since they are a single mission. Relieving this requirement also mitigates the potential ΔV source of the PPOD main spring. Since the two SCION spacecraft do not have separation springs, they remain in contact with one another and the main spring acts on them equally as a single mass. The remaining ΔV source is the differential aerodynamic drag. Even though they are intended to be identical in shape, surface, and mass, the two SCION spacecraft may experience slightly different drag forces due to subtle surface inconsistencies or differences in orientation relative to the velocity vector. Initially, this differential drag force is desired to achieve separation, however if the separation rate is too fast, the amount of time spent within a useful range will be too short to achieve the science mission goals.

To address this question, SCION was modeled in STK using the NRLMISE-2000

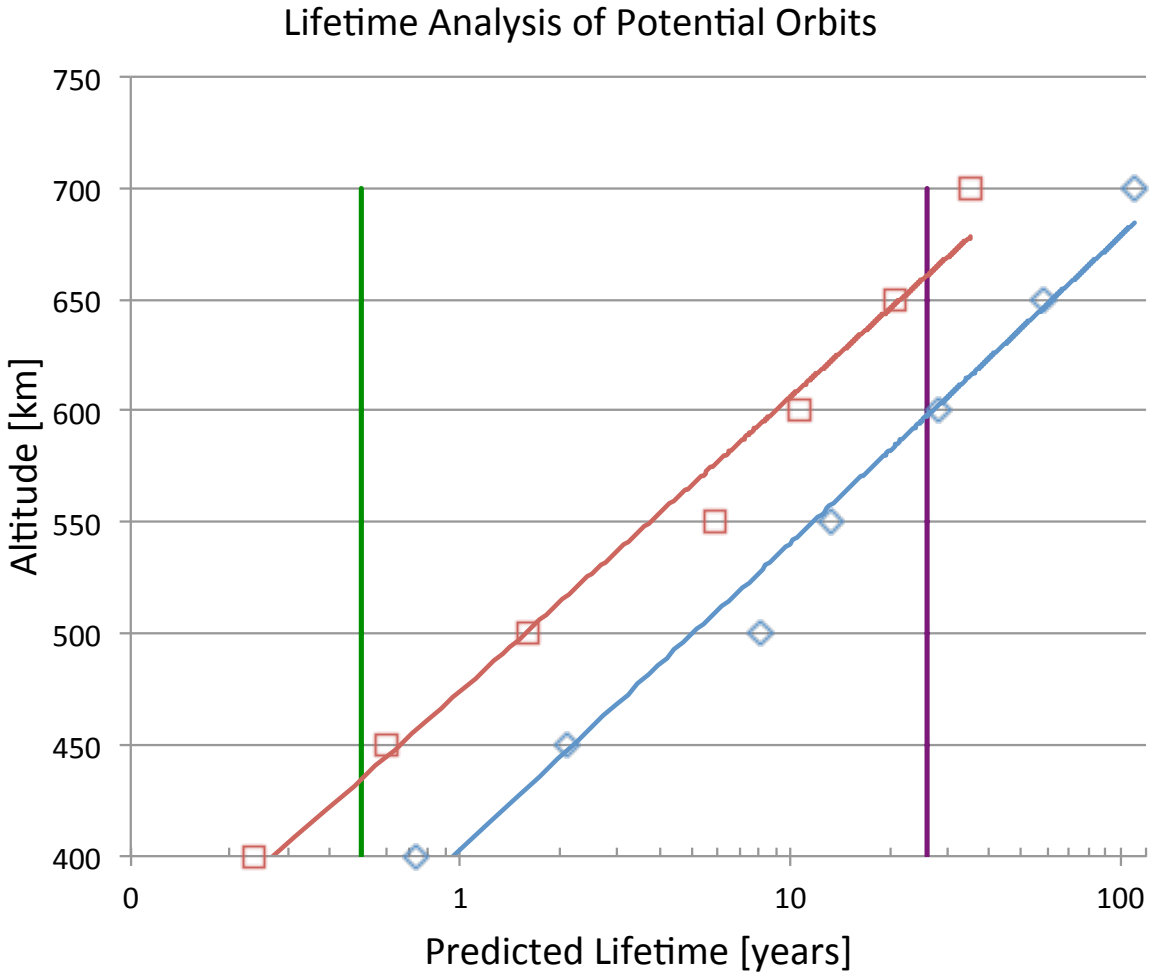

Figure 5.7: Predicted lifetime for SCION at 400-700 km circular, 40° inclined orbits. The red and blue lines indicate effective drag areas 0.010 m^2 and 0.034 m^2respectively. The green and purple vertical lines illustrate the six-year minimum and 25-year maximum lifetime requirements respectively.

atmospheric model for active, moderate, and quiet solar and geomagnetic conditions at altitudes of 500, 550, and 600 km. Active times, defined as having an $F_{10.7}$ and $\langle F_{10.7} \rangle_{81\,\mathrm{Day}}$ of 200 with Kp of 6; moderate times, $F_{10.7}$ and $\langle F_{10.7} \rangle_{81\,\mathrm{Day}}$ of 120 and Kp 3; and quiet times, defined as $F_{10.7}$ and $\langle F_{10.7} \rangle_{81\,\mathrm{Day}}$ of 90 and Kp of 3. These cases represent the extremes and typical conditions observed during the present and previous solar cycle. The two spacecraft were placed at the same point in space, holding the drag coefficient constant at 2.0, with a mass of 1.33 kg, and varying only their drag effective area by 1% from 251 cm^2, the RMS effective area for rotation about SCION's Z axis. The 1% difference in effective area was selected as the upper limit, based on simulations showing that higher effective area differences produced unsatisfactory separation rates. This approximately corresponds to the same area as the edge of an additional exposed 10 cm printed circuit board, or an 8.1° pitch difference between the two spacecraft. The basis of the other assumed parameters will be discussed in a later section. The two spacecraft's positions were propagated using the STK Earth HPOP v8.1.1 propagator for one day, with the NRLMSISE-2000 atmospheric model set with the space environment parameters described above. Figure 5.8 shows the one-day line-of-sight separation between the two spacecraft after one day at quiet, moderate, and active conditions, with a 1% difference in effective drag area. This indicates not only the separation from initially matched positions and velocities, but also the differential ΔV in m day^{-1} that may occur over one day for a given space environment. Figure 5.8 also illustrates that a 50 km increase in altitude roughly halves the one-day separation. Since it is unlikely that any of these space environment conditions would be held constant over days or weeks, the spacecraft were again propagated in STK for 90 days using the same parameters as the one-day simulation, but using the predicted spaceweather conditions for a 2015-2019 epoch (declining phase of the solar cycle) from the Space Weather Data file by Celestrak and the Analytical Graphics Inc. Center for Space

Standards and Innovation. The environment was set to a three-hour update rate. The simulation results for 500, 550, and 600 km show a similar trend for separation distance increasing with altitude. Figure 5.9 shows that the simulated separation between the SCION for 600 km altitude after 90 days is ∼8 km.

These simulations are based on several assumptions about the nature of the aerodynamic drag forces on the spacecraft and the characteristics of the spacecraft themselves. One of the primary assumptions in calculating spacecraft drag is that the drag force is proportional to the cross sectional area. Consequently, under this assumption, the orientation of a cube matters greatly. However, *Hinch* [1988] shows that for low Reynolds number flows, which are applicable here (Re <<1, *Dalgarno and Smith* [1962]), the drag force on a cube in uniform flow is independent of its orientation, and produces no net rotation. This makes intuitive sense, considering the stress tensor acting on a cubic surface is embodied in the drag coefficient, which differs, depending on whether the flow encounters a flat face or a pointed edge on the cube. Consequently, the product of C_d and A_{eff}, and the resulting drag force, remain approximately constant regardless of orientation. While the two SCION spacecraft are essentially cubes, they do have deployable solar panels and potentially other non-ideal surface features that violate this orientation independence. One way to reduce the effect of the non-idealized case is to rotate the two spacecraft along the same axis in near resonance. For two rotating spacecraft, the ratios of the RMS effective area over one period (of a reference spacecraft's rotation rate) remains within 1% if the second spacecraft rotation rate is within ∼3% tolerance (or ± 6 s of the rotation period at 0.3 RPM) of a adjacent resonant mode of the reference spacecraft's rotation rate. At higher resonance modes, the faster/slower relationship is reversed and the RMS effective area ratio for low rotation ratios rapidly exceeds 1%. The rotation's phase showed little or no effect for rotation rates on similar time scales. Figure 5.10 shows the ratio of effective

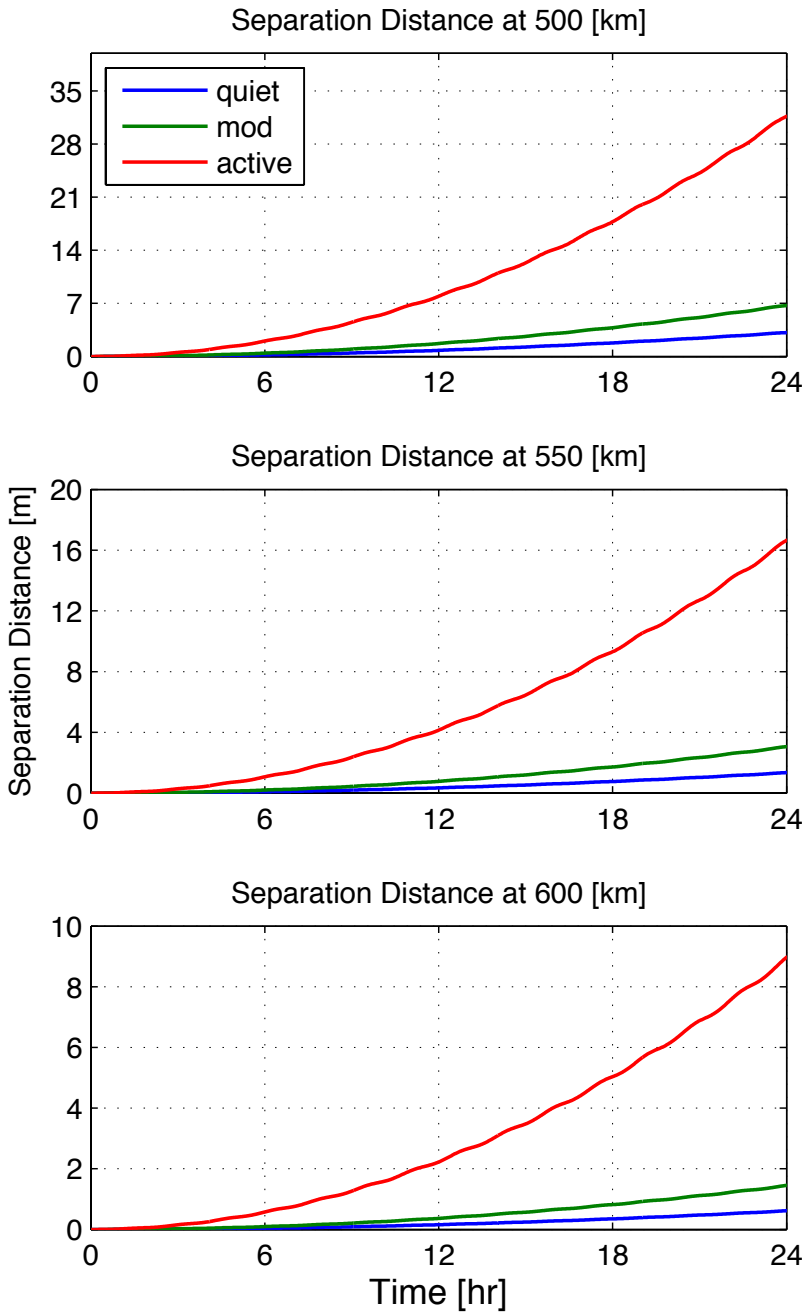

Figure 5.8: One-day separation in meters due to a 1% difference in effective drag area starting from matched positions and velocities. This also implies the one-day ΔV in m day^{-1} resulting from varying solar and geomagnetic conditions.

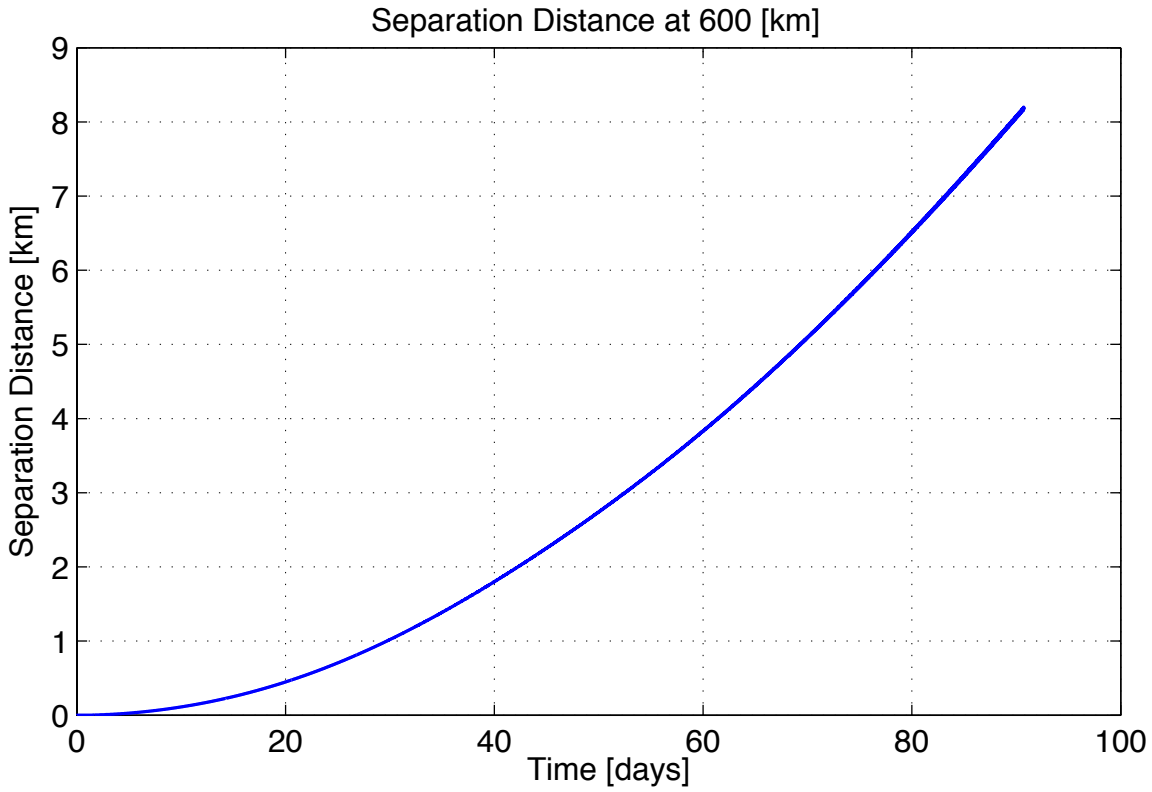

Figure 5.9: 90-day separation in kilometers due to a 1% difference in effective drag area at 600 km altitude.

areas with increasing differential rotation rates. A literature search of magnetorquer-controlled spin rates, including *Sorensen* [1971] and *Damasceno Ferreira and Jaime Da Cruz* [1991], suggests that implemention of spin control at this level does not exceed the capabilities of current CubeSat hardware. Drag coefficients in the LEO regime are roughly bounded between $C_D = 2$ and $C_D = 4$ [*Vallado and Finkleman*, 2008]. A drag coefficient of 2.0 was selected as a best case for the purpose of establishing feasibility. Since the drag force varies linearly with the drag coefficient, the resulting separation also scales linearly with C_D, and so the ∼8 km separation with $C_D = 2$ could be as much as ∼16 km for an extreme worst case $C_D = 4$.

Finally, an analysis was performed to determine acceptable separation distances. SCION's scientific goals are to observe ionospheric density structure on the scale associated with degradation of communication and navigation signals. Figure 5.11 shows the Freznel length spatial scales at relevant distances for LEO spacecraft and ground receivers. The analysis of the spacecraft separation rate shows this is not feasible 100% of the time. However, as the two spacecraft separate, the distance between their two line-of-sight ray paths does meet the desired spatial resolution for some observation angles. To determine how frequent the desired resolution is achieved for various spacecraft separation distances, a single spacecraft was modeled in STK with a 0.3 RPM rotation rate about a northward aligned spacecraft Z axis, and two opposite facing 100° FOV antennas orthogonal to the rotation axis. The spacecraft was propagated for one day in one-second increments, and access times to the GPS constellation were obtained. The access data was first filtered for elevation angles below the local horizon to select limb occulting geometries, and the spacing between the ray paths of each spacecraft was computed for each reported access azimuthal angle, ϕ. The spacing, ρ, represents the multipoint spatial resolution as defined in Figure 5.12. The ray path spacings were divided into fifty bins between

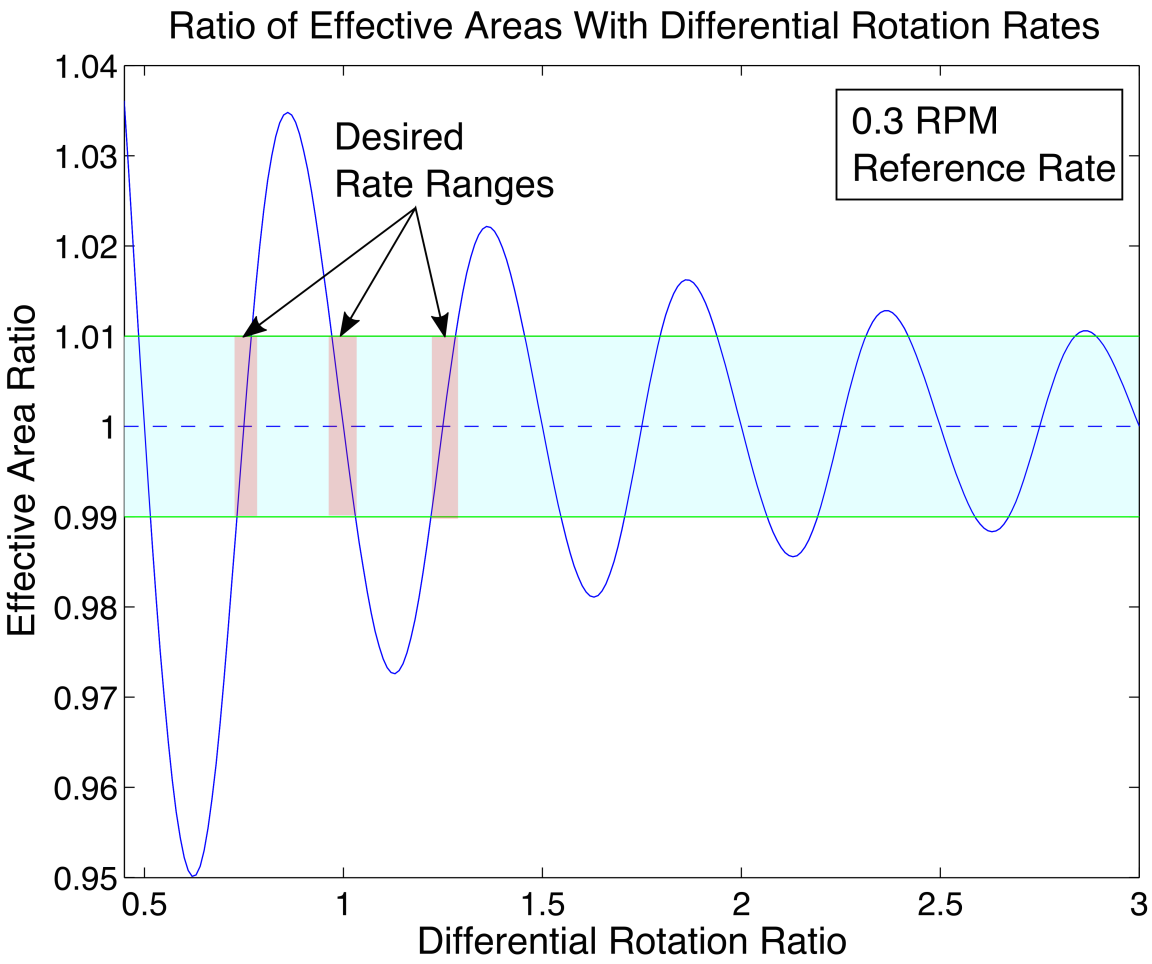

Figure 5.10: Ratio of effective drag areas for spacecraft rotation rates relative to the first spacecraft's rotation rate. The pink boxes show acceptable rotation rate ratios that do not impair the GPS receiver's ability acquire and maintain lock with a given GPS spacecraft.

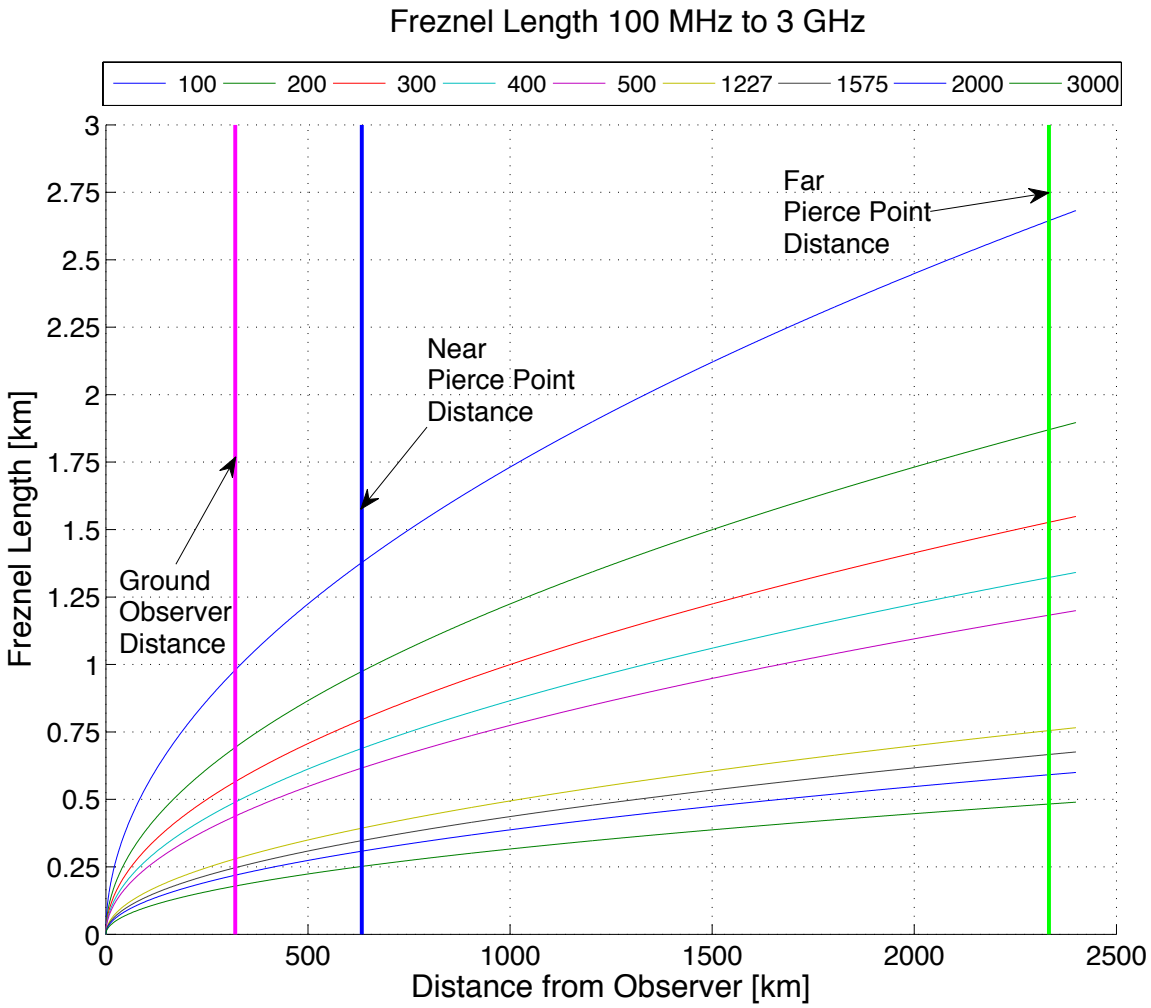

Figure 5.11: The range of Freznel length spatial scales observed by SCION and from the ground over a range of typical communication and navigation frequencies. The observation distance from the two F region pierce points, 600-2500 km, is much greater than that of a typical ground observer, 300 km. Accordingly, SCION does not experience scintillation while observing density structures that produce radio scintillation on the ground.

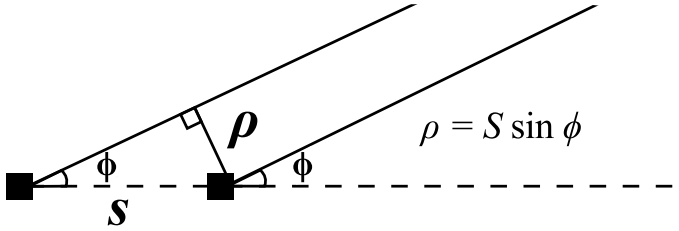

Figure 5.12: Schematic of the definition of multipoint spatial resolution,ρ, for varying spacecraft separation distances, S, given the azimuth angle, ϕ, in the local vertical, local horizontal reference frame.

0-20 km of spacecraft separation. Figure 5.13 shows the results of this analysis as the percentage of time SCION achieves the desired spatial resolution with increasing spacecraft separation. The analysis was also performed for 40°, 55°, and 60° inclinations, and right ascension of the ascending node (RAAN) offsets of 0°, 15°, and 30°. This revealed that the RAAN offset of the orbital plane relative to the principle GPS orbital planes was a significant factor. In fact, it demonstrated that the most frequent opportunities for observation at the desired scale occurred when SCION was in phase (the same RAAN) as one of the GPS orbital planes. This suggests that mission performance is affected by the launch's time of day. Comparing inclinations with equal RAAN, the greatest number of observation opportunities occurred when matching the GPS constellation's 55° inclination. Most importantly, this analysis shows that 1 km resolution is attainable for 20% of observations when the spacecraft are separated by 5 km, and up to 12% when the separation is 20 km. This fits well within the predicted spacecraft separation rate for 90 days.

Given the constraints on lifetime, the maximum possible altitude for SCION is 600 km. In order to achieve the minimum lifetime, its altitude must be above 450 km. For orbits below 700 km, inclinations between 40° and 60° provide the greatest average daily access time to both the GPS constellation and the Ann Arbor ground station. Finally, higher orbits and alignment with the one of the GPS orbital planes (55°, 0° offset from GPS RAAN) provided longer durations with observations at the desired spatial scales. A trade study based on these metrics concluded that while orbits of 40° - 60° and 450 - 600 km are within the acceptable range, higher altitudes are preferred first, and then higher inclinations up to 60°. The ideal orbit for SCION is 600 km, 55° inclination, and with the RAAN initially aligned with the GPS constellation, suggesting a preference for the launch time of day.

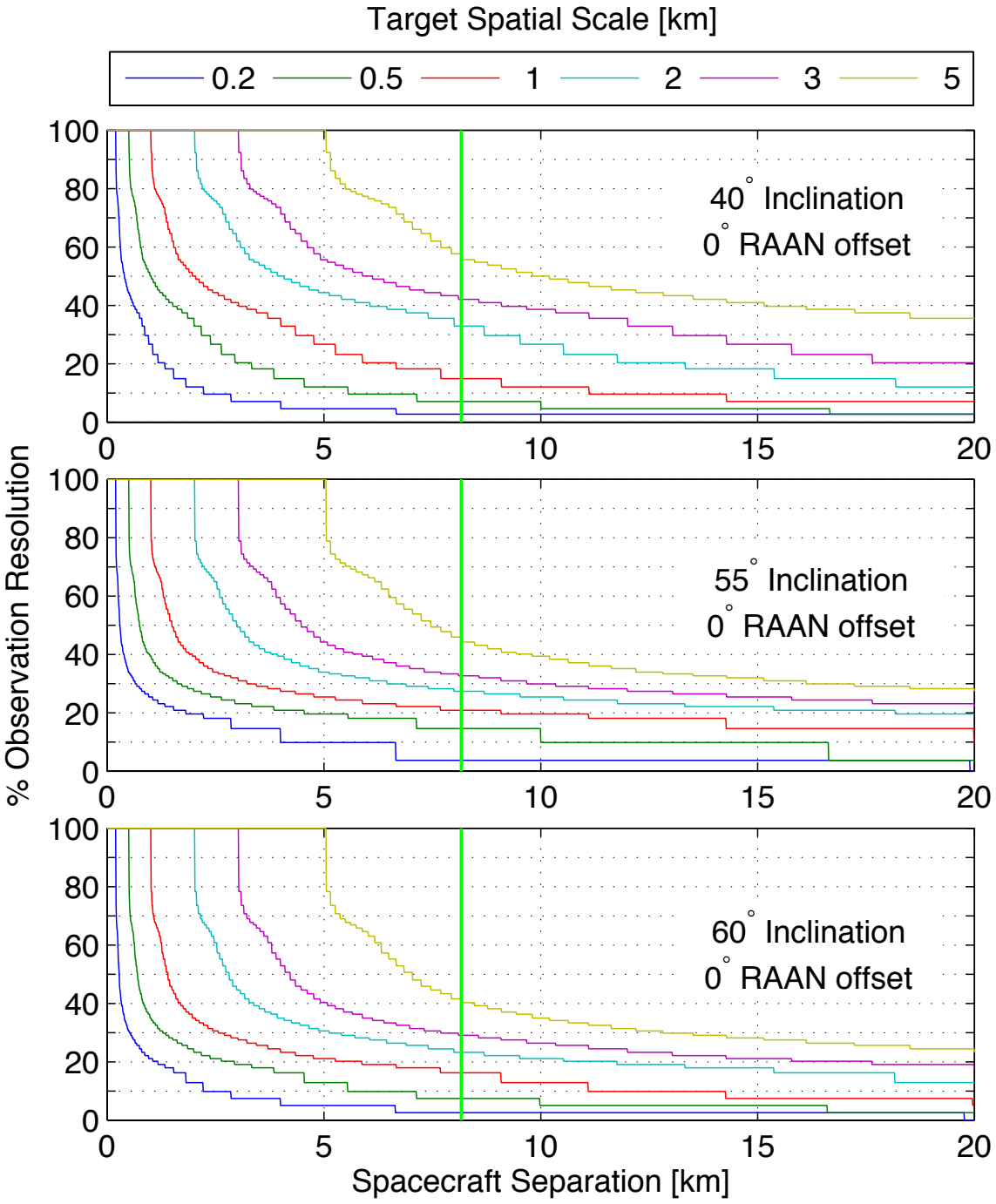

Figure 5.13: Percentage of observations within the target spatial resolution for spacecraft separations of 0-20 km. The orbital planes' RAAN are aligned with one of the GPS orbital planes (130°), and at inclinations of 40° (top), 55° (middle, matched to GPS inclination), and 60° (bottom). The vertical green line is the predicted separation distance at 90 days.

5.3.4 Subsystem Overview

5.3.4.1 Spacecraft Structure

Each SCION spacecraft is built as a 1U (10 × 10 × 10 cm) structure, designed as a lightweight skeletonized aluminum structure similar to that used for CADRE and MCubed-2, allowing for easy insertion and removal of individual component modules and circuit boards. The structure will be made from Al 7075 aluminum with a hard anodized surface finish—as required by the CubeSat Design Specification, Rev. 13 [*Institute*, 2014]. Figure 5.14 shows the packaging and placement of key components and circuit boards within the SCION structure. In this configuration, there are at least 3-4 mm gaps between components. Two deployable solar arrays will unfold from opposite faces of the structure, using spring-loaded hinges. The panels are fully deployed 135° from their initial stowed position. A dual-frequency GPS patch antenna will be placed on each of the +/- X faces of the spacecraft pointed along the solar panel hinge axes to provide a minimally obstructed view of the GPS constellation, as shown in Figure 5.15.

5.3.4.2 Power

The power system consists of two serial 3.6V, 2.9 A hr Lithium-ion secondary batteries for a spacecraft V-batt bus voltage of 7.2 V regulated to 3.3 and 5 V lines. Power will be generated using deployable and body-mounted solar cells. The solar cells will be SpectroLab XTJ cells with beginning-of-life efficiency of 29.5% and degradation to an expected end-of-life efficiency of 26.1%, based on the anticipated radiation environment for SCION's potential orbits. Lifecycle power generation was estimated using STK to determine the illumination and solar incidence angle for each cell, given the ranges of season, orbit, orientation, and rotation rates expected during the mission. The analysis shows that this power generation system is able to

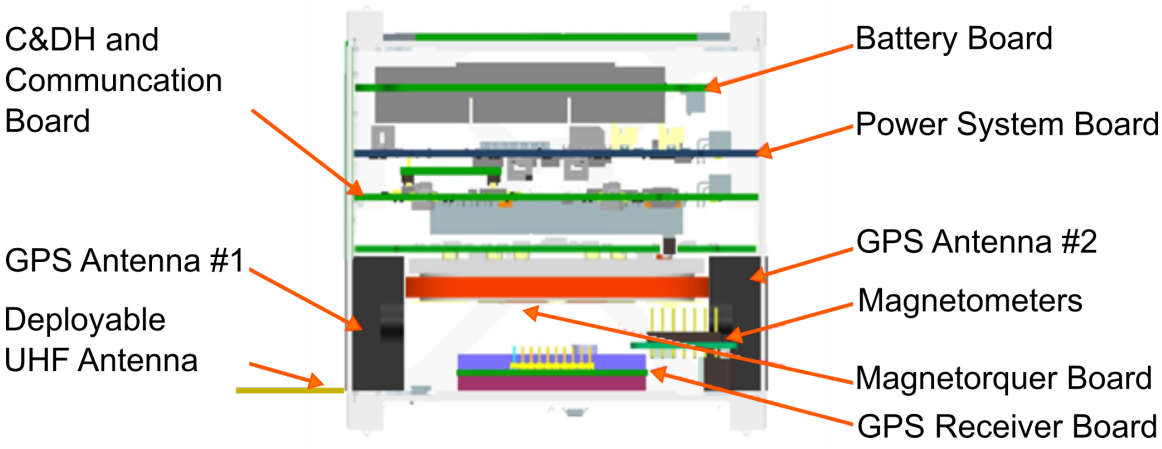

Figure 5.14: Cut out showing packaging and placement of subsystem components within the SCION structure.

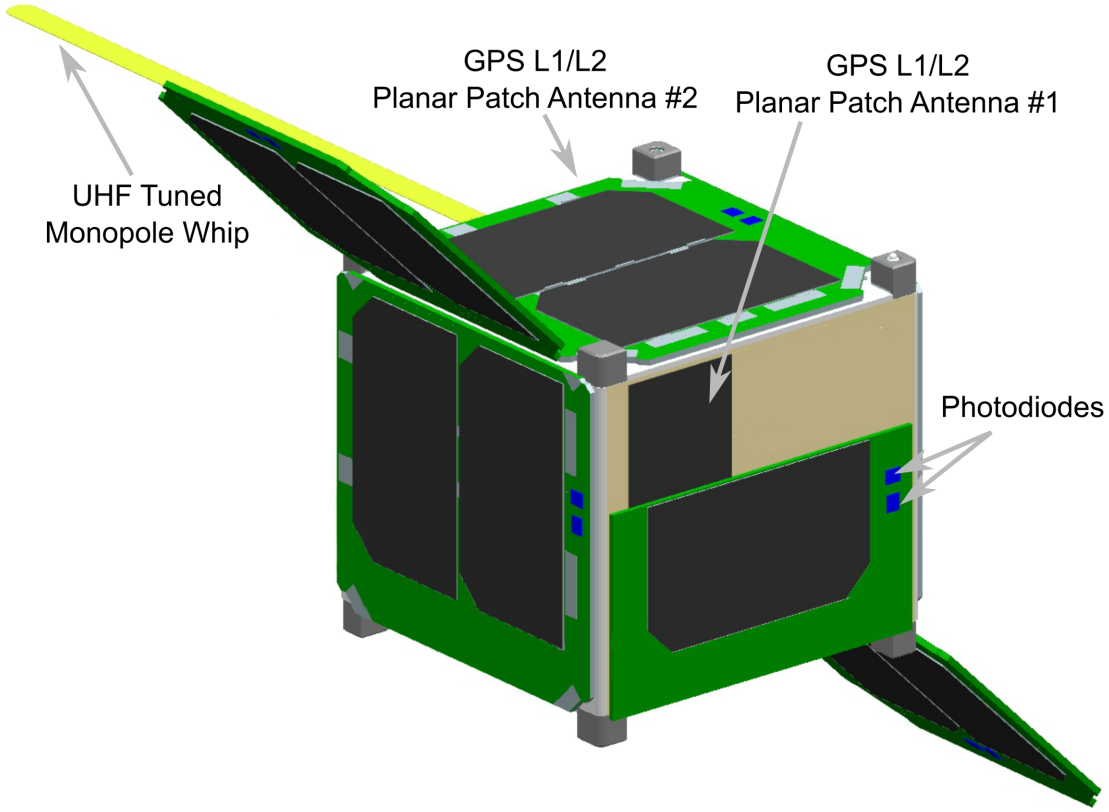

Figure 5.15: SCION with fully deployed panels at 135°, deployed UHF monopole antenna, and relative placement of GPS patch antennas.

provide 9.15 W in sunlight, with deployed solar panels of sufficient margin to recharge batteries during the maximum power consumption of 3.06 W in the Science Operations Mode. Prior to solar panel deployment, the body mounted solar panels produce 3.64 W, which is sufficient to fully recharge batteries in all modes except during detumbling. During detumbling, the batteries accumulate a 5.5% depth-of-discharge (DOD) per orbit that is not replenished. Since detumbling is expected to be complete within two orbits, the batteries experience an 11% DOD for one cycle early in the mission. After solar panel deployment, the maximum operational (DOD) occurs during the longest predicted eclipse, which is 8.6% in the Science Operations Mode. Table 5.1 summarizes the SCION power modes.

Table 5.1: Summary of power resources during each mission mode, Power, Margin, and Battery Depth of Discharge (DOD). Margin refers to the energy available for battery charging. During detumbling, the batteries accumulate a 5.5% DOD per orbit prior to solar panel deployment.

	Mission Modes				
	Safe	Detumble	Deployment	Standby	Science Ops
Power [W]	0.81	1.96	0.83	1.48	3.06
Margin [W Hr]	2.43	0.58	2.4	7.01	4.47
DOD	2.30%	5.50%	2.30%	4.20%	8.60%

5.3.4.3 Command and Data Handling (CDH)

SCION's CDH board is a custom design based on similar CDH boards developed for the CADRE and FTS missions [*Wloszek et al.*, 2013], and is heavily based on experience and flight heritage gained from the M-Cubed, RAX-1, and RAX-2 missions. The motherboard runs an embedded Linux kernel, and its core is a STAMP9G20 computer module containing an Atmel ARM9 processor. The CDH board's software will manage data collection, mode changes, and spacecraft functions, including communication protocols.

SCION's CDH subsystem responsibilities are listed in Table 5.2.

Table 5.2: CDH Subsystem Responsibilities.

Data Collection:	Collection of data from the attitude determination sensors, the GPS science payload, and health and status sensors
Timekeeping:	Onboard clock and command synchronization
Data Management:	Storing, filtering, and compressing data for downlink
Attitude Control:	Gathering attitude sensor information and running the attitude control algorithm
Comm. Management:	Assembling health beacon and downlink packets; interpreting and executing ground station commands

The flight software runs on the STAMP9G20's SDRAM flash storage, which is partitioned to mitigate single event effects. If one kernel is corrupted, secondary or tertiary copies are used. After flashing all kernels for flight, the software team ensures that the kernels have the same CRC32 checksum. Thereafter, the CRC32 checksum is stored in the bootloader's (U-Boot) environment (env1, env2). Linux is unable to write to the kernel partitions, so any CRC32 error is due to a flash error, such as a bit flip. If anomalous behavior is suspected during flight, a reboot command is initiated from the ground. On boot, if the first kernel does not match, U-Boot selects the second, if not that, it selects the third. If the third does not match either, U-Boot tries to boot from third regardless. It is possible for the U-Boot process to become corrupted, since it resides on the same NAND chips as the kernels. However, there are two U-Boot environment partitions that are selected though the NAND chips' native error correction code, which provides some redundancy against U-Boot corruption. SCION also uses three SDRAM storage banks with a veto error correction scheme. If one of the banks does not match the checksum of the other two, it is assumed the data on that bank has been corrupted, and data from the other two are used for the next downlink. The corrupted bank is

then overwritten.

5.3.4.4 Communication

Each SCION spacecraft communicates directly with a single, dedicated UHF ground station at 42.29° N, -83.71° E, in Ann Arbor, Michigan. This ground station has been used successfully for previous CubeSat missions. It is half-duplex, meaning it can either transmit or receive, and can do so with any number of spacecraft, provided their communication channels do not overlap, they fit within the 432-440 MHz band, and are not separated by more than 15° in the ground station's field of view (∼160 km separation at 600 km altitude). The data downlink is initiated and commanded from the ground. Science data is combined with basic housekeeping data consisting of currents, voltages, and temperatures (IVT) on the various subsystems, and onboard data compression is implemented to reduce the size of the downlinked data package.

Once data are received from SCION at the ground station, it is compiled into the Receiver Independent Exchange (RINEX) 2.11 geodetic data format. RINEX is not a compact format, and therefore producing and transmitting a complete RINEX file from SCION file is prohibitive. Fortunately, much of the data required to create a RINEX file (for example, GPS ephemerides) are available on the ground and do not require information from the receiver itself. Consequently, SCION will only downlink the minimum observables required to reconstruct a RINEX file on the ground. Even still, the large data volume generated by the GPS receiver presents one of the greatest challenges of the SCION mission design. Analysis of access to the GPS constellation from a single SCION spacecraft shows that the maximum number of GPS spacecraft in view at any given point of the SCION mission is ten. Sampling all ten GPS satellites at a peak rate of 50 Hz produces 1.2 GB of data per day, whereas at 1 Hz, the data volume drops to 26.8 MB per day. Onboard 1:4 data

compression using tar+bzip2 reduces this volume, but the high sample rate data volume still exceeds the present capabilities of most CubeSat radios. Assuming a circular orbit at 600 km altitude, 40° inclination, SCION will make on average six ground station contacts per day, each 11 min in duration, over the course of a year. Based on these assumptions, Table 5.3 summarizes the data volume and downlink rate required for three sample rates.

Communication link analysis found that a UHF downlink is insufficient to transmit all data generated at the desired 50 Hz cadence. However at a sample rate of 5 Hz, the returned data volume is feasible using a the AstroDev Lithium UHF radio capable of transmitting at 76,800 bps and closing the link with 3.65 dB margin using a single UHF-tuned monopole antenna.

Fortunately, it is not necessary to transmit data from all measurement geometries at the same rate. For instance, data from GPS satellites that fall within the field of view of the side-scanning geometry should be included in the downlink at as high a rate as possible, whereas data from the limb occultation geometry can be much lower at 0.1 Hz. The advantage of this approach is that the receiver can sample all geometries at its peak rate, but onboard filtering algorithms can determine at which rate different observations are added to the downlinked data package. To quantify this, an effective data rate was calculated as the weighted average of the sample rates for each of the three measurement geometries and STK was used to determine the typical number of GPS satellites in the FOV of those geometries over a

Table 5.3: Required downlink rate for zero backlog given GPS sample rate, including housekeeping data, assuming 1:4 compression.

Sample Rate	Per day	Required Rate
5 Hz	125 MB	75.2 kbps
20 Hz	493 MB	296.5 kbps
50 Hz	1,230 MB	739.3 kbps

one-month epoch (Figure 5.4).

Table 5.3 demonstrates that the effective sample rate must be below 5 Hz to achieve the requirement of zero data backlog over the mission lifetime. In actuality, the true rate is closer to 4.6 Hz, to allow a 10% downlink rate margin. Table 5.4 shows an example scenario that uses this technique to achieve a 5 Hz effective sample rate while reporting high rate data when it is useful.

5.3.4.5 Attitude Determination and Control (ADCS)

SCION does not have strict pointing requirements, since the GPS and communication antennas can function in almost any orientation. However, it does require a controlled rotation rate. Therefore, the design drivers for the ADCS system are to detumble after PPOD deployment, and to control spacecraft rotation. Controlled rotation is crucial to SCION, and accomplishes two things. First, it sweeps the GPS antennas slow enough to acquire a fix on both frequencies and make observations. Second, it supports the passive spacecraft separation concept described in Section 5.3.3.4. To accomplish this, SCION is equipped with a magnetorquer board similar to that shown in Figure 5.16 containing an air core magnetorquer and two solid-core magnetic torque rods. Small magnetometers and photo-diodes will provide sufficient attitude knowledge of coarse alignment relative to the local magnetic field and rotation rate respectively. The solar cells will also

Table 5.4: Typical number of satellites in each measurement geometry at any given time, along with their respective sample rates and spatial resolution.

	Returned Rate	# GPS in View	Spatial Resolution
Topside	20 Hz	0.2	0.35 km
Sidescan	35.7 Hz	1.2	0.20 km
Limb	0.1 Hz	0.3	1.50 km

provide additional coarse attitude information.

The ADCS concept of operations uses the magnetorquers after deployment to detumble the spacecraft to a coarse alignment of the +Z axis with the Earth's magnetic field. It is expected that it will take approximately two orbits to achieve magnetic alignment. Once detumbling is accomplished, the magnetorquer board will achieve an initial +Z alignment with the Earth's magnetic field at the equator (northward). The magnetorquer board will then be put into a standby state that only actuates as necessary to maintain the northward +Z alignment. A software control loop running on a dedicated FPGA will drive the magnetic torque rods to achieve the desired rotation rate about the spacecraft +Z axis. To produce this rotation, the magnetic torque rods will actuate when the +Z axis is oblique to the magnetic field, which occurs at higher magnetic latitudes. For example, at 40° geomagnetic latitude, the magnetic inclination, or dip angle, is 55-68°, depending on longitude. Since the spacecraft orientation is aligned with the equatorial magnetic field, as it nears high latitudes, the magnetic field is 90-108° relative to the spacecraft +Z axis. The magnetic torque rods along the X and Y axes are properly aligned to produce rotation about the +Z axis. The FPGA controller actuates the magnetic torque rods to spin the spacecraft to a baseline spin rate of ∼0.3 RPM, though the spin rate can be updated during the mission.

ADCS sizing considered disturbance torques from aerodynamic, solar pressure, residual spacecraft magnetic dipole, and gravity gradient forces with the following assumptions: The worst-case aerodynamic and solar pressure centers of pressure were assumed to be centered on one of the deployed solar panels with a moment arm of 12.1 cm. The worst-case residual dipole was assumed from Springmann et al., 2010 as 0.01 A m^2 and Earth's magnetic field at was taken as 45,294 nT from the International Geomagnetic Reference Field (IGRF), which is the maximum for 60° geodetic latitude and 500 km altitude. Lastly, the worst case gravity gradient

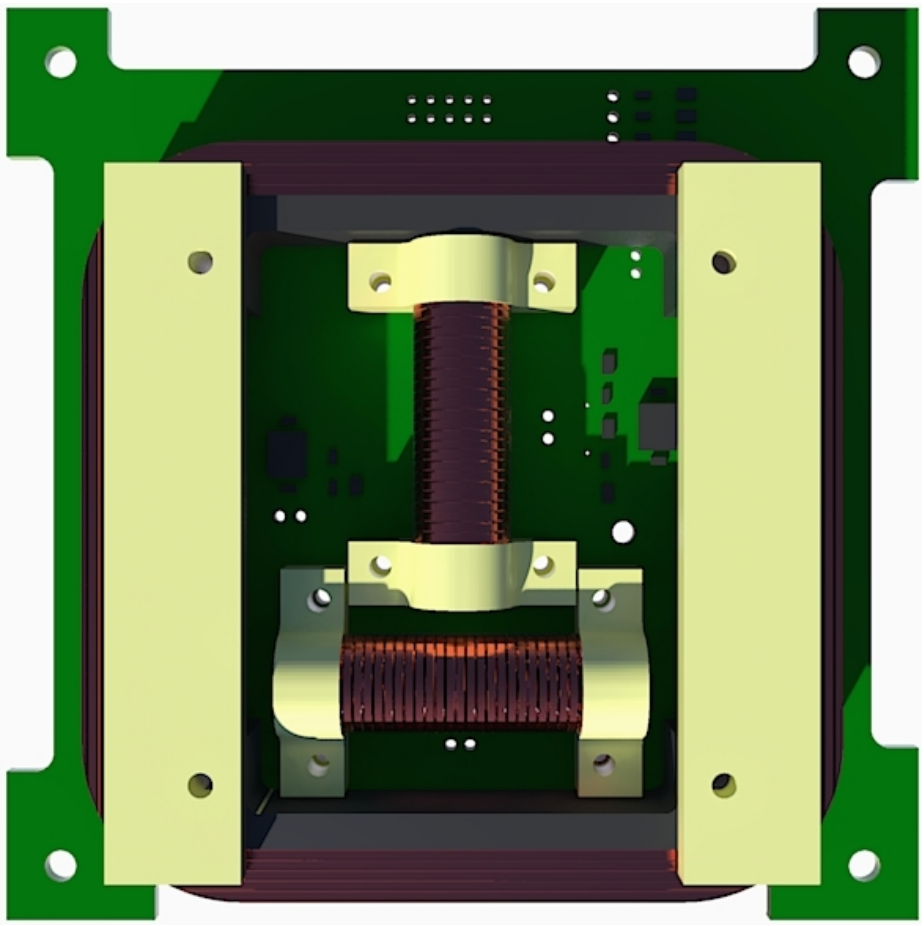

Figure 5.16: Rendering of a PCB mounted air core magnetorquer (outer winding) and two solid core magnetic torque rods flown on the GRIFEX mission. A similar system will be used on SCION. Image credit: Michigan eXploration Laboratory (MXL).

was calculated from the maximum difference in mass moment of inertias along the spacecraft principle axes. The disturbance torques are summarized in Table 5.5. The magnetic torque rods aligned with the spacecraft X and Y axes need a magnetic moment of 0.015 A m^2 to produce the required torque for maximum disturbance rejection in the weakest magnetic field, near the magnetic equator. Sizing the magnetic actuators at the weakest geomagnetic field for the greatest magnetic disturbance torque at the strongest geomagnetic field provides an inherent safety factor of 1.5 due to the relative strengths of Earth's magnetic field at these points in the orbit. Furthermore, to spin the spacecraft at high-latitude magnetic inclinations, an additional 0.02 A m^2 is required to spin up the spacecraft in the 100 s it takes to travel northward between 35° and 40° latitude. The variation in magnetic inclination over this period is between 64.5° and 68°. The in-house PCB embedded magnetorquer board has a calculated magnetic dipole moment of ∼0.055 A m^2 in all three axes, which provides a net safety factor of 3.0 over the worst case disturbance torque to ensure magnetic alignment. Commercially available CubeSat magnetic torque rods with a magnetically soft core (ferrite, Metglas®, nickel alloy, etc.) can also reasonably produce a magnetic moment of 0.1 A m^2, providing a net safety factor of 4.5.

Table 5.5: Summary of worst-case disturbance torques at 500 km and 60°. The worst-case residual magnetic torque is assumed from *Springmann et al.* [2010].

Disturbance	Torque [N m]
Aerodynamic	1.38E-07
Solar Pressure	1.56E-08
Residual Magnetic	*4.53E-07*
Gravity Gradient	1.18E-09
Safety Factor (SF)	3.0
Maximum Disturbance	1.36E-06

5.3.5 SCION Mission Conclusion

SCION represents a concept for a rapidly developed, low-cost, and focused scientific mission to answer important questions about the nature of mid-latitude scintillation and the small-scale density structure in the ionosphere. An important result of this study is the overall feasibly of such a mission from the CubeSat platform. Much of the future work for SCION centers on developing the necessary control algorithms for the spacecraft spin rate, further modeling of aerodynamic drag forces and spacecraft separation, and improved methods to downlink the large data volume produced. Fortunately, the remaining technical challenges have credible solution paths that will help to fully realize this mission with continued work.

CHAPTER VI

Conclusions

6.1 Summary of Findings

This thesis has been an investigation into the small-scale variability of the mid-latitude ionosphere during the occurrence of SED density plumes over North America. The data used in these analyses came primarily from a single station GPS receiver, ANNA, located in Ann Arbor, Michigan. A comparison with other North American stations for the case study in Chapter III suggested that the ANNA observations for the spatial scales of interest to this thesis were comparable with those from stations within 1000 km, and therefore its observations are a good representation of the ionosphere's behavior over North America in the mid-latitudes.
In Chapter II, this thesis demonstrated a new methodology that connected kilometer scale density structure and variability with larger 100 km scale and their evolution through time. The combination of TEC maps to identify large scale background structure, single-station TEC data, and Fast Fourier Transforms of the filtered Slant Total Electron Content, and SuperDARN radar velocity measurements showed the ability to detect, locate, and estimate the size of small-scale variability in SED plume systems.
In Chapter III the methodology of Chapter II was demonstrated on the 17-Mar-2015 "St. Patrick's Day Storm" — the strongest storm of this solar cycle. It

indicated the presence of small-scale irregularities between 3-10 km in size particularly on the poleward edge of the SED plume that were comparable to those observed in the aurora. It also showed longitudinal differences in subsequent crossings by IPPs of the plume's poleward edge suggesting large-scale density changes that may be occurring as the plume propagates toward the noontime cusp. Chapter IV applied the same methodology to a group of twelve geomagnetic storms, which are listed in Table 4.3, and identified several common characteristics (including FFT spectrum metrics and cycle slip statistics) for the regions of the SED plume system. It also analyzed storms that were outliers of those common characteristics and investigated possible differences including Universal Time and Local Time of Sudden Storm Commencement and minimum Disturbance Storm Time, storm strength, and SuperDARN velocity observations, including the components parallel and perpendicular to the SED plume system. Lastly it identified a special case region of the SED plume system referred to as the "plume pocket" that seems to contribute to the unique observations of the storm on 20-Dec-2015.

Finally, Chapter V presented the CubeSat mission concept SCintillation and Ionospheric Occultation NanoSat (SCION) that will improve observations of small-scale irregularities by resolving the altitude ambiguities in ground based observations of small-scale irregularities, use closely-space ($\sim$km) multipoint measurements to directly characterize irregularity length scales, and improve coverage over the oceans and in particular at magnetic conjugate points in the southern hemisphere. Through a high-level mission design, it has been demonstrated that the SCION mission is feasible and unique challenges, such as the spacecraft separation control, can be mitigated without the need of a propulsion system.

6.2 Future Work

Follow-on work to this thesis should seek to improve the statistics of the preliminary study in Chapter IV. This can be done in several ways to answer different questions about the general characteristics of the small-scale density structure in SED plume systems. For example, multi-station observations would expand the geographic range of observation of the SED plume system and, in particular, determine if the equivalent plume regions observed at different latitudes produce the same results or if these observations are unique to the plumes observed at the latitude of ANNA, e.g., do plume pockets that are formed outside the ANNA observation area also exhibit patterns of increased cycle slips or does it depend on the latitude where they occur?

Presently the limiting factor in the analysis methodology described in Chapter II of this thesis is the identification and classification of which region the IPPs are observing. Future work should include the development of algorithms to automatically classify the plume systems and assign them to observations at the IPPs. This would enable hundreds of storms to be analyzed, including multi-station studies and storms of all strengths. Such a body of analyzed data has the potential to reveal the systematic behavior in much the same way as TEC maps from networks of GPS receivers have changed our understanding of mid-latitude storm-time dynamics.

In addition to the body of 1 Hz data used in this study, there is also a large 20 Hz data set to be analyzed. The 20 Hz data will allow even smaller density structure to be detected. Further, a scintillation monitor recently installed at the Space Research Building (SRB) by members of the Space Physics Research Laboratory would allow for joint observations of GPS TEC and direct measurements of scintillation effects on the GPS signal.

BIBLIOGRAPHY

BIBLIOGRAPHY

Afraimovich, E. L., E. I. Astafieva, V. V. Demyanov, and I. F. Gamayunov (2005), Mapping of spatial distribution of ionosphere small-scale structure, phase slips and positioning accuracy as deduced from two-frequency measurements of GPS signals, *Proc. of General Assembly of The Union of Radio Science (URSI GA), Oct. 5–7, 2005, Delhi, India*.

Anderson, D. N. (1976), Modeling the midlatitude F-region ionospheric storm using east-west drift and a meridional wind, *Planetary and Space Science*, *24*(1), 69–77, doi:10.1016/0032-0633(76)90063-5.

Anthes, R. A., et al. (2008), The COSMIC/FORMOSAT-3 Mission: Early Results, *Bulletin of the American Meteorological Society*, *89*(3), 313–333, doi:10.1175/BAMS-89-3-313.

Arlas, J., and S. Spangelo (2013), GPS Results for the Radio Aurora Explorer II CubeSat Mission, in *Proceedings of AIAA Region III Student Conference*, American Institute of Aeronautics and Astronautics, Ann Arbor, MI, doi:10.2514/6.2013-123.

Basu, S., and K. M. Groves (2001), Specification and Forecasting of Outages on Satellite Communication and Navigation Systems, in *Space Weather*, edited by P. Song, H. J. Singer, and G. L. Siscoe, pp. 423–430, American Geophysical Union.

Basu, S., et al. (2008), Large magnetic storm-induced nighttime ionospheric flows at midlatitudes and their impacts on GPS-based navigation systems, *Journal of Geophysical Research: Space Physics*, *113*(A3), A00A06, doi:10.1029/2008JA013076.

Belova, N. A., and D. Acosta-Avalos (2015), The Effect of Extremely Low Frequency Alternating Magnetic Field on the Behavior of Animals in the Presence of the Geomagnetic Field, *Journal of Biophysics*, *2015*, e423,838, doi:10.1155/2015/423838.

Brahmanandam, P. S., G. Uma, J. Y. Liu, Y. H. Chu, N. S. M. P. Latha Devi, and Y. Kakinami (2012), Global S4 index variations observed using FORMOSAT-3/COSMIC GPS RO technique during a solar minimum year, *Journal of Geophysical Research: Space Physics*, *117*(A9), A09,322, doi:10.1029/2012JA017966.

Carrano, C. S., K. M. Groves, C. L. Rino, and P. H. Doherty (2016), A technique for inferring zonal irregularity drift from single-station GNSS measurements of intensity (S4) and phase ($_{\backslash \mathrm{phi}}$) scintillations, *Radio Science*, p. 2015RS005864, doi:10.1002/2015RS005864.

Chen, F. F. (1984), *Introduction to plasma physics and controlled fusion*, 2nd ed ed., Plenum Press, New York.

Cherniak, I., and I. Zakharenkova (2015), Dependence of the high-latitude plasma irregularities on the auroral activity indices: a case study of 17 March 2015 geomagnetic storm, *Earth, Planets and Space*, *67*(1), 151, doi:10.1186/s40623-015-0316-x.

Coster, A. J. (2007), Mitigation of Ionospheric Propagation Errors with GPS, in *2007 IEEE Radar Conference*, pp. 922–926, doi:10.1109/RADAR.2007.374342.

Coster, A. J., M. J. Colerico, J. C. Foster, W. Rideout, and F. Rich (2007), Longitude sector comparisons of storm enhanced density, *Geophysical Research Letters*, *34*, 18,105, doi:10.1029/2007GL030682.

Crowley, G., et al. (2011), Dynamic Ionosphere Cubesat Experiment (DICE), in *Proceedings of the 25th Annual AIAA/USU Conference on Small Satellites*.

Dalgarno, A., and F. J. Smith (1962), The thermal conductivity and viscosity of atomic oxygen, *Planetary and Space Science*, *9*(1–2), 1–2, doi:10.1016/0032-0633(62)90064-8.

Damasceno Ferreira, L. D., and J. Jaime Da Cruz (1991), Attitude and spin rate control of a spinning satellite using geomagnetic field, *Journal of Guidance, Control, and Dynamics*, *14*(1), 216–218, doi:10.2514/3.20628.

Datta-Barua, S., P. H. Doherty, S. H. Delay, T. Dehel, and J. A. Klobuchar (2003), Ionospheric scintillation effects on single and dual frequency GPS positioning, in *Proceedings of ION GPS/GNSS*, pp. 336–346.

Datta-Barua, S., T. Walter, G. S. Bust, and W. Wanner (2014), Effects of solar cycle 24 activity on WAAS navigation, *Space Weather*, *12*(1), 46–63, doi:10.1002/2013SW000982.

Deng, Y., and A. J. Ridley (2006), Role of vertical ion convection in the high-latitude ionospheric plasma distribution, *Journal of Geophysical Research: Space Physics*, *111*(A9), A09,314, doi:10.1029/2006JA011637.

Doherty, P., A. J. Coster, and W. Murtagh (2004), Space weather effects of October–November 2003, *GPS Solutions*, *8*(4), 267–271, doi:10.1007/s10291-004-0109-3.

Dungey, J. W. (1961), Interplanetary Magnetic Field and the Auroral Zones, *Physical Review Letters*, *6*(2), 47–48, doi:10.1103/PhysRevLett.6.47.

Dyrud, L., and J. T. Fentzke (2011), GEOScan Planning Workshop Report, in *Proceedings from the GEOScan Planning Workshop*, Annapolis, MD.

Fong, C.-J., N. Yen, S.-K. Yang, S.-S. Chen, and S. Chi (2007), GPS radio occultation and mission results from FORMOSAT-3/COSMIC spacecraft constellation, in *Recent Advances in Space Technologies, 2007. RAST'07. 3rd International Conference on*, pp. 748–753, IEEE.

Foster, J. C. (1993), Storm time plasma transport at middle and high latitudes, *Journal of Geophysical Research: Space Physics*, *98*(A2), 1675–1689, doi:10.1029/92JA02032.

Foster, J. C., and W. J. Burke (2002), SAPS: A new categorization for sub-auroral electric fields, *Eos, Transactions American Geophysical Union*, *83*(36), 393–394, doi:10.1029/2002EO000289.

Foster, J. C., and W. Rideout (2005), Midlatitude TEC enhancements during the October 2003 superstorm, *\grl*, *32*, 12, doi:10.1029/2004GL021719.

Foster, J. C., P. J. Erickson, A. J. Coster, J. Goldstein, and F. J. Rich (2002), Ionospheric signatures of plasmaspheric tails, *Geophysical Research Letters*, *29*, 1623, doi:10.1029/2002GL015067.

Goldstein, J., B. R. Sandel, M. R. Hairston, and P. H. Reiff (2003), Control of plasmaspheric dynamics by both convection and sub-auroral polarization stream, *Geophysical Research Letters*, *30*(24), 2243, doi:10.1029/2003GL018390.

Hajj, G. A., and L. J. Romans (1998), Ionospheric electron density profiles obtained with the Global Positioning System: Results from the GPS/MET experiment, *Radio Science*, *33*(1), 175–190, doi:10.1029/97RS03183.

Headrick, J. M., and M. I. Skolnik (1974), Over-the-Horizon radar in the HF band, *Proceedings of the IEEE*, *62*(6), 664–673, doi:10.1109/PROC.1974.9506.

Heine, T. R., M. B. Moldwin, and S. Zou (2016), Small-Scale Structure of the Mid-Latitude SED Plume During the March 17, 2015 St. Patrick's Day Storm, *Journal of Geophysical Research (Space Physics)*.

Heine, T. R. P., M. B. Moldwin, S. Zou, J. Arlas, A. Desai, B. Heidt, S. McCarty, A. Nastasoiu, and V. Singh (2015), A CubeSat Concept for Multipoint Ionospheric GPS Occultation, *Journal of Small Satellites*, *4*(2), 329–356.

Hinch, E. J. (1988), Hydrodynamics at low Reynolds numbers: a brief and elementary introduction, in *Disorder and mixing*, pp. 43–56, Springer.

Horvath, I., and S. Crozier (2007), Software developed for obtaining GPS-derived total electron content values: GPS TEC, *Radio Science*, *42*(2), n/a–n/a, doi:10.1029/2006RS003452.

Huang, C.-S., J. C. Foster, L. P. Goncharenko, P. J. Erickson, W. Rideout, and A. J. Coster (2005), A strong positive phase of ionospheric storms observed by the Millstone Hill incoherent scatter radar and global GPS network, *Journal of Geophysical Research (Space Physics)*, *110*, A06,303, doi:10.1029/2004JA010865.

Institute, C. P. (2014), CubeSat Design Specification Rev. 13.

Kelley, M. C. (2009), *The earth's ionosphere: plasma physics and electrodynamics*, no. v. 96 in International geophysics series, 2nd ed ed., Academic Press, Amsterdam ; Boston.

Kelley, M. C., M. N. Vlasov, J. C. Foster, and A. J. Coster (2004), A quantitative explanation for the phenomenon known as storm-enhanced density, *Geophysical Research Letters*, *31*(19), L19,809, doi:10.1029/2004GL020875.

Ledvina, B. M., J. J. Makela, and P. M. Kintner (2002), First observations of intense GPS L1 amplitude scintillations at midlatitude, *\grl*, *29*, 1659, doi:10.1029/2002GL014770.

Liu, J., W. Wang, A. Burns, X. Yue, S. Zhang, Y. Zhang, and C. Huang (2016), Profiles of ionospheric storm-enhanced density during the 17 March 2015 great storm: SED DURING A GREAT STORM, *Journal of Geophysical Research: Space Physics*, *121*(1), 727–744, doi:10.1002/2015JA021832.

Love, J. J., and J. Rigler (2015), 17 March 2015.

Mannucci, A. J., B. D. Wilson, and C. D. Edwards (1993), A new method for monitoring the Earth's ionospheric total electron content using the GPS global network, *Tech. rep.*, Jet Propulsion Laboratory.

NASA-STD-8719.14A (2012), Process for Limiting Orbital Debris.

NOAA/NGDC - Earth Observation Group - Defense Meteorological Satellite Progam (), NOAA/NGDC - Earth Observation Group - Defense Meteorological Satellite Progam.

NPR 8715.6A (2009), NASA Procedural Requirements for Limiting Orbital Debris, *Tech. rep.*, National Aeronautics and Space Administration.

Parker, E. N. (1958), Dynamics of the Interplanetary Gas and Magnetic Fields, *Astrophys. J.*, *128*, 664–676, doi:10.1086/146579.

Pi, X., A. J. Mannucci, U. J. Lindqwister, and C. M. Ho (1997), Monitoring of global ionospheric irregularities using the Worldwide GPS Network, *Geophysical Research Letters*, *24*(18), 2283–2286, doi:10.1029/97GL02273.

Prikryl, P., P. T. Jayachandran, S. C. Mushini, D. Pokhotelov, J. W. MacDougall, E. Donovan, E. Spanswick, and J.-P. St.-Maurice (2010), GPS TEC, scintillation and cycle slips observed at high latitudes during solar minimum, *Annales Geophysicae*, *28*(6), 1307–1316, doi:10.5194/angeo-28-1307-2010.

Sabol, C., R. Burns, and C. A. McLaughlin (2001), Satellite Formation Flying Design and Evolution, *Journal of Spacecraft and Rockets*, *38*(2), 270–278, doi:10.2514/2.3681.

Schunk, R., and A. Nagy (2009), *Ionospheres: Physics, Plasma Physics, and Chemistry*, Cambridge University Press, Cambridge.

Seo, J., T. Walter, and P. Enge (2011), Correlation of GPS signal fades due to ionospheric scintillation for aviation applications, *Advances in Space Research*, *47*(10), 1777–1788, doi:10.1016/j.asr.2010.07.014.

Simon, A. (1963), Instability of a Partially Ionized Plasma in Crossed Electric and Magnetic Fields, *Physics of Fluids (1958-1988)*, *6*(3), 382–388, doi:10.1063/1.1706743.

Sorensen, J. A. (1971), A Magnetic Attitude Control System for an Axisymmetric Spinning Spacecraft, *Journal of Spacecraft and Rockets*, *8*(5), 441–448, doi:10.2514/3.59677.

Springmann, J. C., J. W. Cutler, and H. Bahcivan (2010), Magnetic sensor calibration and residual dipole characterization for application to nanosatellites, *Toronto, Ontario Canada*.

Sugiura, M., T. Kamei, A. Berthelier, and M. Menvielle (1991), *Equatorial Dst Index: 1957-1986*, ISGI Publications Office.

Sun, Y.-Y., T. Matsuo, E. A. Araujo-Pradere, and J.-Y. Liu (2013), Ground-based GPS observation of SED-associated irregularities over CONUS: SED-ASSOCIATED IRREGULARITIES OVER CONUS, *Journal of Geophysical Research: Space Physics*, *118*(5), 2478–2489, doi:10.1029/2012JA018103.

Tsybulya, K. (2005), Medium- and small-scale ionospheric irregularities detected by GPS radio occultation method, *Geophysical Research Letters*, *32*(9), doi:10.1029/2005GL022420.

Vallado, D. A., and D. Finkleman (2008), A critical assessment of satellite drag and atmospheric density modeling, in *AIAA/AAS astrodynamics specialist conference and exhibit*, pp. 18–21.

Wloszek, P., R. Glumb, R. Lancaster, C. Lietzke, S. McCarty, J. Arlas, B. Heidt, M. Ramirez, and V. Singh (2013), FTS CubeSat Constellation Providing 3d Winds.pdf, in *Proceedings of the 27th Annual AIAA/USU Conference on Small Satellites*, Logan, UT.

Yeh, K. C., and C.-H. Liu (1982), Radio wave scintillations in the ionosphere, *Proceedings of the IEEE*, *70*(4), 324–360.

Yizengaw, E., M. B. Moldwin, P. L. Dyson, and T. J. Immel (2005), Southern Hemisphere ionosphere and plasmasphere response to the interplanetary shock event of 29–31 October 2003, *Journal of Geophysical Research: Space Physics*, *110*(A9), 1–16, doi:10.1029/2004JA010920.

Yizengaw, E., M. B. Moldwin, P. L. Dyson, B. J. Fraser, and S. Morley (2006), First tomographic image of ionospheric outflows, *Geophysical Research Letters*, *33*(20), L20,102, doi:10.1029/2006GL027698.

Yizengaw, E., J. Dewar, J. MacNeil, M. B. Moldwin, D. Galvan, J. Sanny, D. Berube, and B. Sandel (2008), The occurrence of ionospheric signatures of plasmaspheric plumes over different longitudinal sectors, *Journal of Geophysical Research*, *113*(A8), 1–9, doi:10.1029/2007JA012925.

Yizengaw, E., E. Zesta, M. B. Moldwin, B. Damtie, A. Mebrahtu, C. E. Valladares, and R. F. Pfaff (2012), Longitudinal differences of ionospheric vertical density distribution and equatorial electrodynamics, *Journal of Geophysical Research (Space Physics)*, *117*, 1–10, doi:10.1029/2011JA017454.

Zhang, X.-Y., and M. B. Moldwin (2014), The source, statistical properties, and geoeffectiveness of long-duration southward interplanetary magnetic field intervals, *Journal of Geophysical Research: Space Physics*, *119*(2), 658–669, doi:10.1002/2013JA018937.

Zou, S., A. J. Ridley, M. B. Moldwin, M. J. Nicolls, A. J. Coster, E. G. Thomas, and J. M. Ruohoniemi (2013), Multi-instrument observations of SED during 24-25 October 2011 storm: Implications for SED formation processes, *Journal of Geophysical Research (Space Physics)*, *118*, 7798–7809, doi:10.1002/2013JA018860.

Zou, S., M. B. Moldwin, A. J. Ridley, M. J. Nicolls, A. J. Coster, E. G. Thomas, and J. M. Ruohoniemi (2014), On the Generation/Decay of the Storm-Enhanced Density (SED) Plumes: Role of the Convection Flow and Field-Aligned Ion Flow, *Journal of Geophysical Research: Space Physics*, p. 2014JA020408, doi:10.1002/2014JA020408.